The Thesis committee for Adrien Wilbert

Certifies that this is the approved version of the following thesis:

On the Crushing of Honeycomb Under Axial Compression

APPROVED BY

SUPERVISING COMMITTEE:

Supervisor: __________________________

Stelios Kyriakides

____

Krishnaswamy Ravi-Chandar

On the Crushing of Honeycomb Under Axial Compression

by

Adrien Wilbert, Diplôme d'Ingénieur

Thesis

Presented to the Faculty of the Graduate School of
The University of Texas at Austin
in Partial Fulfillment
of the Requirements
for the Degree of

Master of Science in Engineering

The University of Texas at Austin
December, 2010

Dedication

To my parents, Isabelle and Sylvain, and my brother Guillaume

Acknowledgements

I would like to express my profound gratitude to all the people who, along the past two years, have assisted me towards this research. I am particularly grateful to my supervisor Stelios Kyriakides who made this work possible by mentoring my studies at The University of Texas at Austin. His wise advices and his scientific expertise have been essential at every stage along the way. I would also like to thank Dr. Ravi-Chandar for serving as a second reader of this thesis. I would like to express my particular consideration to Mrs. Sylviane Wignacourt at Ecole Centrale de Lille in France who made this double-degree experience possible by supporting me and helping me through the application process for attendance at UT Austin. Special thanks go to Dr. Wen-Yea Jang for starting the numerical work and helping me using ABAQUS. I would also like to thank my fellow graduate students and friends for their support and friendship, especially Julian Hallai, Aaron Albrecht, Federico Gallo, Vishal Nayyar and Shravan Growishankar. The financial support of the National Science Foundation under Grant No. CMMI-0856155 and the University of Texas is acknowledged with thanks. Finally, I would also like to thank the Hexcel Corporation for providing the honeycomb tested.

December 2010

On the Crushing of Honeycomb Under Axial Compression

by

Adrien Wilbert, MSE

The University of Texas at Austin, 2010

SUPERVISOR: Stelios Kyriakides

This thesis presents a comprehensive study of the compressive response of hexagonal honeycomb panels from the initial elastic regime to a fully crushed state. Expanded aluminum alloy honeycomb panels with a cell size of 0.375 in (9.53 mm), a relative density of 0.026, and a height of 0.625 in (15.9 mm) are laterally compressed quasi statically between rigid platens under displacement control. The cells buckle elastically and collapse at a higher stress due to inelastic action. Deformation then first localizes at mid-height and the cells crush by progressive formation of folds; associated with each fold family is a stress undulation. The response densifies when the whole panel height is consumed by folds. The buckling, collapse, and crushing events are simulated numerically using finite element models involving periodic domains of a single or several characteristic cells. The models idealize the microstructure as hexagonal, with double walls in one direction. The nonlinear behavior is initiated by elastic buckling while inelastic collapse that leads to the localization observed in the experiments occurs at a significantly higher load. The collapse stress is found to be mildly sensitive to various problem imperfections. For the particular honeycomb studied, the collapse stress is 67% higher than the buckling stress. It was also shown that all aspects of the compressive behavior can be reproduced numerically using periodic domains with a fine mesh capable of capturing the complexity of the folds. The calculated buckling stress is reduced when considering periodic square domains as the compatibility of the buckles between neighboring cells tends to make the structure more compliant. The mode consisting of three half waves is observed in every simulation but its amplitude is seen to be accented at the center of the domains. The calculated crushing response is shown to better resemble measured ones when a 4×4 cell domain is used, which is smoother and reproduces decays in the amplitude of load peaks. However, the average crushing stress can be captured with engineering accuracy even from a single cell domain.

Table of Contents

List of Tables

List of Figures

Chapter 1

Introduction

Man-made cellular materials have been extensively developed, analyzed and used over the past fifty years in a variety of practical applications. Two-dimensional cellular materials come mainly in the form of honeycombs with various cell shapes. Three-dimensional ones are usually in the form of foams with either open or closed cells. Both families are made from a variety of materials such as metals, polymers, ceramics, carbon and paper (Gibson & Ashby, 1997). They can be manufactured to chosen cell sizes and relative densities, but as a family, cellular materials have relatively high strength-to-weight and stiffness-to-weight ratios. In addition, they have excellent energy absorption characteristics, good sound and heat insulation properties and are used as filters.

One of the structural uses of cellular materials is as cores in sandwich structures. In other words they provide the shear connection that separates two thin plates or shells. The result is usually a sandwich that is stiff in bending but can also absorb energy due to impact.

Honeycomb is particularly suited for sandwich construction as it is relatively strong and stiff along the normal to the microstructure but compliant and weak in plane (e.g., Allen [1969], Marshall [1982]). Hexagonal cells are most common but circular, square and other cell geometries including ones that are auxetic and others that can accommodate bending of a sheet exist (Hexcel, 2010) (see Fig. 1.1). Honeycomb is made from most materials, metals, polymers, paper, etc, to fit the application. Their wide use stems from their excellent specific stiffness and weight, their outstanding energy absorption characteristics and their cost effectiveness (Gibson & Ashby, 1997).

The aerospace industry has favored the use of sandwich construction in applications where stiffness-to-weight and strength-to-weight ratios are critical. For example, Fig. 1.2a shows the extensive use of honeycomb in different components of the Airbus A380-800. These include control surfaces, nacelles, floors as well as many non-structural parts such as interior partitions, overhead lockers, etc. Figure 1.2b shows several cutouts from control surfaces with honeycomb and polymeric foams cores. A related application is in helicopter blades shown in Fig. 1.3a.

Modern naval ships also make extensive use of sandwich construction consisting of glass/epoxy composite faceplates and either honeycomb or closed cell foam cores (see Fig. 1.3b). Driven by their favorable energy absorption characteristics and weight savings they provide, the automotive industry is increasing its use of cellular materials in applications such as bumpers. The energy absorption of tubular components is often increased by filling them with foams or honeycombs. Special designs allow the loads/crushing energy to be transferred to these crushable elements during crash situations, thus protecting the passenger cabin. Figure 1.4 shows how honeycomb has been introduced in the front of the cabin of the Pininfarina Nido concept car in order to absorb the shock energy in case of an accident. Three layers with honeycomb of different densities have been used conceivably to crush sequentially at different load levels.

The wide use of honeycomb in practice generated a need for establishing their mechanical properties and this spawned an extensive literature on the subject starting from the anisotropic elastic properties, the onset of “yielding” and collapse, and the crushing response (e.g., Gibson & Ashby, 1997). Of all honeycombs, metallic ones with hexagonal cells have received the most attention because of their outstanding properties and the simplicity of their manufacture. The extensive literature on the out of plane mechanical behavior was motivated first by the design needs of sandwich construction (e.g., Kelsey et al. [1958], Penzien & Didriksson [1964], Grediac [1993], Zhang & Ashby [1992], Gibson & Ashby [1997]). The second motivation comes from the use of such honeycombs for energy absorption in a variety of applications (McFarland [1963, 1964], Wierzbicki [1983], Wierzbicki & Abramowicz [1983], Goldsmith & Sackman [1992], Mohr & Doyoyo [2004a, 2004b], Aktay et al. [2008], Yamashita & Gotoh [2005], among others).

A similarly large literature on the in-plane properties is mainly motivated by the similarities between the behavior of 3-D cellular materials, namely foams, and that of honeycombs loaded and crushed in-plane; in other words, here the honeycomb represents a 2-D model for the more complex foams with space-filling 3-D microstructure (e.g., Gibson et al. [1982], Klintworth & Stronge [1988], Papka & Kyriakides [1994, 1998], Triantafyllidis & Schraad [1998]).

The present study is concerned with the more traditional problem of transverse compression. In particular, the aim is to establish all aspects of the compressive response of honeycomb sandwich panels; that is, the initial linearly elastic behavior, the onset of instability, the onset of collapse, its localization, and the progressive folding and crushing under persistent compression. Of these properties, the crushing behavior, or in other words the energy absorption capacity, has received the most attention experimentally (e.g., McFarland [1963,1964], Goldsmith & Sackman [1992], Mohr & Doyoyo [2004a]) and analytically; early on using kinematically admissible collapse mechanisms (e.g., Wierzbicki [1983], Wierzbicki & Abramowicz [1983]), and more recently with more representative numerical models (e.g., Mohr & Doyoyo [2004b]).

The study performed is based on a Hexcel aluminum alloy honeycomb bonded to aluminum faceplates. The core has a relative density, ρ^* / ρ, (ρ^* = density of honeycomb, ρ = density of Al) of 2.6%, which ranks it in the ultra lightweight category. The honeycomb is manufactured as described in Papka & Kyriakides [1998] (see also Hexcel, 2010): lines of epoxy of chosen width and spacing are “printed” on thin metal foils. The foils are stacked together in a manner that places the bond lines of adjacent foils half a period out of phase as shown in Fig. 1.5. The foil stacking is placed in a press with hot platens where the epoxy lines are cured. Axial strips of the required honeycomb thickness are then cut from the stacking and the strips are mechanically expanded to form the hexagonal cell honeycomb as shown in Fig. 1.5. The initial width and spacing of the bond lines determines the cell diameter (*c*). Honeycomb made in this fashion has double wall thickness in one direction (L); in other words, it is anisotropic with two principal directions, L and W. Papka & Kyriakides [1998] discuss other effects of the process such as changes to the mechanical properties of the foil material, introduction of residual stresses, small rounding of the expanded corners of the hexagonal cells, and geometric imperfections introduced by small deviations in the bond line spacing and under or over expansion.

The study starts in Chapter 2 with the presentation of results from compression and crushing experiments on finite size sandwich panels. Chapter 3 details the methodology used in the Finite Element Analyses adopted and compares the results from a representative unit cell with experiments. Chapter 4 reports parametric studies of all aspects of the response. Finally, Chapter 5 presents the main conclusions drawn from this study.

Chapter 2

Experiments

A series of crushing experiments was performed on Hexcel Al-5052-H39 honeycomb in order to evaluate and analyze the structural properties of interest described earlier. Particular attention was paid to the geometrical measurements of both the hexagonal cells and the laboratory prepared sandwich panels. The inelastic properties of the base materials used in the sandwich panels – Aluminum and Hysol epoxy - were also measured. This chapter presents the experimental setups and procedures used as well as the experimental results.

2.1 GEOMETRICAL MEASUREMENTS

The honeycomb used came from Hexcel as 0.625 x 24 x 24 in (15.9 x 600 x 600 mm) sheets. Specimens were extracted by careful cutting of the walls along the L and W directions using special scissors (see Fig. 2.1). Following are summaries of measurements taken to characterize the geometry of the microstructure as well as that of the panels.

2.1.1 Hexagonal Cell Geometry

The cell geometry of Hexel honeycombs used in this study was measured precisely using an optical set up consisting of a high-resolution video camera coupled with different lenses. Calibrated gages - rods and blocks – were used as references to establish the required dimensions. Images taken were analyzed in Photoshop® and dimensions were assigned by comparison to the gages. Particular attention was given to the alignment of the axes of the honeycomb, the camera and the gage, so that misalignments did not influence the quality of the measurements. The values reported below are averages from multiple measurements: 30 for the cell size, 40 for the wall thicknesses and 10 for the height. Values for the cell size, *c*, the wall thickness, *t*, and the height, *h*, defined in Fig. 1.5 are listed in Table 2.1. Figure 2.2 shows a close up view of a cell's corner obtained using the optical set up. One can see the two single walls on the upper part bonded into a double wall on the lower part of the photograph.

Table 2.1 Geometric parameters measured from Al-5052-H39 honeycomb cells

c in (mm)	ℓ in (mm)	t in (mm)	λ	h in (mm)	$\frac{\rho^*}{\rho}$
0.375 (9.53)	0.2165 (5.50)	0.00374 (95)	0.92	0.625 (15.9)	0.026

Measurements of the cell wall lengths showed consistent deviation from perfect hexagon ($\ell \equiv$ length of sides of perfect hexagon with $c = 0.375$ in). This arises from a somewhat deficient bond width defined as $\lambda\ell$ in Fig. 2.3. The value of λ quoted in Table 2.1 is the average from measurements on 30 cells.

Assuming perfect hexagonal geometry, the relative density of honeycomb with double walls in one direction is given by (Papka and Kyriakides, 1994):

$$\frac{\rho^*}{\rho} = \frac{8}{3}\left(\frac{t}{c}\right). \tag{2.1}$$

Thus, for the present honeycomb $\rho^*/\rho = 0.026$.

2.1.2 Sandwich Panel Geometry

The size of the majority of the honeycomb specimens tested was 8 x 15 cells while one larger specimen with 15 x 15 cells was also analyzed. Table 2.2 lists the main dimensions: length L_L and width L_W of 10 specimens (see Fig. 2.4). Because of the smalls irregularities in the size of the side edges that come from the cutting, these dimensions were obtained by averaging series of 5 measures (2 taken on the sides, 1 in the center and 2 in between).

2.2 PREPARATION OF SANDWICH SPECIMEN

Various sizes of honeycomb specimens ranging from 8 x 15 to 15 x 15 cells (W x L) were prepared and analyzed (see Fig. 2.1). Two thin rectangular aluminum plates 0.030 in (0.76 mm) thick were cut to dimensions slightly larger than the honeycomb domain and bonded to the top and bottom parts of the core as shown in Fig. 2.4 by the following process.

The faces of these aluminum plates that are in contact with the honeycomb core were roughened with fine sandpaper and cleaned with acetone. A high-strength film epoxy (Hysol EA-9696, 0.060 psf NW) was then applied entirely on the roughened sides of the face sheets. Each side of the panel was cured separately using the bottom platen of a press with controllable heating. The platen was heated to 250°F (121°C) and once steady state was achieved the specimen was placed on it applying small pressure with a weight. The curing time was 90 minutes. At this stage the specimen was flipped over and the process was repeated for the curing of the second side. This process limits the effect of gravity on the film epoxy, which becomes very viscous during initial heating. It also tends to limits the formation of air bubbles in the epoxy layer.

2.3 MATERIAL PROPERTIES

The elastic-plastic properties under uniaxial tension of the base materials used in these honeycomb sandwich panels were evaluated. The aluminum and epoxy materials were extracted from the bulk honeycomb and epoxy sheets respectively, and prepared into samples. More precise information about the geometry of the different specimen and the measured stress-strain responses are given in Appendix A.

2.3.1 Aluminum Alloy

A representative stress-strain response from a small specimen cut through the height of the Al-5052-H39 honeycomb (single wall) is shown in Fig. A.2. The elastic modulus (E) was found to be very close to 10^4 ksi (69 GPa) and the yield stress σ_o reached a value of 36 ksi (248 MPa) both listed in Table 2.3.

Table 2.3 Material properties obtained from Al-5052-H39 specimen

Type	E ksi (GPa)	σ_o ksi (MPa)
Al-5052-H39	10^4 (69)	36 (248)

2.3.2 Epoxy Resin

The Hysol EA-9696 epoxy resin, extracted from bulk 0.060 psf (0.293 kg/m^2), sheets was also tested in uniaxial tension and a representative stress strain response is shown in Fig. A.4. The elastic modulus was found to be about 211 ksi (1.45 GPa) and the yield stress was measured to be 3.78 ksi (26.1 MPa). A summary of these results is reported in Table 2.4 below.

Table 2.4 Material properties obtained from Hysol EA-9696 epoxy specimen

Type	E ksi (GPa)	σ_o ksi (MPa)
Hysol EA-9696	211 (1.45)	3.78 (26.1)

2.4 LATERAL COMPRESSION OF HONEYCOMB

2.4.1 Testing Device and Experimental Setup

The panels were compressed in a screw-type testing machine between parallel platens with a ground finish at a displacement rate of $\dot{\delta} = 5 \times 10^{-4} h$ s^{-1}.

The prescribed displacement and induced load were recorded in a computer based data acquisition system while simultaneously the deformations of the cell walls on two of the sides of the panel were monitored with a video camera. A picture of the experimental setup is shown in Fig. 2.5.

2.4.2 Results from a Typical Crushing Response from a Honeycomb Panel

Figure 2.6 shows the stress-shortening response ($\sigma - \delta$) recorded in a typical honeycomb crushing experiment (dashed line). The nominal stress σ is the force recorded divided by the projected area of the honeycomb ($L_L \times L_W$ in Fig. 2.4). The initial part of the response is stiff and nearly linear. Along the way, the sides of the hexagonal cells were observed to buckle developing a number of axial waves. The buckling was elastic as the waves would disappear if the panel was unloaded early enough. At higher stress levels inelastic action takes place, a limit load develops and simultaneously the axial waves tend to localize. The maximum stress achieved, or *collapse stress*, was 529 psi (3.65 MPa) which represents the compressive strength, σ_{CO}, of the panel and the onset of crushing. As compression continues the load is seen to drop precipitously down to a local minimum that is associated with the formation of the first local fold. Subsequently, a number of stress undulations develop, which represent the formation of additional folds of the cell walls. The amplitude of the undulations is seen to decrease with δ. The particular test was terminated when the panel was crushed down to 40% of its original height and unloaded. At this stage it is useful to define a second characteristic stress for the problem, the *crushing stress*, $\overline{\sigma}_{ch}$. It is calculated by averaging the value of stress for a shortening comprised between the inflection point occurring after the first load trough and a shortening of 60% as shown in Fig. 2.7. For the case shown in Fig. 2.6a $\overline{\sigma}_{ch}$ is at a level of 254 psi (1.75 MPa).

A separate experiment was conducted by Floccari [2008] in order to document the details of the crushing behavior of cell walls. A larger panel 6.5 x 6.2 in (165 x 157 mm) was used for this purpose. The $\sigma-\delta$ response recorded is drawn in Fig. 2.6a with a solid line. The crushing was performed in a step-by-step fashion so that the specimen was unloaded after a certain amount of deformation. A small section of it was then removed from the panel by cutting along the L and W directions with a diamond saw, keeping the remainder for further crushing. The two faces of the removed sections were polished and photographed using a low magnification microscope. Thus for example, the first unloading was performed when the stress dropped to about 300 psi (2.07 MPa) following the onset of collapse (point ① on the response in Fig. 2.6a). The corresponding pair of photographs taken of the orthogonal faces is depicted as ① in Fig. 2.6b. From left to right the images correspond to the W and L planes of the honeycomb. The deformation is seen to have localized into a single wave symmetrically deployed about the mid-height. On the left, the single walls are bending alternately in and out of the page while on the right the double walls are bending inwards. It is interesting to observe that in the W plane image the double walls have debonded over a length of 0.1 *h* at mid-span (noted also in Wierzbicki [1983] and others).

The specimen was then reloaded, crushed to point ② just after the first load trough, unloaded again, and a second small section was removed in a similar fashion. The two internal planes were photographed and the corresponding images are depicted as ② in Fig. 2.6b. The mid-span deformation has now evolved into folds with some contact developing between the fold walls (see L image), which is responsible for the upswing in the overall load. The debonding observed in the W image in ① has been arrested and is seen to be limited to the crease of the fold.

In the next loading step, the stress continues to increase until point ③ when the stiffness of the honeycomb develops a point of inflection. This event is short-lived and the stress quickly begins to rise again, reaching point ④ at $\delta / h \approx 0.22$. As pointed out above, in the neighborhood of ② initial contact occurred on the bottom side of the folds in L. As crushing progresses, that side of the fold comes into full contact so that at ③, there is no longer any gap underneath the fold. Subsequently, the other half of each cell collapses until by ④ contact is achieved on both sides. Between these points, the stiffness dropped slightly because crushing occurred where the microstructure was not in self-contact. With the fold in full contact the load increases once more.

With further crushing the load reaches a second peak that is associated with the initiation of a second fold at the top half of the cells, thus breaking the symmetry of the deformation. The load drops tracing another valley at the bottom of which the specimen is unloaded once more and a new small section is removed. The formation of the second fold is clearly seen in images ⑤.

As the panel is crushed further the load goes through a third peak and is unloaded at ⑥. The beginning of the formation of a third fold in the upper half can be seen in images ⑥. By point ⑦, the third fold is fully developed and a new one starts in the bottom half that hitherto stayed essentially intact. The formation of the new fold is again associated with a stress peak but as evidenced in Fig. 2.6a the amplitude of the stress undulations is decreasing as crushing progresses further.

It is worth noting that the progressive removal of a small section of the panel to facilitate observation of the evolution of crushing was undertaken in order to analyze crushing in the interior of the specimen. It was thought that free edges might crush somewhat differently. After each section was removed the area of the specimen was adjusted and this was accounted for in evaluating σ.

It is interesting to observe that the incremental response in Fig. 2.6a is in very good agreement with the one corresponding to monotonic crushing (drawn with a dashed line). This agreement was generally repeated for most of the panels tested despite some differences in the folding patterns that developed in each.

That is, in some specimens the folding developed in the upper half of the honeycomb height first and in others in the bottom. In some cases, part of the specimen crushed in the former manner, part in the latter, and the two zones were joined by a transition with inclined folds.

2.4.3 Summary of Results from Crushing Experiments on Honeycomb Panels

Seven sandwich panel specimens with 0.030 in (0.76 mm) thick face sheets were tested under axial compression in the experimental setup described earlier. Even though honeycomb cores were extracted from different Hexel sheets, the stress-shortening responses showed great repeatability. Figures 2.8a and 2.8b show the stress-shortening ($\sigma - \delta$) responses for these experiments along with the experimental response obtained from Floccari [2008]. For better visualization, specimen unloaded at a shortening of about 60% are reported on Fig. 2.8a, while those unloaded at about 75% shortening are plotted on Fig. 2.8b.

In Table 2.5 we report the mean values of the collapse stress and of the average crushing stress from these experiments. Also included are the average values of each critical stress variable. The average collapse stress calculated is 539 psi (3.72 MPa) with one standard deviation being 38.1 psi (263 kPa). Since among other factors the onset of collapse is influenced by small initial geometric imperfections specific to each test, the variation is considered to be rather small. The average crushing stress from these experiments is 241 psi (1.66 MPa) with a standard deviation of 8.3 psi (0.06 MPa). Again, the variation is considered small.

2.4.4 Compression Tests on Honeycombs Without Faceplates

Three honeycomb specimens with 8 x 15 cells were tested in the same experimental setup without faceplates. The stress-shortening responses from three such experiments along with the response of the case A-HC-3 with bonded face sheets (dashed line) are reported on Fig. 2.9. The three responses show the same level of repeatability as the results from the panels. (Note that one of the three specimens was unloaded close to the first stress valley.) It is interesting to observe that the initial part of the response - up to the second load peak – is almost identical. However, the current collapse stresses are markedly higher. Table 2.6 shows that the average σ_{CO} is 631 psi (4.35 MPa), which compares with an average of 539 psi (3.72 MPa) for the panels.

Differences between the panels and pure honeycomb crushing responses are seen to develop after the second load peak. The third peak occurs at a same amount of shortening, but at a lower stress level while following this point the two responses diverge. Both responses have the same number of load peaks, which is confirmed by the observation of 5 folds in both cases – one at mid-height, two on the top and two on the bottom. The main difference is in the onset of densification at the end of the stress plateau. This occurs at a shortening of about 60% for the panels while it is delayed to a shortening of approximately 80% in the case of the pure honeycombs. This contrast is easily explained by the fact that the epoxy layers inside the panel core reduce the space available for the aluminum folds and therefore cause earlier stiffening in the crushing response. These differences also results in the crushing stress of the pure honeycombs being slightly lower. Thus the average of the two values in Table 2.6 is 220 psi (1.51 MPa) which compares with 241 psi (1.66 MPa) for the panels.

Looking for a reason in the difference in the collapse stresses between the panels and the pure honeycomb, we examined carefully panels for initial imperfections. Figure 2.10 shows plots of the out-of-plane initial imperfections along two perpendicular center lines (W and L). A small curvature can be seen to have developed most probably due to the two-step curing process that we followed and perhaps due to inadequate pressure applied. The mean radii of curvature are $R = 603h$ and $701h$ along W and L, respectively. Such initial imperfections introduce initial stresses and deformations that may reduce the collapse stress.

Chapter 3

Analysis

The compressive response and crushing of honeycomb observed in the experiments reported in Chapter 2 will now be simulated numerically using a finite element model representative of the infinite periodic domain. This Chapter describes the model and evaluates its performance.

3.1 ASSUMPTIONS

The problem complexity is reduced by neglecting the mechanical property changes and residual stresses, left behind by the mechanical expansion process through which the honeycomb is manufactured and by the preparation of the sandwich panels. Furthermore, the small rounding of the corners of the actual cells is also neglected. Thus, we will consider the idealized geometry shown in Fig. 3.1 that consists of perfect hexagonal cells of diameter c $(= \sqrt{3}\ell)$ and foil thickness t. The double wall thickness of the sides in the L direction is retained but the bonding of the two walls is neglected making them instead monolithic of thickness $2t$.

3.2 CHARACTERISTIC CELL

Because of the periodicity of the idealized microstructure, many of the mechanical characteristics of interest can be simulated using a characteristic cell assigned appropriate periodicity conditions. The cell chosen is drawn with a dashed line in the L-W plane in Fig. 3.1 and in a 3-D rendering in Fig. 3.2. It has a cross sectional area of $\sqrt{3}\ell \times 3\ell / 2$. Table 3.1 reports the geometric parameter of the model.

Table 3.1 Geometry of the characteristic cell

c in (mm)	ℓ in (mm)	t in (mm)
0.375 (9.525)	0.2165 (5.499)	0.00374 (0.095)

3.3 MAIN ELASTIC PROPERTIES

The main elastic properties can be easily evaluated from simple considerations. Thus the elastic modulus E_3^* is given by

$$\frac{E_3^*}{E} = \frac{8t}{3c} = \frac{\rho^*}{\rho} , \tag{3.1}$$

where E is the modulus of the base material. The two Poisson's ratios are equal to that of the base material ν (Zhang & Ashby, 1992)

$$\nu_{31}^* = \nu_{32}^* = \nu_{.} \tag{3.2}$$

The shear moduli were first evaluated by Kelsey *et al.* [1958] using energy methods and shear flow analysis that neglect bending of the cell walls. They are given by

$$\frac{3}{2\sqrt{3}}\frac{t}{\ell} \le \frac{G_{13}^{*}}{G} \le \frac{5}{3\sqrt{3}}\frac{t}{\ell} \quad \text{or} \quad \frac{9}{16}\frac{\rho^{*}}{\rho} \le \frac{G_{13}^{*}}{G} \le \frac{5}{8}\frac{\rho^{*}}{\rho} \tag{3.3a}$$

and

$$\frac{G_{23}^{*}}{G} = \frac{1}{\sqrt{3}}\frac{t}{\ell} = \frac{3}{8}\frac{\rho^{*}}{\rho}\ . \tag{3.3b}$$

The performance of these expressions was evaluated in Wilbert *et al.* [2010] using FE models and the honeycomb parameters listed in Table 3.1 (perfect hexagonal cell). In the models, the honeycomb upper and lower surfaces were restrained to remain plane and all cell sides do not develop out of plane deformations. The two expressions were found to yield shear moduli that were in very good agreement with those from the numerical results. In the case of G_{13}^{*} the upper bound was found to be closer to the numerical result than the lower bound (see also Grediac, 1993).

3.4 FINITE ELEMENT MODEL

In this Chapter we consider just one fully periodic unit cell; limiting effects of this choice of domain will be discussed later in Chapter 4.

3.4.1 Mesh

The unit cell is discretized within the nonlinear FE code ABAQUS using S4 shell elements, with three Gaussian integration points through the thickness. S4 is a fully integrated 4-node element that allows for finite membrane strains. Progressive folding that characterizes the crushing calculations is numerically intensive so the shell element selection and the discretization adopted were guided by computational efficiency. A regular mesh with nearly square elements was adopted, while the number of elements used was selected from convergence studies that follow.

3.4.2 Boundary Conditions

For the panels tested a thin film of epoxy is used to bond the faceplates to the honeycomb. When cured the epoxy tends to form meniscus-like fillets at the corners of the cell walls and the plate. After looking into the effect of the fillets on the calculated response it was decided that including them would make the calculation numerically cumbersome without adding significantly to the accuracy of the predictions. Thus, the top and bottom edges of the unit cell are assumed to be fixed, except that the top can translate in the x_3-direction. This mimics the axial crushing of honeycomb under displacement control.

3.4.3 Periodicity Conditions

The following periodicity conditions are used for the four lateral edges of the unit cell. Define the edges as (A_1, A_2) and (B_1, B_2) as shown in Fig. 3.2. The displacements and rotations of points on these edges are respectively denoted by (u_{i1}, u_{i2}) and $(\theta_{i1}, \theta_{i2})$ $i = 1, 3$. The following relationships are prescribed for the degrees of freedom of points on each pair of faces:

$$u_{i1} - u_{i2} = u_{i1}^{ref} - u_{i2}^{ref} \text{ and } \theta_{i1} - \theta_{i2} = 0, \; i = 1,3, \qquad (3.4)$$

where u_{ij}^{ref} are displacements of conjugate points on opposite sides chosen as reference points. Equations (3.4) hold for every node on the four lateral edges, with the exception of the 8 nodes that are also contained in the top and bottom edges, which are required to satisfy the prescribed boundary conditions.

Applying these periodicity conditions within ABAQUS is rather cumbersome as specific nodes on conjugate sides must be related. This was automated by developing a Matlab code to pre-process the numbering of nodes in the model and thus the edges as described in Section 3.4.5.

3.4.4 Material Properties

The aluminum alloy material is modeled as a finitely deforming J_2 solid that hardens isotropically. The model is calibrated to a trilinear fit of the measured tensile stress-strain response of the honeycomb foil show in Fig. 3.3. It has an elastic modulus of 10^4 ksi (69 GPa), a yield stress of 36 ksi (248 MPa), a postyield modulus of 57 ksi (393 MPa) up to a strain of 10% and is perfectly plastic at higher values (see also Table 3.2; true stress-logarithmic plastic strain version). The ABAQUS/Explicit code also requires the density of the base material. The value of 0.0975 lb/in^3 (2700 kg/m^3) was assigned for this purpose.

Table 3.2 Material properties of the honeycomb used in all FE models

Aluminum alloy	E ksi (GPa)	E' ksi (MPa)	σ_0 ksi (MPa)	ρ lb/in^3 (kg/m^3)
Al-5052	10^4 (68.9)	57 (248)	36 (248)	0.0975 (2700)

3.4.5 Matlab Code

A Matlab code was developed in order to automatically pre-process the creation of input files for the ABAQUS solver. The code generates the geometry and the mesh of the unit cell described on Fig. 3.2.

The meshing of the geometry, i.e., the position and numbering of S4 shell elements and nodes, is further described in Appendix B. Two data files are created to ease the modification of the input file, especially for parametric analyses. One contains the element connectivity, that is, a list of the element numbers along with the reference numbers of the four nodes attached to them. The other lists the node numbers along with their position in the (x_1, x_2, x_3) coordinate system.

The node sets for the top and bottom edges are automatically assigned the boundary conditions. The nodes on the side edges are organized in the correct manner in order to accommodate the applied the periodicity conditions (3.4).

A few parameters can be changed when running the Matlab program. In fact, if the user decides not to run the classic geometry and mesh, he needs to enter (see Figures 3.2 and 3.4):

- the length along the W direction (denoted as a)
- the length along the L direction (denoted as b)
- the height (denoted as h)
- the number of elements along the height (denoted as N_h)

One also needs to choose the type of analysis: bifurcation buckling, initial response, initial collapse response or complete crushing.

The input file and associated data files are then post-processed using ABAQUS.

3.5 BUCKLING, INITIAL POST-BUCKLING AND COLLAPSE BEHAVIOR

The buckling and initial collapse of the characteristic cell model were conducted using ABAQUS/Standard because of the efficiency and the accuracy it affords. The cell is loaded by prescribing incrementally the normal displacement of the top surface δ. A typical calculated compressive stress-displacement ($\sigma - \delta$) response is shown in Fig. 3.5, where σ is the force divided by the cell's projected area ($3\sqrt{3}\ell^2/2$, see Fig. 3.1). For this calculation a mesh of 18254 elements was used as both the critical stress and collapse stress have converged (see Section 4.2).

3.5.1 Elastic Buckling

The response is initially stiff and linear with stiffness E_3^* as quoted in (3.1). At some level of stress (σ_C = 428 psi—2.95 MPa) the plate-like walls of the cell buckle into the mode shown in Fig. 3.6a. It has three half waves along the height of the cell and is symmetric about the mid-height. Interestingly, the second buckling mode shown in Fig. 3.6b is anti-symmetric about the mid-height and occurs at only slightly higher stress of 434 psi (2.99 MPa). It is worth noting that higher modes are separated by larger stress levels. Buckling is clearly elastic as the honeycomb yields at a much higher stress level marked on the extended trivial response with a square symbol (σ_y = 947 psi—6.60 MPa). The critical buckling stress of 428 psi (2.95 MPa) compares with the upper bound value developed by Zhang and Ashby [1992] of 1249 psi (8.61 MPa) (see also §4.5 Gibson and Ashby, 1997). The bound was developed using a long strip of foil width ℓ and thickness t with fixed boundary conditions along the long edges. It is interesting to note that even if the sides had been assumed to be simply–supported, the buckling stress from this approach would still be significantly higher than the numerical value (717 psi—4.85 MPa; using K = 3.29 in Refs. Eq. (7)). Since the cell corners are not rigid, neighboring cells buckle in a compatible manner (see Fig. 3.7), which apparently makes the structure more flexible.

3.5.2 Post-Buckling and Collapse

Elastic buckling of plates has a stable post-buckling response and consequently the initial change in stiffness of the buckled structure is relatively small. Figure 3.8 shows deformed configurations corresponding to three points on the response marked with numbered bullets in Fig. 3.5. Configuration ① is in the pre-bucking regime and so the honeycomb does not exhibit out of plane deformations. In configuration ② the symmetric deformation of mode 1 is clearly discernible. The post-buckling response is of course nonlinear but the structure remains elastic until a higher stress level is reached. With further compression the combination of bending and membrane stresses yield the material and the response starts to lose stiffness deviating from the elastic one (drawn with dashed line). Plastification eventually results in the development of a load maximum in the response that represents the collapse load of the structure (σ_{CO} = 714 psi — 4.93 MPa). This value of collapse stress is somewhat higher than the average value measured in the experiments of 539 psi (3.72 MPa). Various imperfections present in real structures tend to reduce the collapse load (see imperfection sensitivity studies in Chapter 4). The effects of the size of the domain analyzed and of the mesh will also be discussed in the next chapter.

With further compression the deformation starts to localize while the average stress follows a downward trajectory. In configuration ③ in Fig. 3.8 the deformation is seen to localize, but remains symmetric about, the mid-height (compare amplitude of displacements at mid-height and elsewhere). The continuation of the collapse of the structure and the subsequent progressive folding of the walls will be discussed in the Section 3.6.

3.5.3 Imperfect Structure

At this stage it is also interesting to consider the response of an imperfect version of this unit cell. The imperfection chosen here corresponds to the first buckling mode (see Fig. 3.6a) with the point of maximum transverse deflection assigned an amplitude equal to t. The response of the imperfect structure, drawn in Fig. 3.5 with a dashed line, is seen to be initially somewhat less stiff than the one for the perfect geometry. The load maximum is 6.5% lower but at higher deformations it merges with the perfect case response.

In reviewing the literature we observed that the distinction between "buckling" and "collapse" is rather blurred. This is partly due to the fact that the onset of buckling in the cell walls is difficult to pinpoint experimentally. Measured responses appear more like the one for the imperfect cell model in Fig. 3.5 in which the point of buckling is impossible to identify. The best one can do is to bracket σ_C by careful monitoring the development of waves in the cell walls, something that is practically difficult and consequently not usually done. Instead, some quote the maximum stress recorded as "buckling." As reported above, the load maximum is caused by inelastic action due to the combined effect of cell bending and compression. In the present case inelasticity is loss of stiffness due to plasticity; in others it could be some type of damage that can lead to failure. In both cases a non-trivial calculation is required to pinpoint the load maximum. A reasonable lower bound may be established by calculating the onset of yielding due to combined bending and compression in the fashion proposed by Timoshenko. Finally, we note that if the cell walls are made thicker, buckling can occur in the plastic range of the material requiring a different treatment from the present one.

3.5.4 Wall Debonding

During the experiments, partial debonding of the double walls at mid-height was observed. This was seen to occur at the junction where single walls are bonded into double walls (rounded corners) and for an opening of about 10% of the height h (see configuration ① along W in Fig 2.6b). This effect was seen to happen at the early stages of the response of the structure, when the deformation localizes and the first-fold collapse begins. Further debonding was difficult to confirm at more advanced stages of crushing.

In the way of evaluating the effect of debonding on the buckling and collapse, the following analysis was performed. An initial debond of height of $h_o = 0.094h$ was introduced at mid-height of the unit cell model (see inset in Fig.

3.9a). Thus, in the sections of the model with thickness 2*t*, the debonded zones have two overlapping layers of shell elements with wall thickness *t*. The remainders are modeled with the usual single layer of shell elements with thickness 2*t*. Special attention had to be given to the connectivity of the elements of the two layers and those of the adjacent single thickness walls in order to allow for the expected separation of the walls to develop naturally. A mesh of 4224 S4 shell elements (see the reference case in Chapter 4) was adopted.

The bifurcation analysis performed using ABAQUS/Standard for this model gave the exact same mode and critical stress as for the base case with the same mesh. Since the initial stiffness of the original unit cell and the one with the debonds is the same, this result also confirms the correct connectivity of the shell elements in the model.

Figure 3.9a shows the stress-shortening response of the model with the debond along with the intact case. Both cases were assigned an initial imperfection in the form of the first buckling mode with amplitude *t*. Figure 3.9b shows three deformed configurations from each model. As expected, the initial elastic response is unchanged. At a level of stress of about 500 psi the two responses start deviating and the model with partial debonding reaches a significantly lower collapse stress (σ_{CO} = 582 psi). As collapse occurs, the double walls are seen in configurations ② and ③ in Fig. 3.9b to buckle outwards separating from each other. In the descending part of the response, the level of stress stays about 100 psi below the base case. The calculation was not continued into the crushing regime when contact of the debonded layers takes place.

We observe that in the present model, debonding was introduced a-priori. In the experiments, the debonding occurred following the limit load through a process involving wall separation through fracture. Despite this difference, the present results indicate that the collapse response is influenced by the debonding.

3.6 CRUSHING RESPONSE

Honeycomb crushing involves severe local bending of and contact between the walls of the folds. Consequently, in contrast to the pre-buckling and initial post-buckling calculations described in Section 3.5, crushing was performed using ABAQUS/Explicit due to the computational efficiency that it affords. The basic calculations involve the characteristic cell shown in Fig. 3.2 with a mesh of 5850 S4 elements (convergence study will follow in Chapter 4). The cell is assigned the periodicity conditions given in (3.4). The top and bottom edges are fixed except in the x_3-direction of the top edge, which is prescribed a downward displacement. This displacement was assigned a "smooth step" time function in order to minimize inertial effects, thus mimicking the "quasi-static" rate of crushing of the experiments. Furthermore, the computation time was minimized by speeding up the simulation to a total crushing time of 2 seconds. For this choice of crushing time the kinetic energy of the structure was shown to remain only a small fraction of the strain energy, thus confirming that the simulation remained “quasi-static.” The same time independent constitutive model described in Section 3.4 was adopted for the mechanical properties of the Al-5052-T4 alloy.

3.6.1 Contact Properties

The crushing involves contact between folds of adjacent cell walls as well as self-contact and consequently both sides of the cell walls were considered for contact (ABAQUS’ “all exterior” parameter). This process ensures that contact occurs at the actual surface of the walls (i.e., at $\pm t/2$). It suffices to say that for such problems contact constitutes a major contributor to the total computation time of the simulation.

3.6.2 Crushing Response and Folding Process

A typical crushing response from such a simulation is shown in Fig. 3.10 along with one of the experimental responses. Figure 3.11 shows L and W pairs of views of the initial and a set of deformed configurations of the unit cell corresponding to the numbered bullets marked on the response in Fig. 3.10. An initial imperfection corresponding to the first buckling mode (Fig. 3.6a) with amplitude of *t* was included in the model to ensure consistency in the initial mode of collapse with the results shown above. Configurations ①, on the first descending part of the response, shows localized deformation symmetrically deployed about the mid-height that is associated with the initial stages of collapse of the cell. The local buckles that have formed are inward in the W side and outward in the L side. Simultaneously, the walls above and below the collapse are seen to be relatively undeformed. In the experiments the first sign of some debonding of double walls was observed at this stage. Wall separation was precluded in this model and this omission is expected to introduce some minor differences between the calculated and measured responses.

The collapse continues with folding up the local buckles at mid-height while the load is decreasing. In the neighborhood of configuration ②, contact between folds in adjacent walls develops for the first time. The structure is stabilized and this is reflected in the bottoming out of the response. In the neighborhood of configuration ③, self-contact in the folds takes place further stabilizing the structure and the load takes an upward trajectory (note that the images show the mid-surface of the cell). It is reassuring that the depth of the load trough is similar (slightly higher) to that of the experiment.

The inflection point that was consistently seen in the experiments is reproduced in the simulation but is less distinctive. We speculate that in the physical test it may be a manifestation of the contact of the separated parts of the double walls that can be seen in configuration ③ in Fig. 2.6b. In configuration ④ some of the folds have developed self-contact and the upward trend in the load continues. At some point the thus far intact part of the upper half of the cell gets destabilized once more; a new load maximum develops and a second fold is initiated from the disturbance provided by the bent walls of the first one. The new fold can be seen at a well-developed state in ⑤. The second load peak is at a slightly higher level than the experimental one. By configuration ⑥, contact is fully developed in the second fold and the response takes an upward path once more. A third load peak develops at about the same level as the second one. This is associated with the initiation of a third fold again in the upper half of the cell that can be seen in configuration ⑦. Contact arrests the deformation in the third fold and the response recovers once more. Configuration ⑧ shows the third fold fully developed and the stiffening of the response once more. A fourth load peak develops which signals the commencement of folding in the lower half of the cell which can be seen in configuration ⑨ just before the next load valley. The folding in the lower half continues forming a total of five folds before densification, which agrees with the experiment. However, the experimental response associated with the final folding differs from the simulation primarily because of the presence of the epoxy fillets that form at the interfaces with the plates.

Overall, the simulated crushing response is a reasonable reproduction of the experimental one all be it with some differences. The crushing stress ($\bar{\sigma}_{ch}$ = average σ between $0.225 \le \delta / h \le 0.60$) is 257 psi (1.77 MPa), that is 8.4% higher than the mean value from the experiments. The period of the folds is somewhat different than the experimental one and the decay in the amplitude of the stress undulations was not captured here as stress peaks 2, 3 and 4 occur at about the same level. Furthermore, small amplitude undulations associated with local events within the folds appear in the calculated response making it more rugged. Of course, the experimental response represents the average over many cells (at least 8×15), which tends to smooth out local force fluctuations.

Chapter 4

Parametric Study

In this Chapter the two major aspects of honeycomb compressive behavior, buckling and collapse, and crushing, are considered once again but now emphasizing their sensitivity to various problem parameters. The parameters considered include the mesh, the size of the domain analyzed, and several types of geometric and other imperfections.

4.1 BASE CASE

We first define a "Base Case" that will form the basis of the comparisons that follow. The base case consists of the unit cell defined in Section 3.2 with a perfect geometry (see Figs. 3.1, 3.2 and Table 3.1). The geometry is meshed with 4224 nearly square fully integrated S4 shell elements; i.e., 64 elements along the height, 22 along the length of the center wall, and 11 along the length of the truncated side walls. The calculations are done considering three Gaussian integration points through the shell thickness. The boundary and periodicity conditions are applied in the way described in Sections 3.4.2 and 3.4.3; the mechanical properties adopted are the same as outlined in Section 3.4.4.

For the bifurcation analyses and the collapse load calculations, the code was run in ABAQUS/Standard, while for complete crushing calculations ABAQUS/Explicit was preferred for the reasons explained in Chapter 3 (with a smooth step displacement function and a simulation time of two seconds). Unless otherwise stated, both collapse and complete crushing calculations were done with an initial imperfection corresponding to the first buckling mode with three half-waves and maximum lateral amplitude of t. As an example, Fig. 3.6a shows the mode considered in the case of a single cell. Table 4.1 summarizes the values of the key parameters of the base case.

The calculated buckling, collapse, and average crushing stresses of the base case are reported in Table 4.2 below. These results will be used to normalize similar results from calculations that follow in the parametric studies that are performed.

Table 4.2 Critical stresses calculated using base case

Reference	σ_C psi (MPa)	σ_{CO} psi (MPa)	$\bar{\sigma}_{ch}$ psi (MPa)
Base case	437 (3.02)	667 (4.60)	273 (1.88)

The number of Gaussian integration points through the shell thickness used for the base case (three) was determined from a parametric study of this issue reported in Table 4.3. As expected, increasing this number does not change significantly the buckling and collapse stresses. The average crushing stress slightly increases with the number of integration points N_{IP}, but corresponding stress-shortening responses are nearly identical as shown for the two cases shown in Fig. 4.1.

Table 4.3 Critical stresses calculated for different numbers of through thickness Gaussian integration points

N_{IP}	σ_C psi (MPa)	σ_{CO} psi (MPa)	$\bar{\sigma}_{ch}$ psi (MPa)
3 (Base case)	437 (3.02)	667 (4.60)	273 (1.88)
5	437 (3.02)	667 (4.60)	281 (1.94)
7	437 (3.02)	667 (4.60)	284 (1.96)
9	437 (3.02)	667 (4.60)	285 (1.97)

4.2 PARAMETRIC STUDY OF BUCKLING AND COLLAPSE

4.2.1 Effect of Mesh Density

The effects of the characteristic cell mesh density on the bifurcation and collapse stresses was examined and the results are shown in Fig. 4.2, where the two variables are plotted against the number, M, of S4 elements. In all cases the mesh is nearly square. The calculated critical loads are normalized by the bifurcation buckling stress, "σ_C", of the base case which is 437 psi (3.02 MPa;

normalized value designated as $\bar{\sigma}_C$). The coarsest mesh considered has 870 elements, the second 2208, the third 4224 and so on. The buckling stress is seen to gradually decrease with M so that for 870 elements it is 4.5% higher than σ_C and for 18254 elements it is 2% lower; this last case can be considered as converged. In other words, the base case is not fully converged as far as this variable is concerned; instead it has been chosen for computational expediency in the execution of very large calculations that follow. It is important to note however that the mode associated with the critical stress remained the same for all meshes.

The calculated $\bar{\sigma}_{CO}$ $(= \sigma_{CO} / \sigma_C)$ values are seen in Fig. 4.2 to be less sensitive to the mesh so that even for the coarsest mesh the value is only 0.6% higher than the base case value. Furthermore, for $M > 4224$ the results can be considered to have converged.

4.2.2 Effect of Domain Size

As is well known, in periodic structures both the mode and the critical buckling stress can be influenced by the size of the periodic domain considered; or in other words, criticality can involve more than one characteristic cell. Geymonat *et al.* [1993] developed a method based on Bloch wave theory that automates the search for the critical state (see application to a Kelvin foam in Gong *et al.*, 2005). The method uses the stiffness matrix of the characteristic cell, which for the present problem is large (51000^2 for the unit cell) making the automation afforded by the method difficult to exploit. For this reason here we opt for a more limited examination of the effect of the domain size that involves direct analysis of periodic domains of different sizes.

In the way of evaluating the effect of the domain size we calculated the critical buckling and collapse stresses of periodic rows of N cells in the W and L directions. Results for rows of 1 to 8 cells are plotted in Fig. 4.3. In the L direction the buckling stress drops slightly as N increases but appears converged after $N = 5$ at a value that is about 4.5% lower than that of the base case. In the W direction the effect of N on the buckling stress is larger so that it is reduced by about 10% for $N \geq 6$. Figures 4.4a and 4.4b show renderings of the buckling modes for N_L and N_W of 4. The shapes of the modes are the same as for the single cell but the amplitude of the waves is more pronounced in the central cells. Similar variation in amplitude was also observed for longer domains. Included in Fig. 4.3 are the normalized collapse stresses for W and L rows of periodic cells. Interestingly, this value increases slightly (less than 4%) with N but is essentially constant for $N \geq 4$. It is worth noting that the collapse stress of the corresponding perfect domains remained essentially unchanged with the values of N_L and N_W.

In the same spirit we considered periodic square domains with $N_L \times N_W$ $(= n)$ cells. The buckling and collapse stresses are plotted against n in Fig. 4.5 for $1 \leq n \leq 64$ (solid lines). Here the number of cells in the periodic domain impacts the buckling stress more significantly; thus, for $n = 36$ the buckling stress is reduced by nearly 19% and remains essentially unchanged for larger *n*. The critical buckling mode for *n* = 16 is shown in Fig. 4.4c. Once more the mode imparts the same shape to each cell but the amplitude is more intense in the central cells. This pattern was observed in the larger domains considered also. The collapse stress for $w_o = t$ is seen to be insensitive to *n* for all but the smallest domains.

For domains larger than *n* = 16 calculations were also performed by removing the periodicity conditions from the edges, in other words we considered finite size square domains. The first observation is that the buckling mode consisted of three half waves as in the periodic domains. The corresponding buckling stresses are included in Fig. 4.5 with a dashed line and are seen to be very comparable to the results from the periodic domains. As expected the two sets of results converge as *n* becomes larger. The collapse stresses were also calculated for these cases using again an imperfection with amplitude *t*. The results are included in Fig. 4.5 and are seen to be slightly lower than those from the periodic domains.

4.2.3 Effect of Imperfections

As noted earlier, the collapse stress calculated for a characteristic cell with perfect geometry was higher than the values measured in all of our experiments. It is thus worth examining the effect of various imperfections on this variable (see also Chen *et al.*, 2009). The most natural one is a geometric imperfection in the form of the critical buckling mode shown in Fig. 3.6a. Figure 4.6 shows the collapse stress of the characteristic cell vs. the amplitude of the imperfection normalized by the foil wall thickness (see inset in Fig. 4.6). An imperfection with amplitude of t reduces σ_{CO} by 7% and for $3t$ by 17%. In other words, the structure is modestly sensitive to this imperfection.

In our experiments the panels were compressed between stiff parallel (nearly) platens. Although care was taken to make the platens as parallel as possible, small misalignments were observed and are thought to have influenced the measured collapse stress. The effect of one directional platen misalignment on the collapse pressure was analyzed using a 6×6 periodic cell. The calculated collapse stresses for $w_o = t$ are plotted in Fig. 4.7 against the single direction misalignment angle ϕ. The results show that even very small misalignments can cause a reduction in σ_{CO}. As might be expected, the direction of the misalignment also influences the collapse stress with larger reduction taking place when ϕ is oriented in the W direction. Thus for example, for $\phi_W = 0.03^{\circ}$ the collapse stress drops by about 5% and for 0.06° by about 11%.

Papka and Kyriakides [1994, 1998] reported that the shape of expanded honeycomb cells can differ from the perfect hexagonal geometry considered this far. The bond lines that are initially printed on the foil sheets can deviate from the ideal value so that on expansion the hexagonal cells are distorted in the fashion shown in Fig. 2.3. In addition, honeycomb can be somewhat under- or over-expanded. These two manufacturing “imperfections” affect the density of the honeycomb as well as all its mechanical properties. Measurements performed on the honeycomb used in this study showed that the value of the cell width c was consistently very close to the ideal value of 0.375 in (9.53 mm). However, some variations in the bond line length were found. For this reason we used unit cell calculations to examine how the bond line length affects the buckling and collapse stresses. Figure 4.8 shows plots of calculated buckling and collapse stresses against the bond line deviation parameter λ ($0.8 \leq \lambda \leq 1.05$ with 1 representing the ideal bond line length). Both critical stresses decrease for $\lambda < 1$ and increase for $\lambda > 1$ with the buckling stress being affected more by this variable than σ_{CO}.

4.3 PARAMETRIC STUDY OF CRUSHING

4.3.1 Effect of Mesh Density

Next we conduct a limited parametric study of the crushing response as a whole as well as the crushing stress as defined in Fig. 2.7. Figure 4.9 compares the crushing responses of a single characteristic cell using three different nearly square mesh densities. As reported above, the collapse is not particularly sensitive to the mesh densities considered here (see Table 4.4). The subsequent crushing response however is seen to be the highest for 2700 elements, lower for the base case mesh of 4224 and slightly lower yet for 5850. Consequently the crushing stresses calculated for each also differ as shown in Table 4.4. The formation of the sharp folds associated with crushing requires a fine enough mesh for it to be accommodated. Indeed, some of the details of the folding tend to differ when the mesh is not sufficiently refined. These numbers compare with an average crushing stress of 241 psi (1.66 MPa) from our experiments.

4.3.2 Effect of Domain Size

The effect of the domain size on the crushing response was evaluated using the following periodic domains: $\{N_W \times N_L\} = \{1\times 1,\ 1\times 4,\ 4\times 1,\ 4\times 4\}$, with each cell in each domain having the same mesh as the base case (4224 elements). The stress-shortening results are plotted in Fig. 4.10 together with one of the experimental responses. Figure 4.11 shows four deformed configurations of the 4×4 domain corresponding to the numbered bullets on the response in Fig. 4.10. Once again, the four collapse stresses differ by a small amount (see Table 4.5) with the larger domains having somewhat higher values. The initial collapse responses through the first stress trough and up to the second load peak are identical. This is because deformation localizes in the same manner at mid-height for all domains (e.g., compare ① in Figs. 4.11 and 3.11a). The formation of the first fold is also similar (e.g., compare ② in Figs. 4.11 and 3.11a). Differences between the responses from the three smaller domains and the larger one (4×4) start with the formation of the second fold. While for the first three domains the second fold occurs strictly on either the top or the bottom half of the height (see ⑤ and ⑥ in Fig. 3.11b), the events for 4×4 are different (corresponding configurations from 1×4 and 4×1 domains are very similar to the results in Fig. 3.11b and are not included here for brevity). Careful examination of configuration ③ in Fig. 4.11 shows that the position of the second fold differs from the left to the right. On the left it is developing in the lower half of the cells and on the right in the upper half. The third load peak occurs at the same displacement for all domains but it is distinctly lower for the larger one. Configuration ④ in Fig. 4.11 shows the crushing at a more developed stage, and at the same time illustrates even more clearly the difference in the crushing patterns across the domain. It is worth noting that the difference in the crushing patterns develop inside the domain as opposite edges must maintain the imposed periodicity conditions. Thus, for the observed difference in folding patterns to develop, several folds are inclined something that is not observed in the smaller domains. Note that such a variation in the position of folding along the height of the specimens was also observed in most of the crushing experiments performed al be it in much larger domains with free edges.

The response of the larger domain continues to deviate from the others at larger values of δ with the last load peak being even lower than those of the other three domains. Another difference is that the larger domain response is less rugged. The decay in the amplitude of the stress undulations as well as the smoothness of the response of the larger domain are both features that are observed in the experimental responses also (e.g., see case included in Fig. 4.10).

Apparently, these aspects of the response are related to the variation in the crushing patterns within the domain. This variation causes the collapse of cells and the contact between the walls of the folds to occur at somewhat different times across the domain; these have the effect of first smoothening the response and second of causing a decay in the amplitude of the average stress undulations. At the same time however the average stresses of the responses of the four domains considered do not differ as is evident from the crushing stresses reported in Table 4.5.

The 4×4 domain discussed is already rather large and computationally intensive. Larger domains were considered and the trend was similar. Crushing of large domains with free edges was not performed as experimentally the effect of the free edges was found to be modest at least for the sizes considered.

In summary then, the crushing of a single characteristic cell and of small linear domains results in stress undulations of nearly the same amplitude and in more ragged responses. Switching to a square domain of 4×4 cells smoothens the response and causes a progressive decay in the stress undulations, both features that were observed in the experiments. However, all domains considered yielded about the same crushing stress, which happens to be somewhat higher than the measured values. One cause of this difference may be the debonding observed to occur at least during the formation of the first fold in the experiments; debonding was not included in the crushing calculations.

4.3.3 Effect of Imperfections

The effect of two types of imperfections on the crushing response and the average crushing stress is now evaluated using a single cell. The first geometric imperfection considered is in the form of the first buckling mode. This imperfection resulted in relatively small changes in both the crushing response and in the average crushing stress. Figure 4.12 shows the crushing responses of the base case for three different imperfection amplitudes: w_o = 0.1t, t, and 2t. Table 4.6 reports the calculated average crushing stresses for five different amplitudes of such imperfection. The results demonstrate that the initial modal imperfection has a very mild effect on the crushing response of the honeycomb. However, it is important to recall that it has a more important effect on the reduction of the collapse stress as described earlier.

The imperfect hexagonal geometry introduced from an incorrect bond length of the double walls showed larger but still mild differences on the crushing. Simulations for several values of λ between 0.80 and 1.05 were run and the corresponding crushing stresses are listed in Table 4.7. Figure 4.13 compares three of these responses. The four first load peaks in the responses are similar, while larger differences appear after a shortening of about 0.55. In fact, a fifth load peak at a shortening of 0.65 was clearly perceivable for the case with $\lambda = 0.85$. The numerical results Table 4.7 indicate that small values of λ yield smaller crushing stresses. These results are not surprising as crushing the cell with longer double thickness walls and shorter single thickness ones requires a higher level of stress; the change in the projected area of the cell with λ is actually not significant in comparison to the change in force.

Chapter 5

Summary and Conclusion

This thesis reported results from a comprehensive study of the compressive response and crushing of Al-5052-H39 honeycomb panels. The honeycomb used were manufactured by an expansion process that results in double thickness walls in one direction; they had a cell size of 0.375 in (9.53 mm), a relative density of 0.026, and a height of 0.625 in (15.9 mm).

5.1 MAIN EXPERIMENTAL FINDINGS

Finite size panels of the order of 8×15 cells or larger were compressed quasi-statically between flat platens. Following an initial linear response, the cell walls buckle elastically. The post-buckling response is initially stiff and stable but inelastic action progressively softens it leading to a limit load instability. Deformation localizes first at mid-height in the form of a sharp buckle, and morphs into a fold with the load continuing to drop. When the walls of the fold come into contact local collapse is arrested, the load begins to recover, and a second fold develops on one side of the first one. The second fold in turn collapses forming a new load peak and a second trough. This progressive folding keeps repeating until the whole panel is consumed and the structure returns to a stiff response.

Panels of different sizes were tested and showed great repeatability of the measured responses, even though the non-uniformity of the crushing patterns inside the specimens were different from one experiment to another. Differences appeared when comparing the collapse and crushing between sandwich panels and pure honeycomb. A significant reduction in the collapse stress was seen for the bonded specimens, as well as an earlier densification due to the epoxy. The collapse stresses and crushing stresses were measured to be in average 539 psi (3.72 MPa) and 241 psi (1.66 MPa) for the sandwich specimens, and 631 psi (4.35 MPa) and 220 psi (1.51 MPa) for the pure honeycombs, respectively.

5.2 NUMERICAL SIMULATIONS

The compressive response including the buckling, collapse and crushing have been simulated numerically using finite element models of various domain sizes. The models idealize the microstructure as hexagonal, with double walls in one direction. Several of the properties of interest can be extracted using a characteristic cell that exploits the periodicity of the microstructure. Closed form expressions for the elastic moduli from the literature were compared to the numerical predictions and found sound. Buckling was confirmed to occur in the elastic regime of the material at stress levels that are much lower than values reported in the literature that are based on simplistic models. The post-buckling response is stable and stiff as is expected from the plate like strips that constitute the walls of the hexagonal cells. Combined membrane and bending stresses eventually yield the material and the response develops a limit load, which represents the compressive strength of the honeycomb. For the particular honeycomb studied, the collapse stress was 67% higher than the buckling stress.

The buckling and collapse stresses were found to be sensitive to some degree to the mesh density used. The collapse stress was shown to be mildly sensitive to geometric imperfections including small misalignment of the compression platens used in the crushing. In view of this sensitivity the predicted collapse stress is considered to be in good agreement with measured values.

Beyond the limit load, deformation localizes first into a single sharp buckle at mid-height as was observed in the experiments. With further compression the buckle evolves into a fold. The downward trajectory of the response stops when the walls of the fold come into contact. The response then returns to positive stiffness and remains so until a second fold starts to develop either above or below the first one precipitating a second load peak followed by a stress valley. The load recovers again when a third fold develops and this repeats until the whole domain is folded up. In the experiments, the amplitude of such stress undulations consistently decayed as the crushing progressed, whereas in the single cell predictions it stayed nearly unchanged. The mean value or crushing stress however was found to be about 8% higher than the average of 8 experimental values. This level of agreement however came only with the use of a fine mesh, which is required in order to capture the details of the sharp folds. Another difference between the single cell predictions and the measurements is the much more ragged nature of the calculated response. The debonding observed in the experiments to occur at least during the formation of the first fold was not modeled in the crushing simulations. A collapse stress calculation with initial debond showed that it reduces the level of stress during the formation of the first fold.

The size of the periodic domain considered in crushing calculations was found to influence the results as follows. When a 4×4 cell periodic domain was crushed, the buckling and initial localization that follows collapse were found to replicate those of the single cell. However, the height location of the subsequent folding varied across the domain, a feature that is commonly observed in experiments. This variation in the location of the folds had the result of first smoothening the crushing response and second of introducing a decay in the amplitude of the stress undulations, both features that mimic the experimental results. The mean value of the stress undulations however, in other words the crushing stress, remained unaffected.

In view of the results presented it is concluded that the compressive response of honeycomb from the initial elastic part, through buckling, collapse and crushing can be evaluated with engineering accuracy using one characteristic cell. It is pointed out however that the crushing response requires a fine mesh for it to be accurate enough.

5.3 RECOMMENDATIONS FOR FUTURE WORK

The present thesis reported experimental and numerical results of the axial crushing of aluminum honeycomb, following the work done by Floccari [2008]. Floccari [2008] also studied experimentally the response of honeycomb under combined loadings including displacement controlled axial-crushing and constant shear. Further numerical simulations may consider such combined loadings.

The partial debonding that was seen to occur during the experiment was only included in one example simulation as an initial debond. More precise modeling of this effect, including complete crushing simulations may improve the understanding of the phenomenon.

The epoxy fillets at the bonded interface between the honeycomb core and the aluminum faceplates were seen to influence the point of densification in the experiments. Inclusion of the fillets in future models could clarify this issue.

Finally, the expansion process through which honeycomb is manufactured introduces small geometric variations, residual stresses, and changes in mechanical properties. This effect was not included in the present work and can also be studied for completeness.

Table 2.2 Geometric dimensions of honeycomb used in the experiments

Exp. ref.	Bonded faceplates	L_L in (mm)	L_W in (mm)
Floccari [2008]	Y	5.5 (140)	3.2 (81)
A-HC-1	Y	5.21 (132)	3.25 (83)
A-HC-2	Y	5.57 (141)	3.55 (90)
A-HC-3	Y	5.37 (136)	3.27 (83)
A-HC-4	Y	6.34 (161)	6.73 (170)
A-HC-5	Y	5.39 (137)	3.27 (83)
A-HC-6	Y	5.41 (137)	3.32 (84)
A-HC-7	N	5.38 (137)	3.29 (84)
A-HC-7bis	N	5.49 (139)	3.24 (82)
A-HC-7ter	N	5.34 (136)	3.28 (83)
Average (Except A-HC-4)	Y & N	5.41 (137)	3.30 (84)

Table 2.5 Average values of collapse and crushing stresses from experiments

Exp. ref.	Bonded faceplates	σ_{CO} psi (MPa)	$\overline{\sigma}_{ch}$ psi (MPa)
Floccari [2008]	Y	529 (3.65)	254 (1.75)
A-HC-1	Y	605 (4.17)	249 (1.72)
A-HC-2	Y	556 (3.83)	240 (1.65)
A-HC-3	Y	558 (3.85)	238 (1.64)
A-HC-4	Y	509 (3.51)	236 (1.63)
A-HC-5	Y	534 (3.68)	240 (1.65)
A-HC-6	Y	487 (3.36)	229 (1.58)
Average	Y	539 (3.72)	241 (1.66)
Standard deviation	Y	38.1 (0.263)	8.3 (0.0572)

Table 2.6 Average values of collapse and crushing stresses from experiments

Exp. ref.	Bonded faceplates	σ_{CO} psi (MPa)	$\overline{\sigma}_{ch}$ psi (MPa)
A-HC-7	N	627 (4.32)	218 (1.50)
A-HC-7bis	N	641 (4.42)	221 (1.52)
A-HC-7ter	N	624 (4.30)	N.A.
Average	N	631 (4.35)	220 (1.51)
Standard deviation	N	9.1 (0.06)	2.1 (0.01)

Table 4.1 Parameters used in the reference case

Parameter	Symbol	Value
Cell size	c	0.375 in
Height	h	0.625 in
Wall thickness	t	0.00374 in
Deficient bond length	λ	1
Num. of cells	n	1
Num. of elements	M	4224
Element type	EL	S4
Num. of integration points	N_{IP}	3
Explicit time	T	2 sec

Table 4.4: Calculated collapse and crushing stresses for different mesh densities

Element No.	σ_{CO} psi (MPa)	$\overline{\sigma}_{ch}$ psi (MPa)
2700	668 (4.61)	330 (2.28)
4224	667 (4.60)	267 (1.84)
5850	667 (4.60)	257 (1.77)

Table 4.5: Calculated collapse and crushing stresses for different periodic domain sizes

Domain Size $N_W \times N_L$	σ_{CO} psi (MPa)	$\overline{\sigma}_{ch}$ psi (MPa)
1×1	667 (4.60)	267 (1.84)
1×4	684 (4.72)	265 (1.83)
4×1	688 (4.74)	265 (1.83)
4×4	699 (4.82)	271 (1.87)

Table 4.6 Average crushing stresses calculated for different amounts of modal imperfection

w_0	$\bar{\sigma}_{ch}$ psi (MPa)
$0.1t$	269 (1.85)
$0.5t$	271 (1.87)
t	273 (1.88)
$2t$	271 (1.87)
$3t$	275 (1.90)

Table 4.7 Average crushing stresses calculated for various imperfect bond lengths

λ	$\bar{\sigma}_{ch}$ psi (MPa)
0.80	258 (1.78)
0.85	255 (1.76)
0.90	254 (1.75)
1.00	273 (1.88)
1.05	281 (1.94)

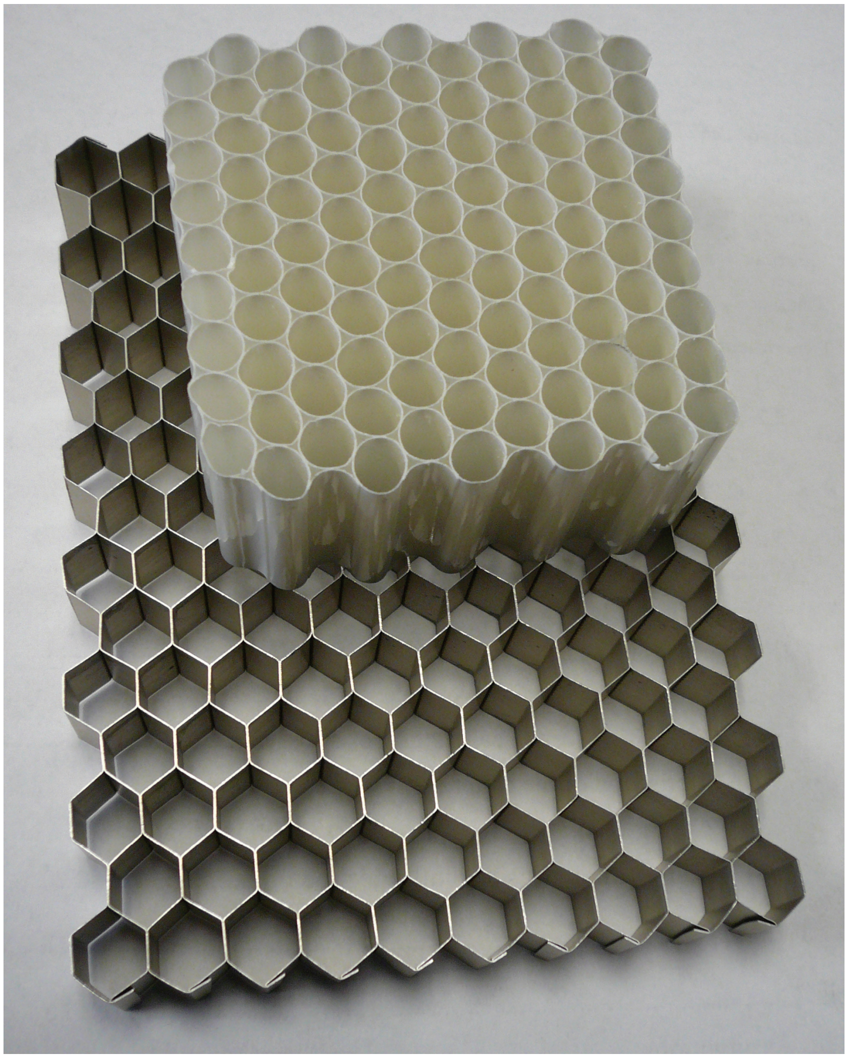

Figure 1.1: Photograph of two honeycombs with circular and hexagonal cells.

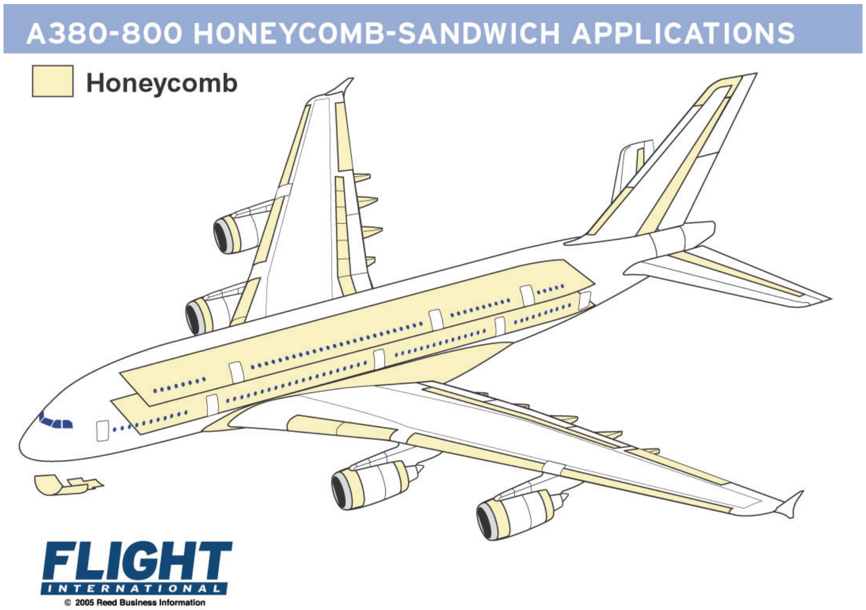

(a)

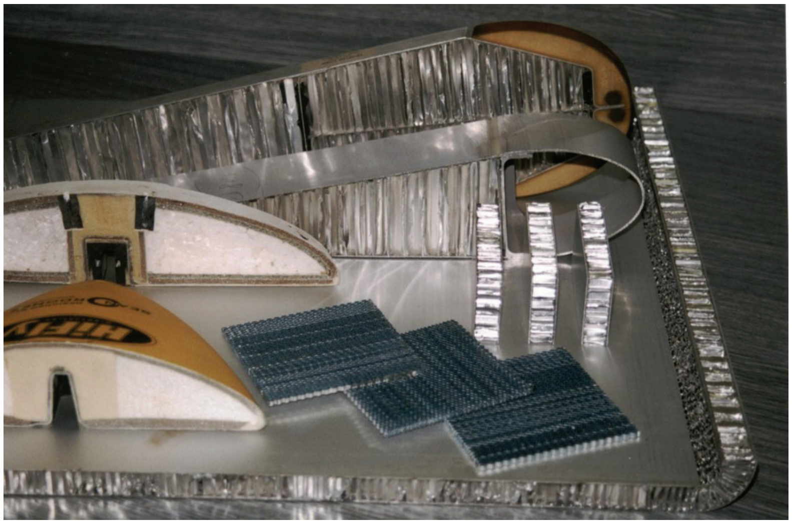

(b)

Figure 1.2: Examples of uses of honeycomb in (a) Airbus A380 airplane (Flight International, 2005) and (b) aircraft structures (5M, 2010).

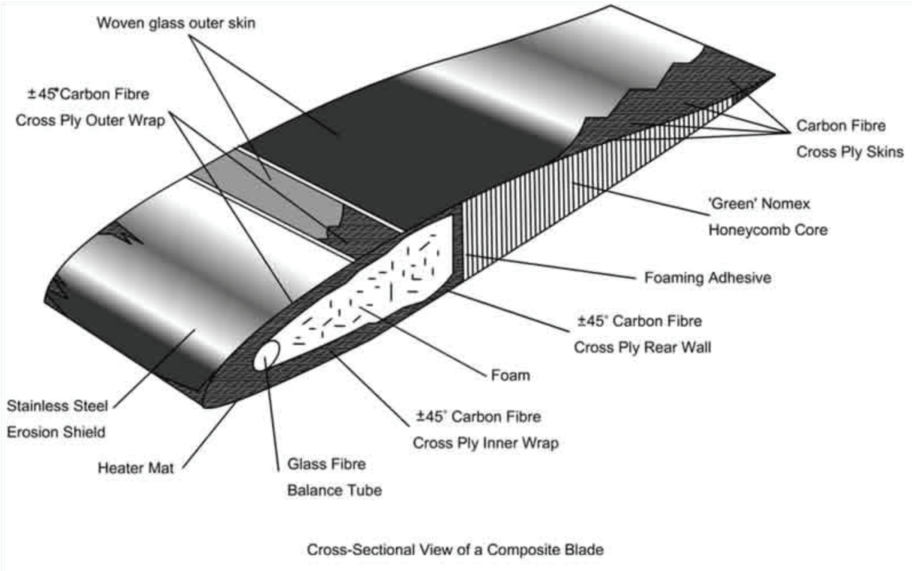

(a)

(b)

Figure 1.3: Examples of uses of honeycombs in (a) helicopter blades (UK Center for Materials Education, 2010) and (b) stealth Visby class corvette (Defense Industry Daily, 2008).

Figure 1.4: Pininfarina Nido concept car presented in 2004, and exploring new concepts in the field of safety with honeycomb energy absorbers (Car Body Design, 2008).

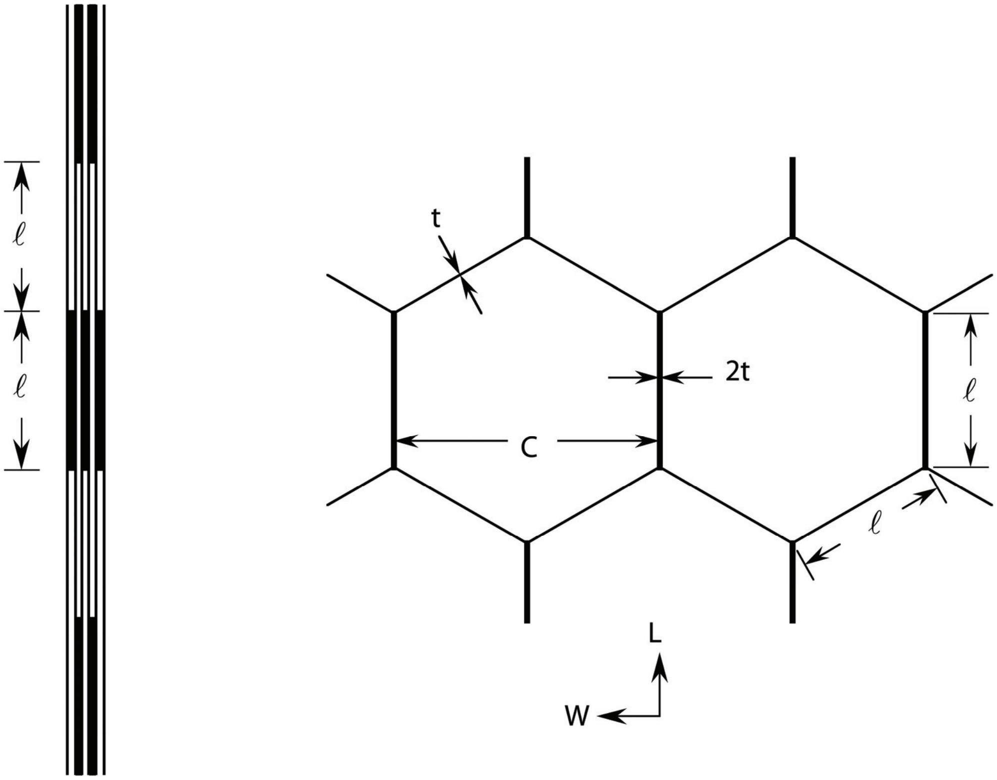

(a) (b)

Figure 1.5: (a) Laminate of periodically bonded aluminum sheets and (b) hexagonal honeycomb microstructure.

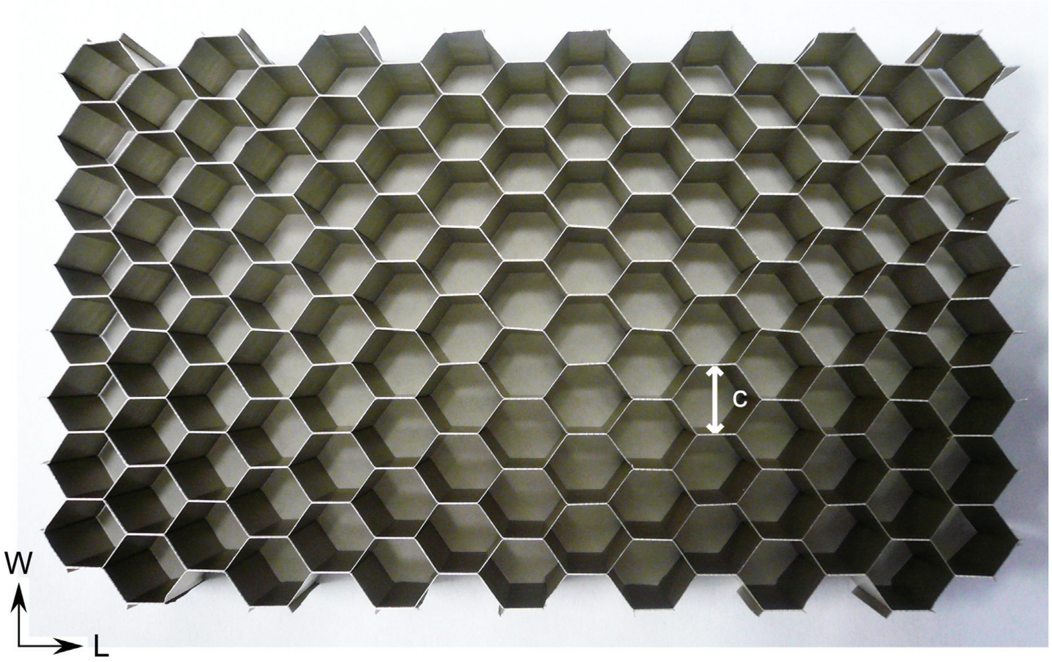

Figure 2.1: Photograph of a honeycomb sample of 8 x 15 cells.

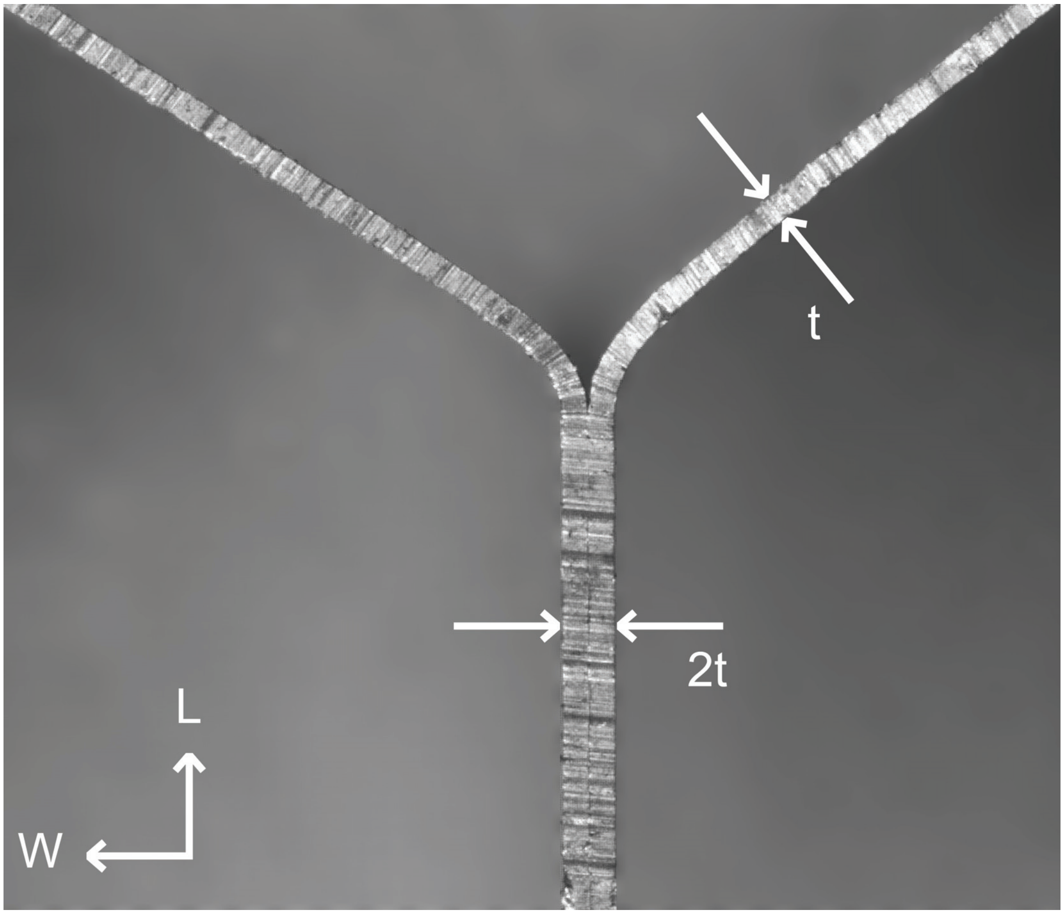

Figure 2.2: Expanded view showing the rounding at cells corners.

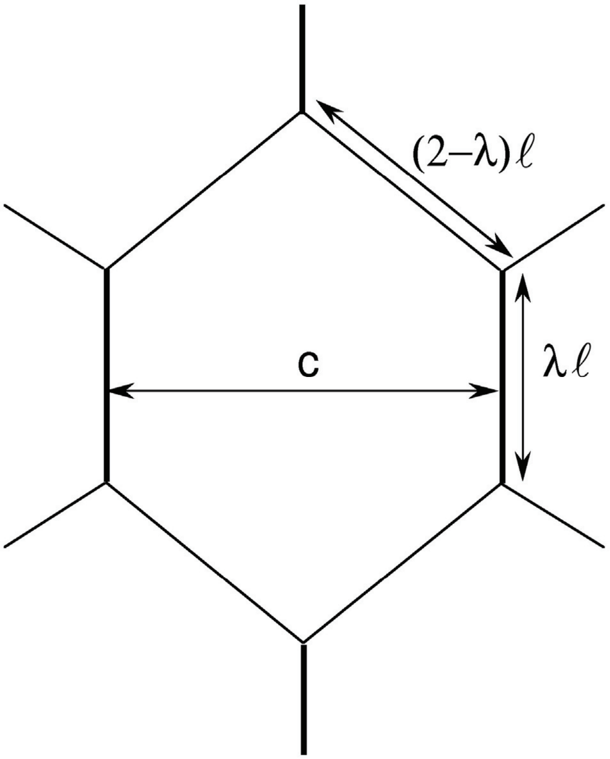

Figure 2.3: Geometry of imperfect hexagonal cell with deficient bond length.

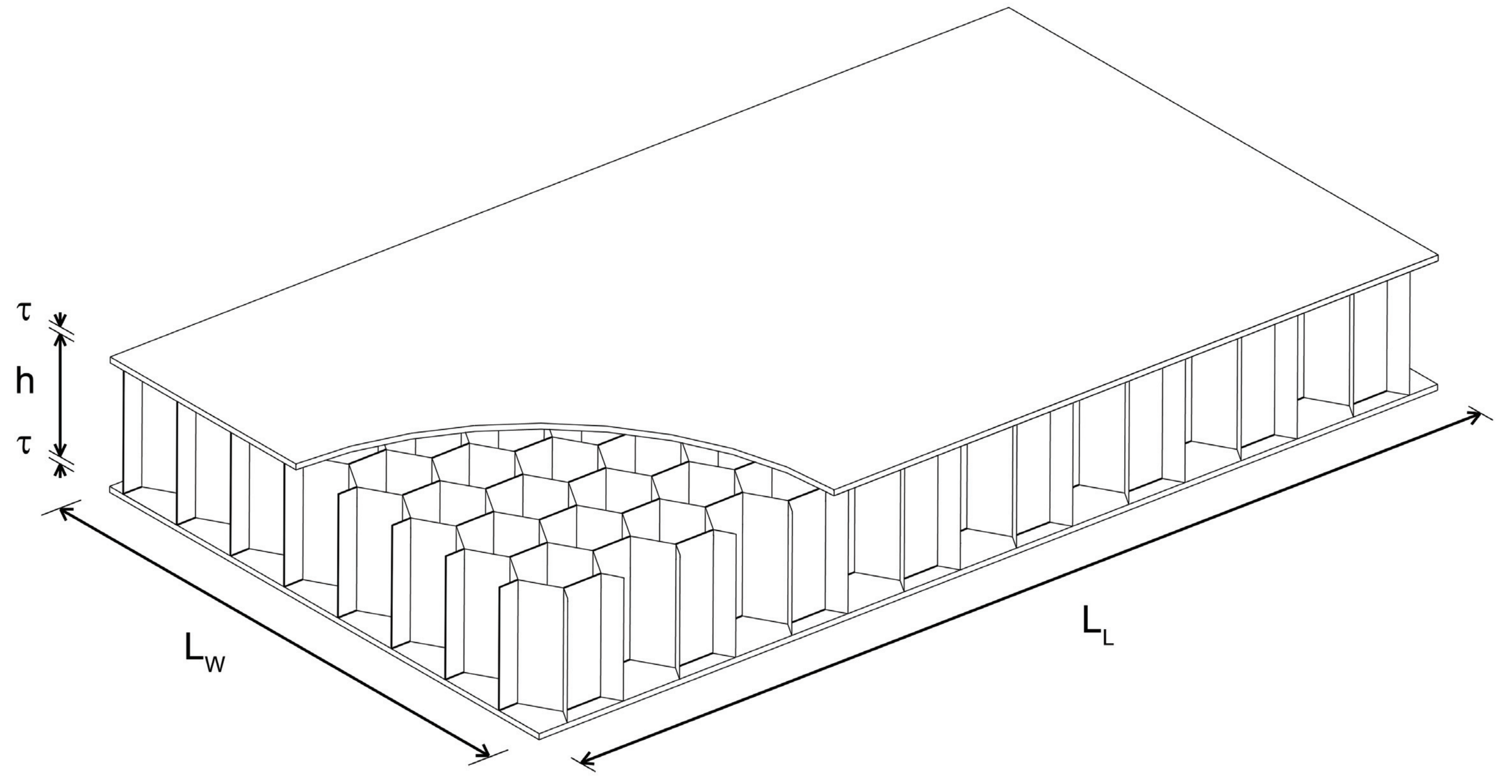

Figure 2.4: Three-dimensional rendering of a honeycomb sandwich panel.

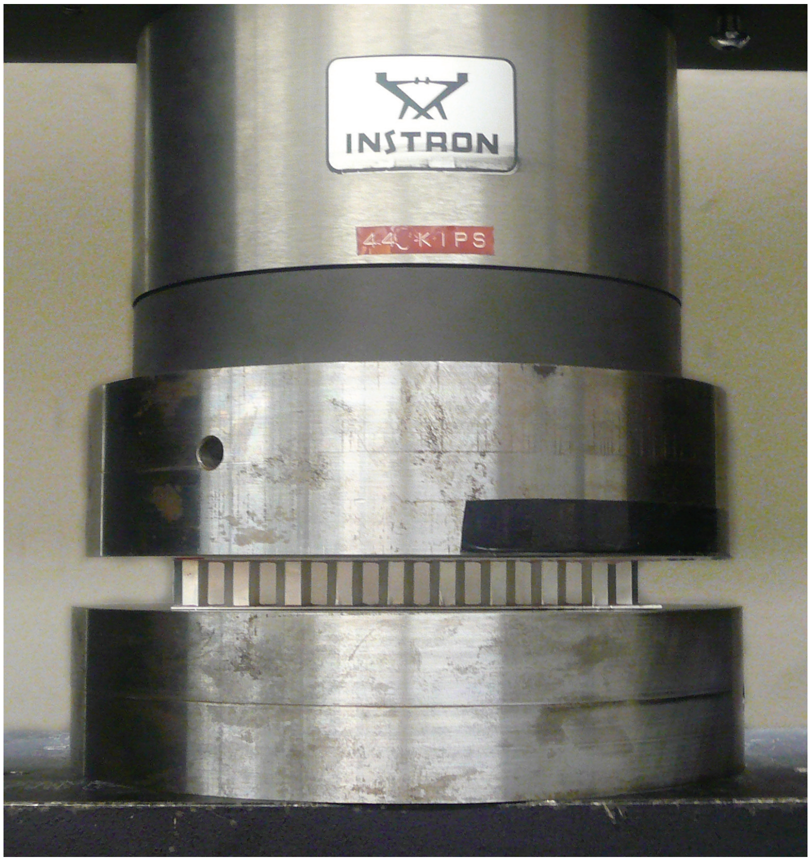

Figure 2.5: Photograph showing a panel between stiff platens in a universal testing machine where the crushing experiments were conducted.

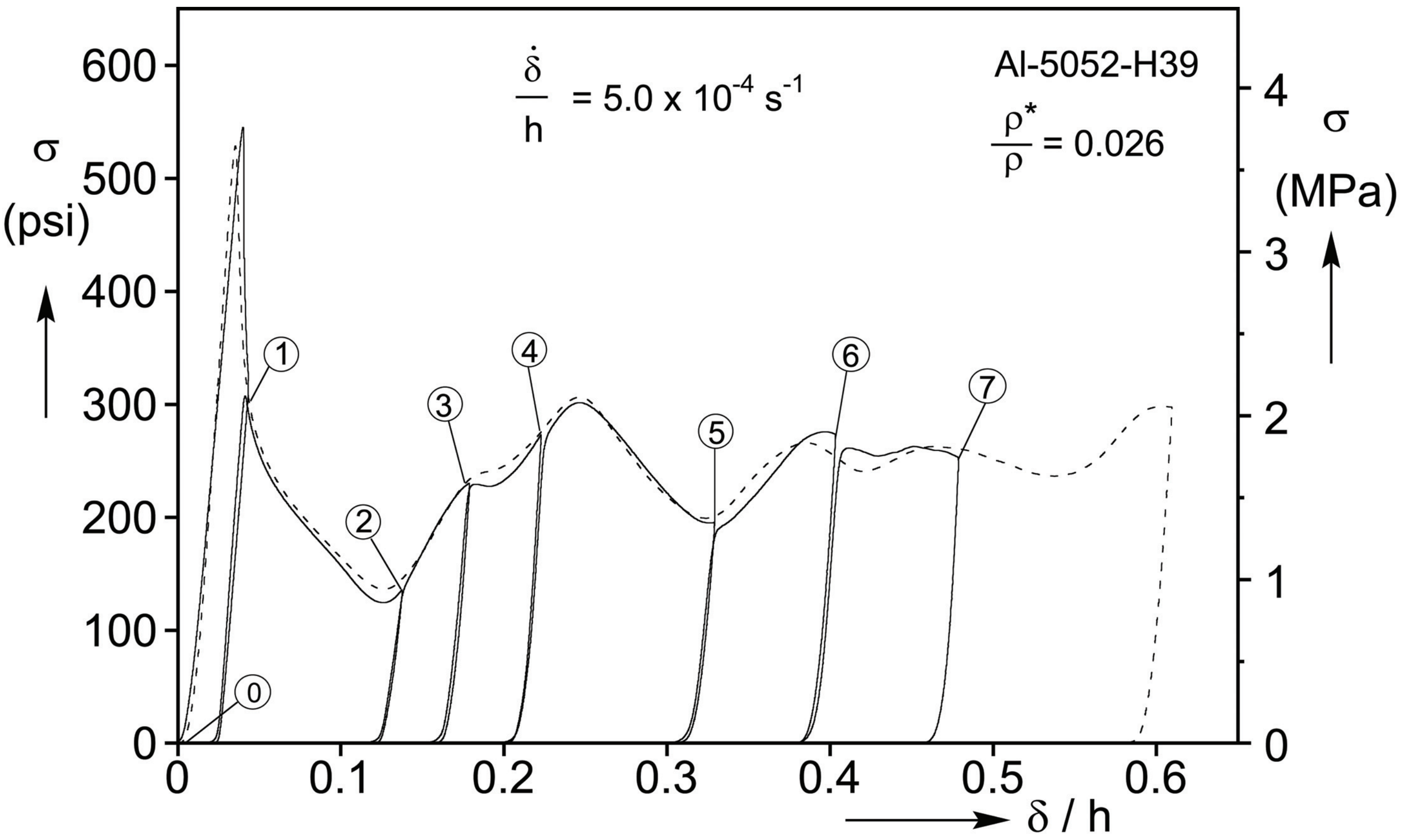

Figure 2.6a: Stress-shortening responses of a typical panel crushing experiment (dashed line) and a second one from an incremental compression test (solid line).

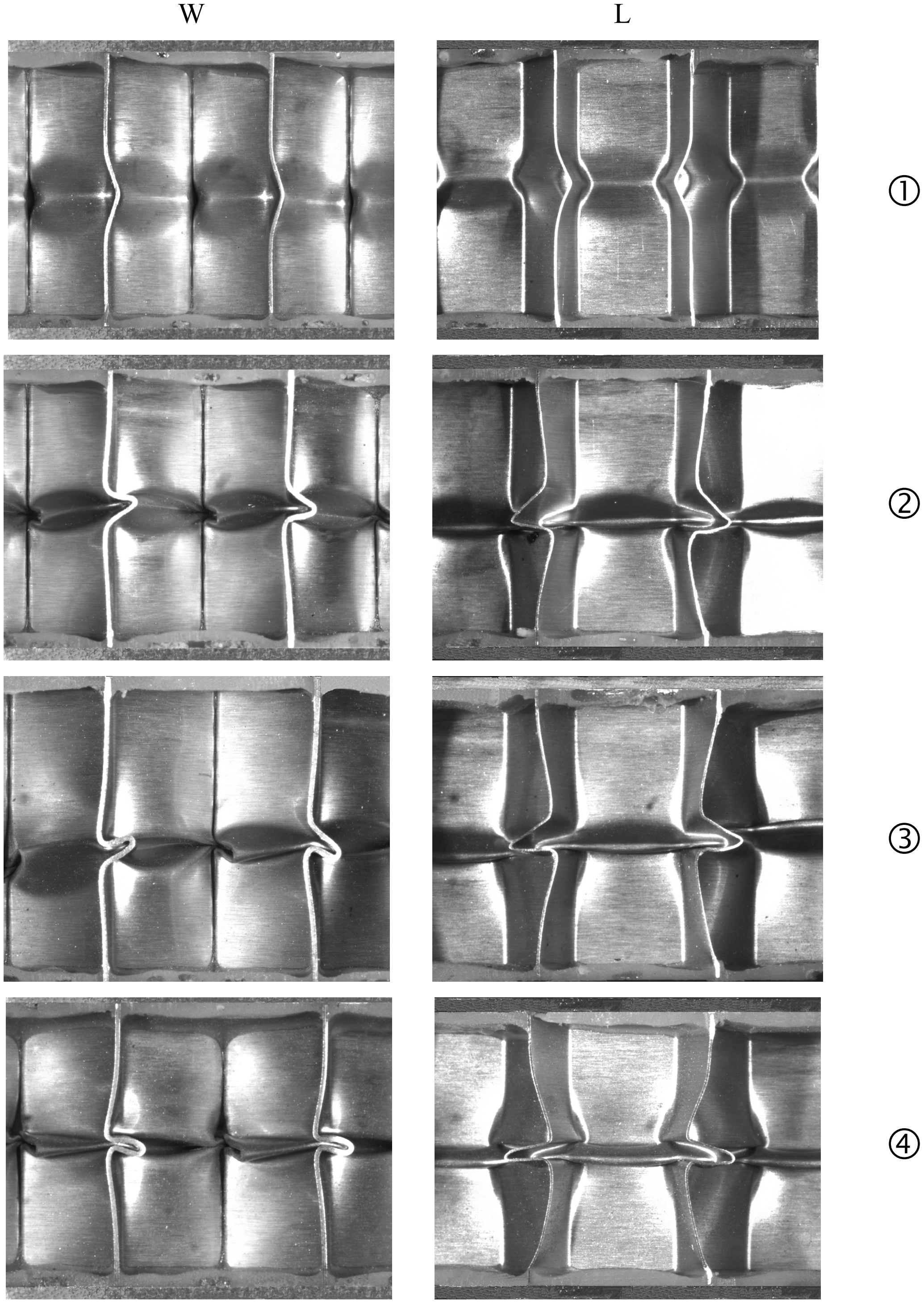

Figure 2.6b: Crushing configurations corresponding to numbers in Fig. 2.6a.

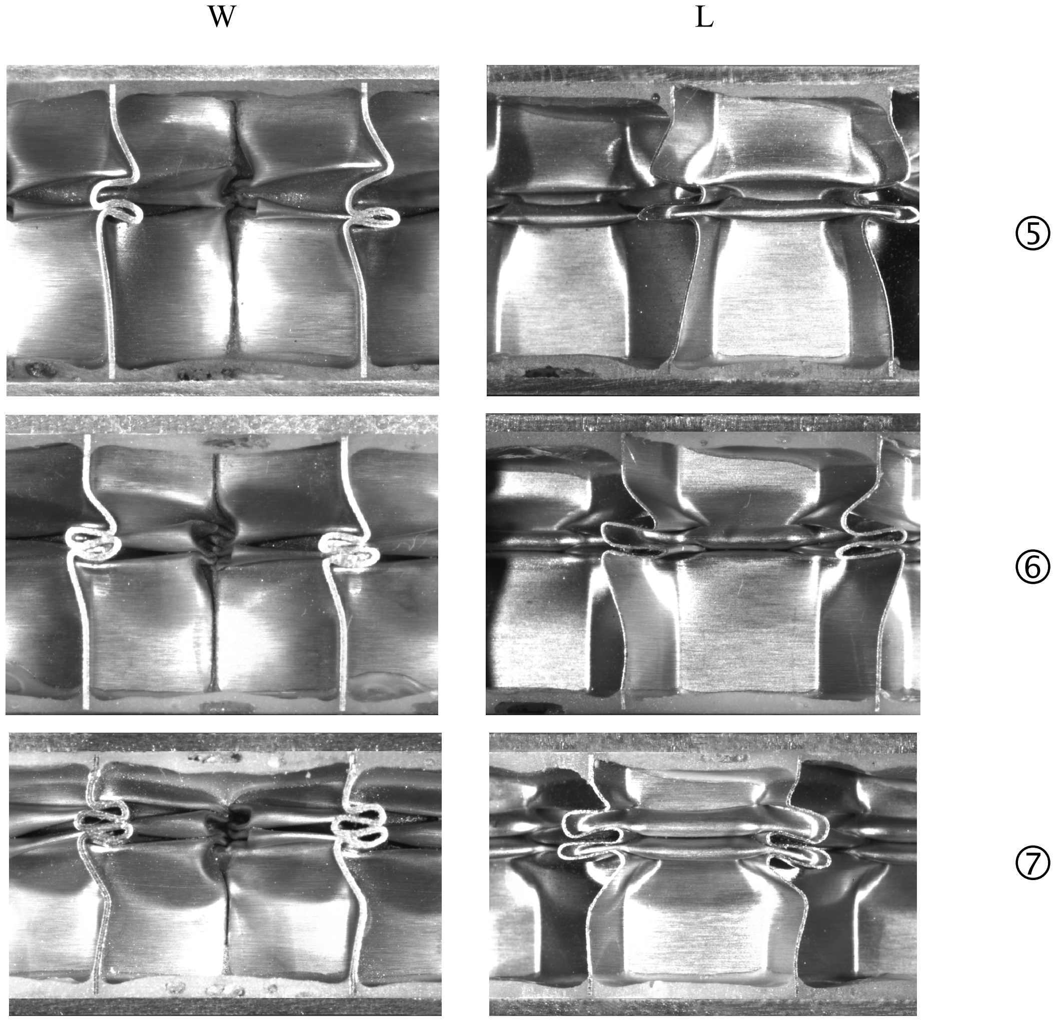

Figure 2.6c: Crushing configurations cont.

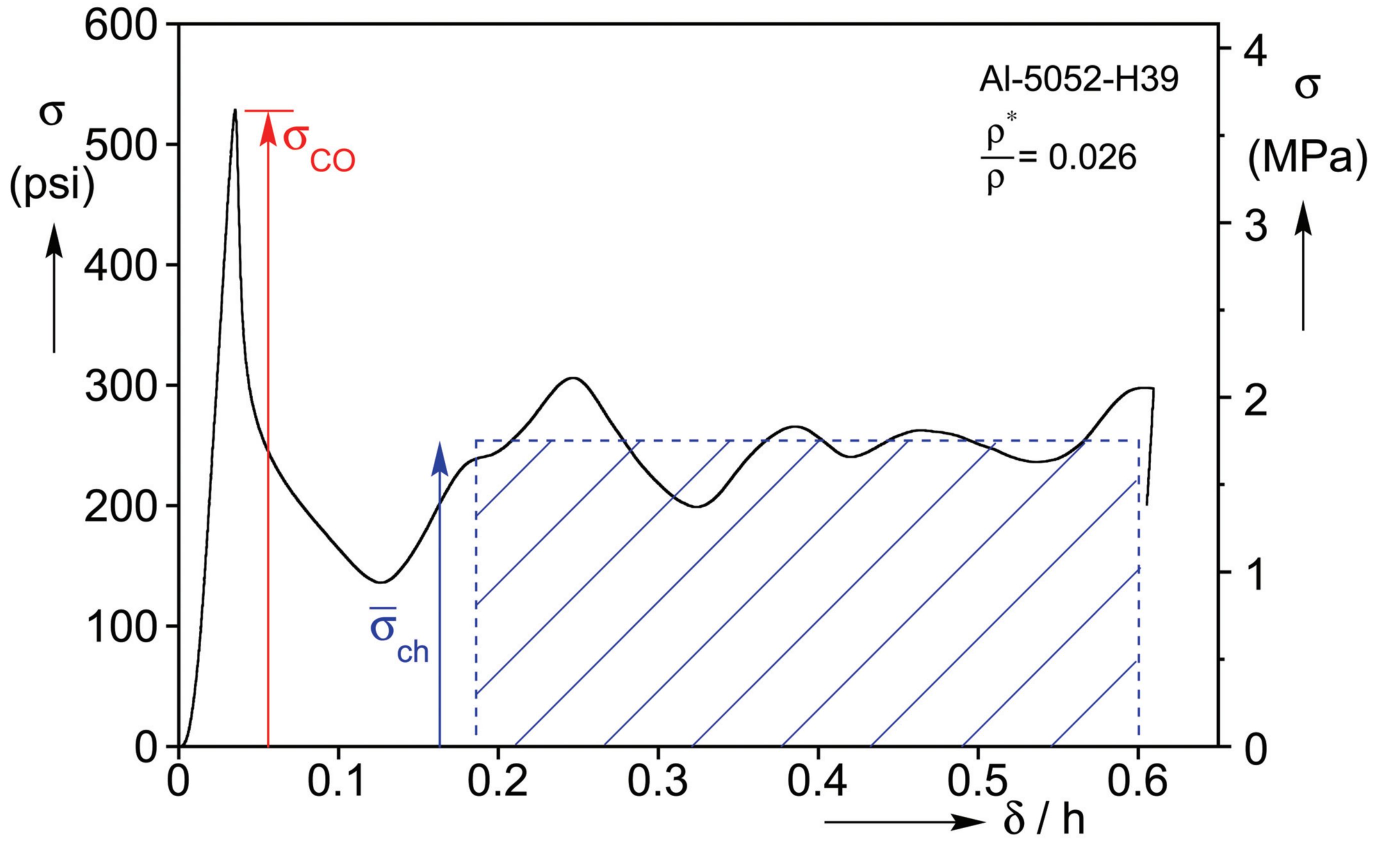

Figure 2.7: Definition of collapse and average crushing stresses on a typical stress-shortening response of a honeycomb panel.

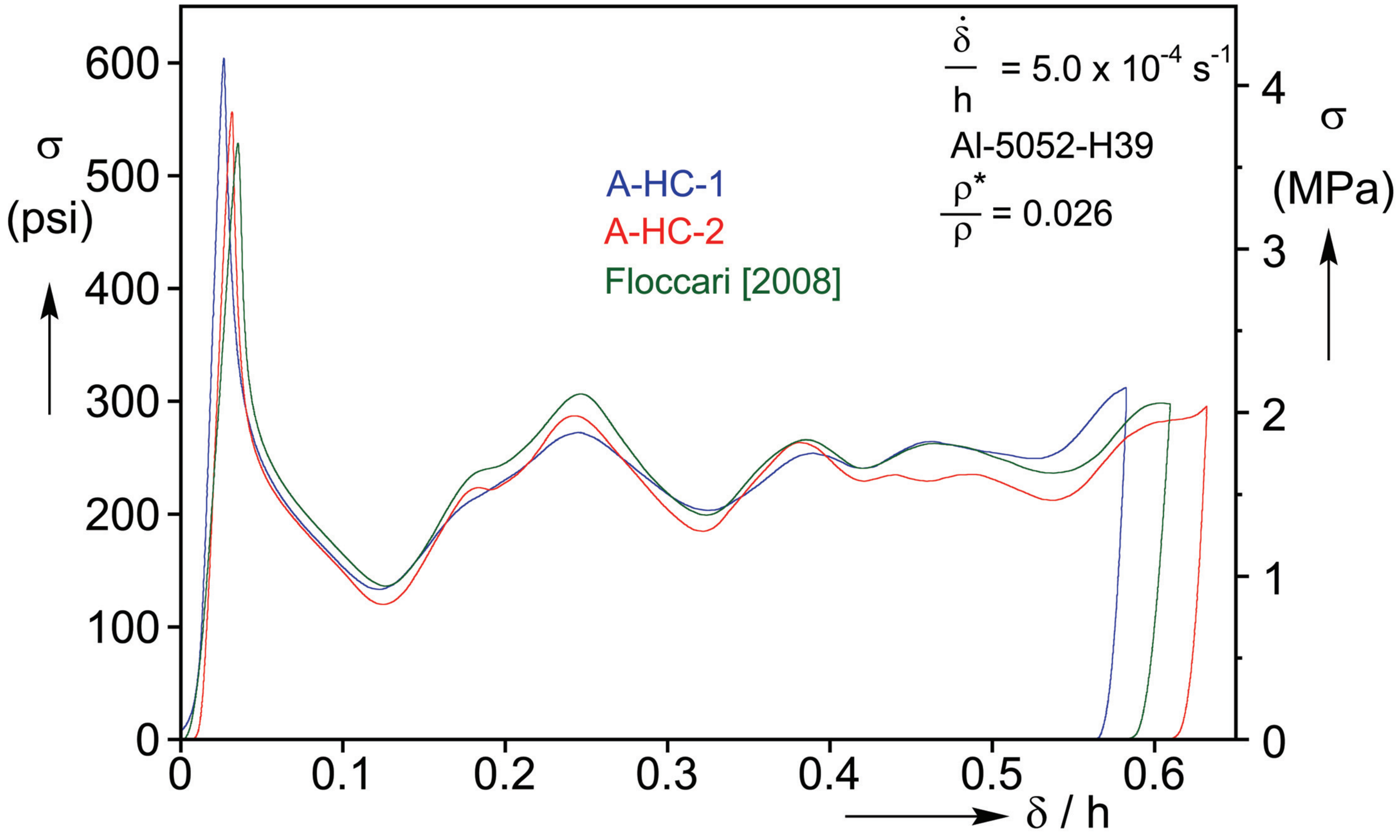

Figure 2.8a: Stress-shortening responses from three experiments on honeycomb panels unloaded at $\delta/h \approx 0.60$.

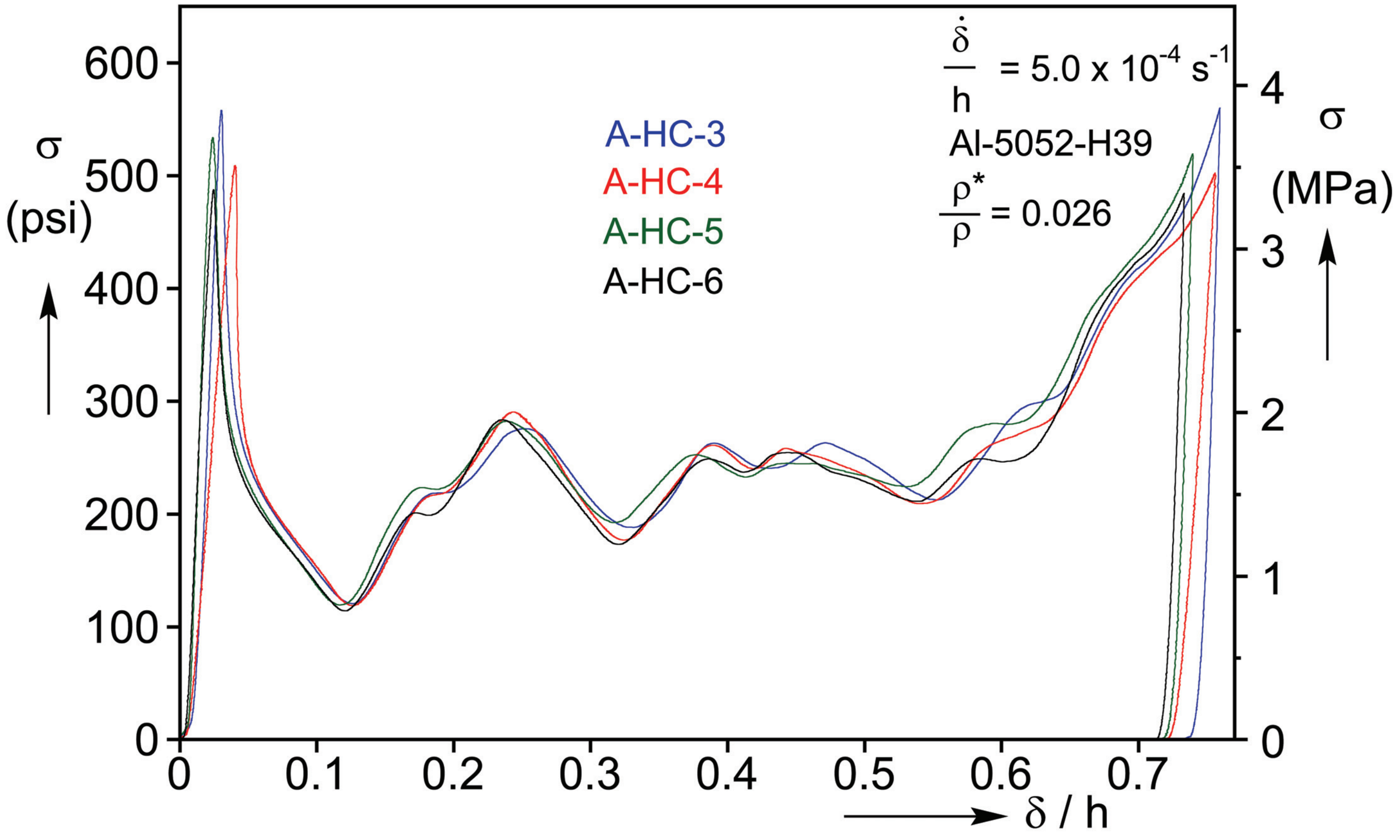

Figure 2.8b: Stress-shortening responses from four experiments on honeycomb panels unloaded at $\delta/h \approx 0.75$.

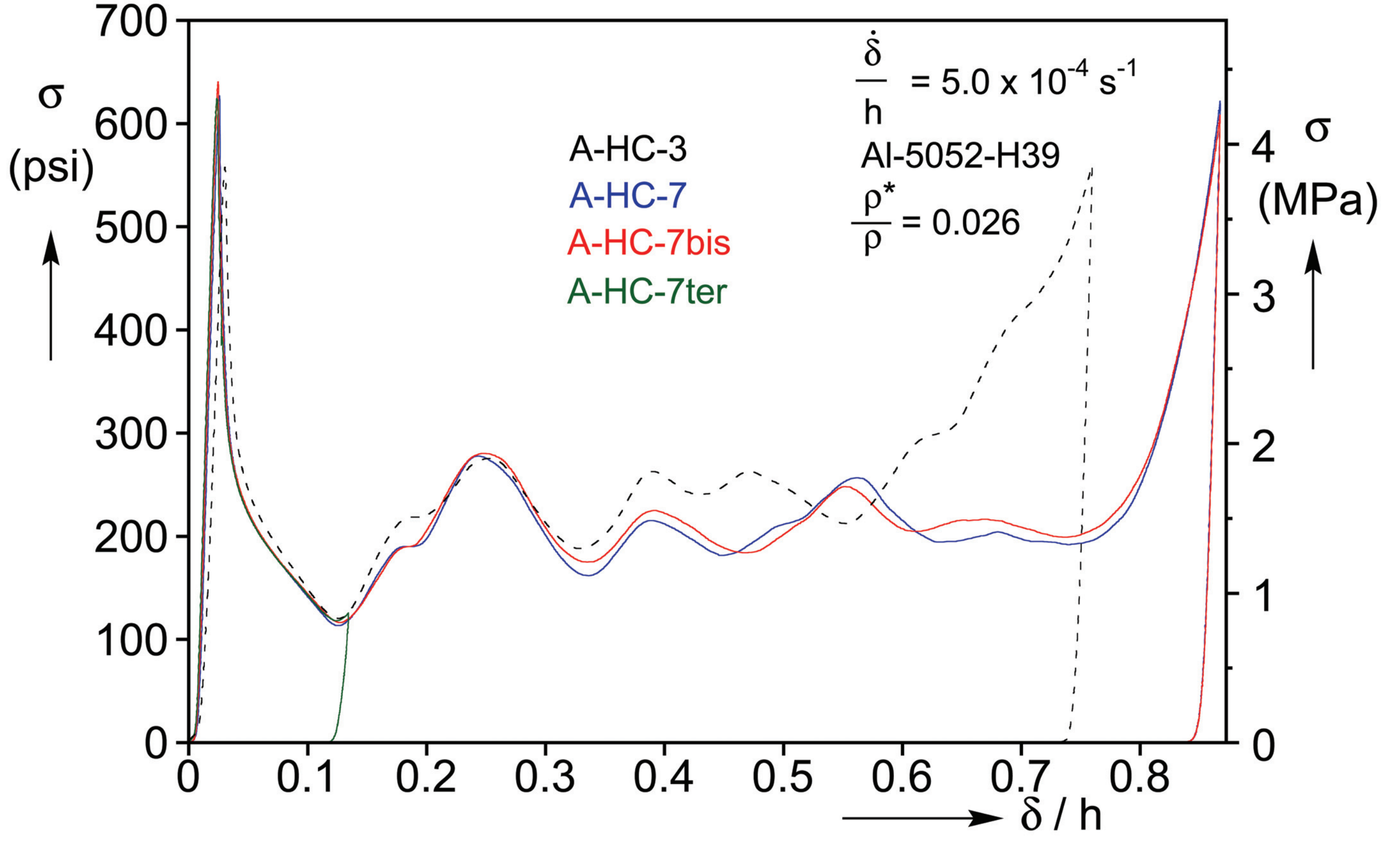

Figure 2.9: Stress-shortening responses from three crushing experiments on honeycombs without faceplates and a case with faceplates.

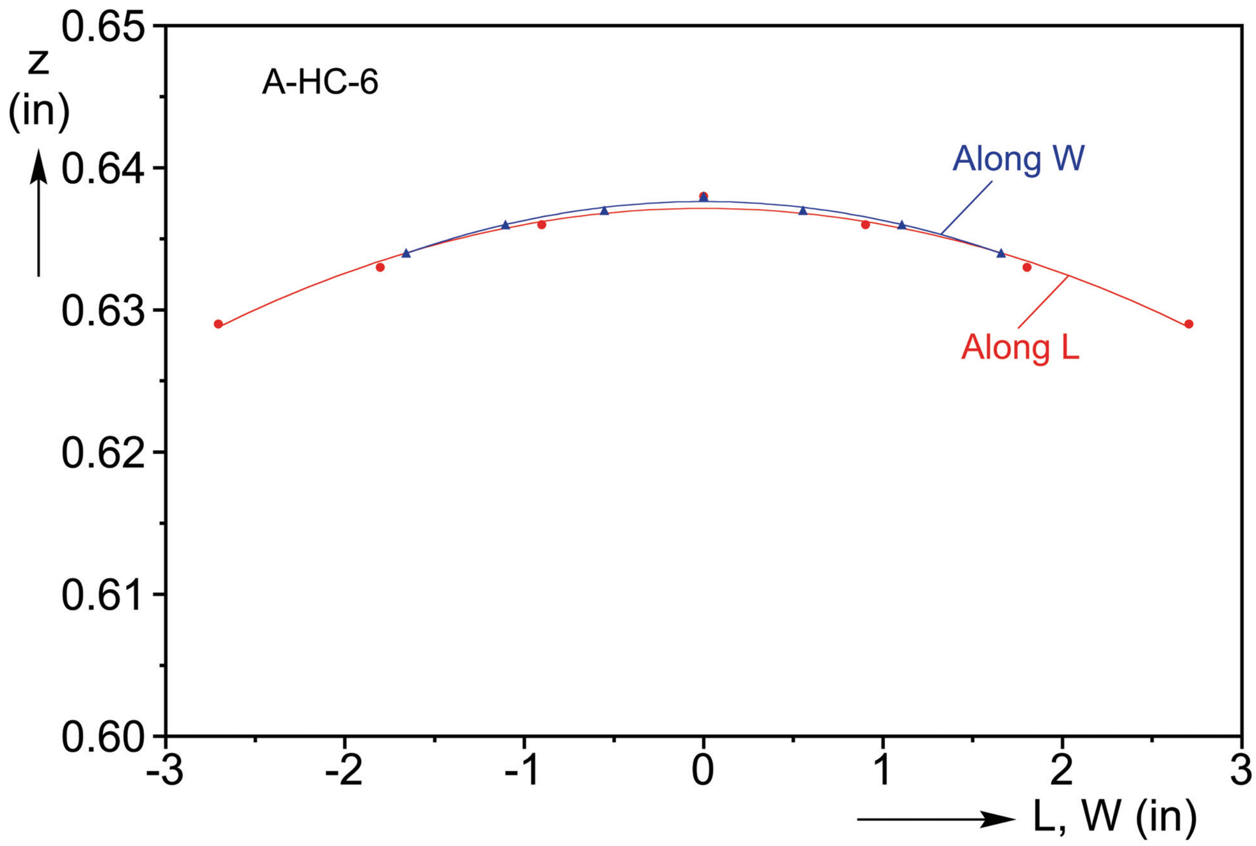

Figure 2.10: Bending profile of the top surface of panel specimen A-HC-6 along center lines.

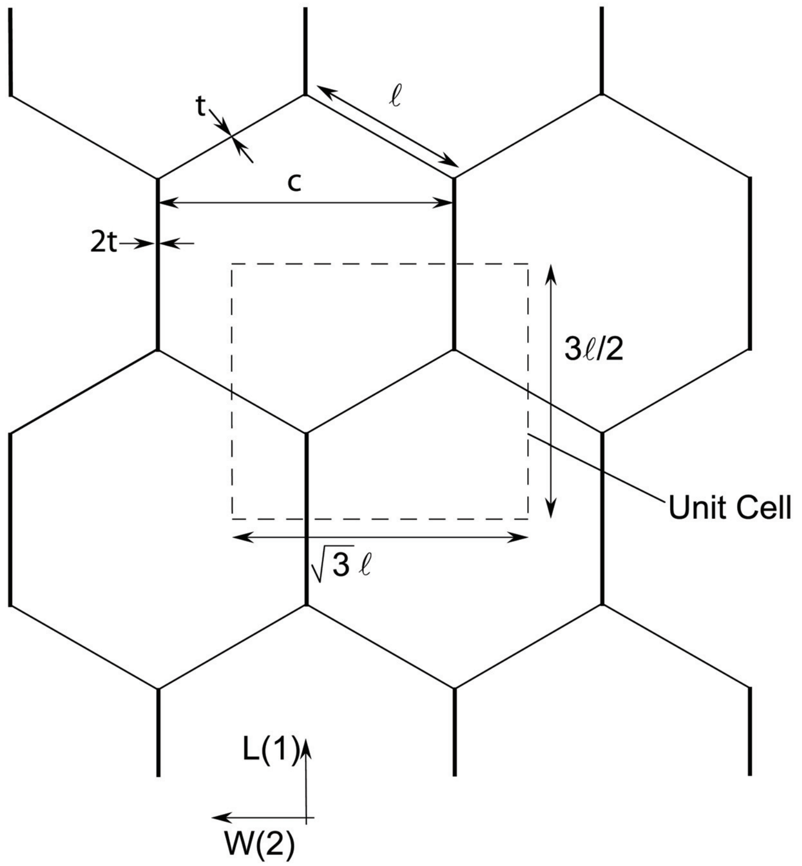

Figure 3.1: Idealized hexagonal cell geometry used in the FE analyses.

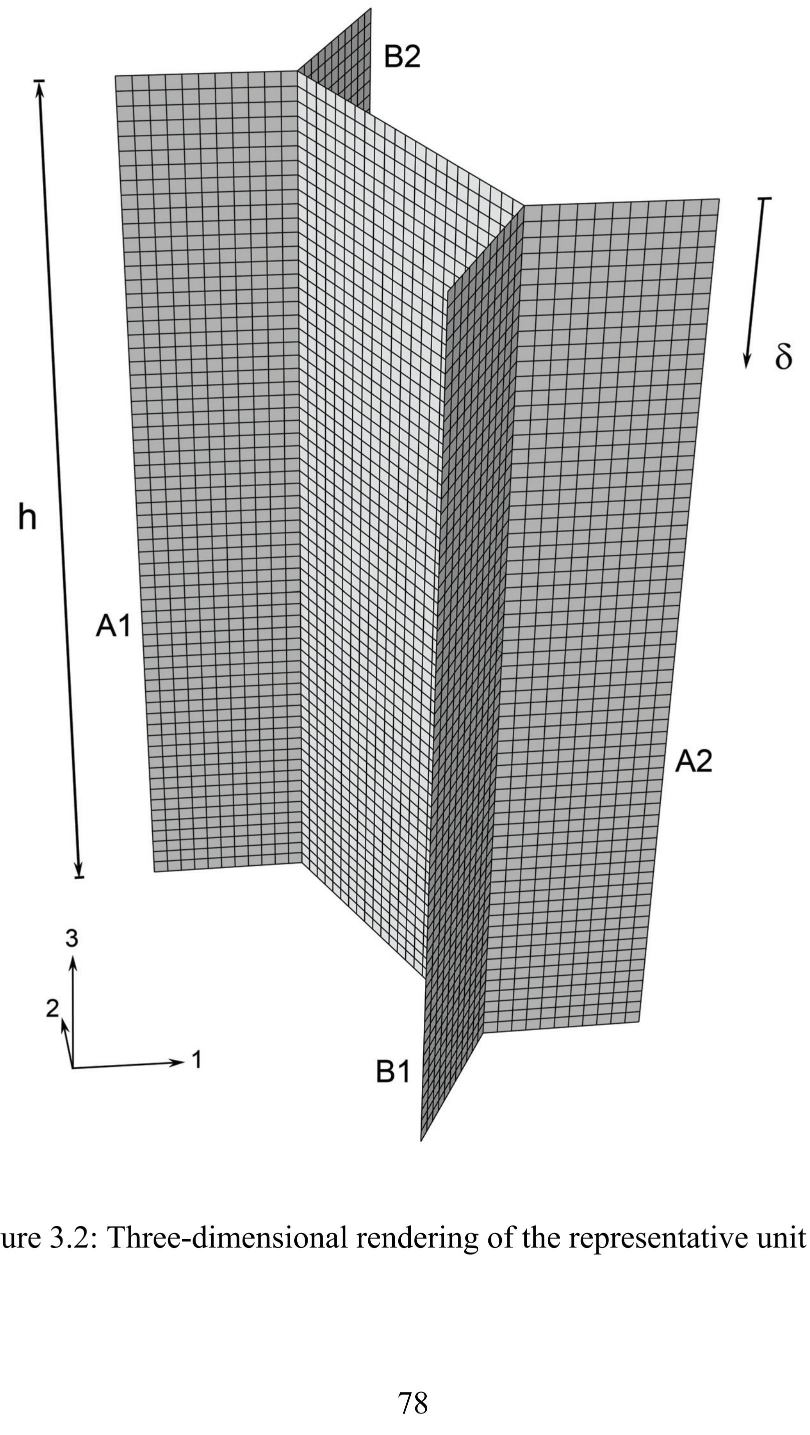

Figure 3.2: Three-dimensional rendering of the representative unit cell.

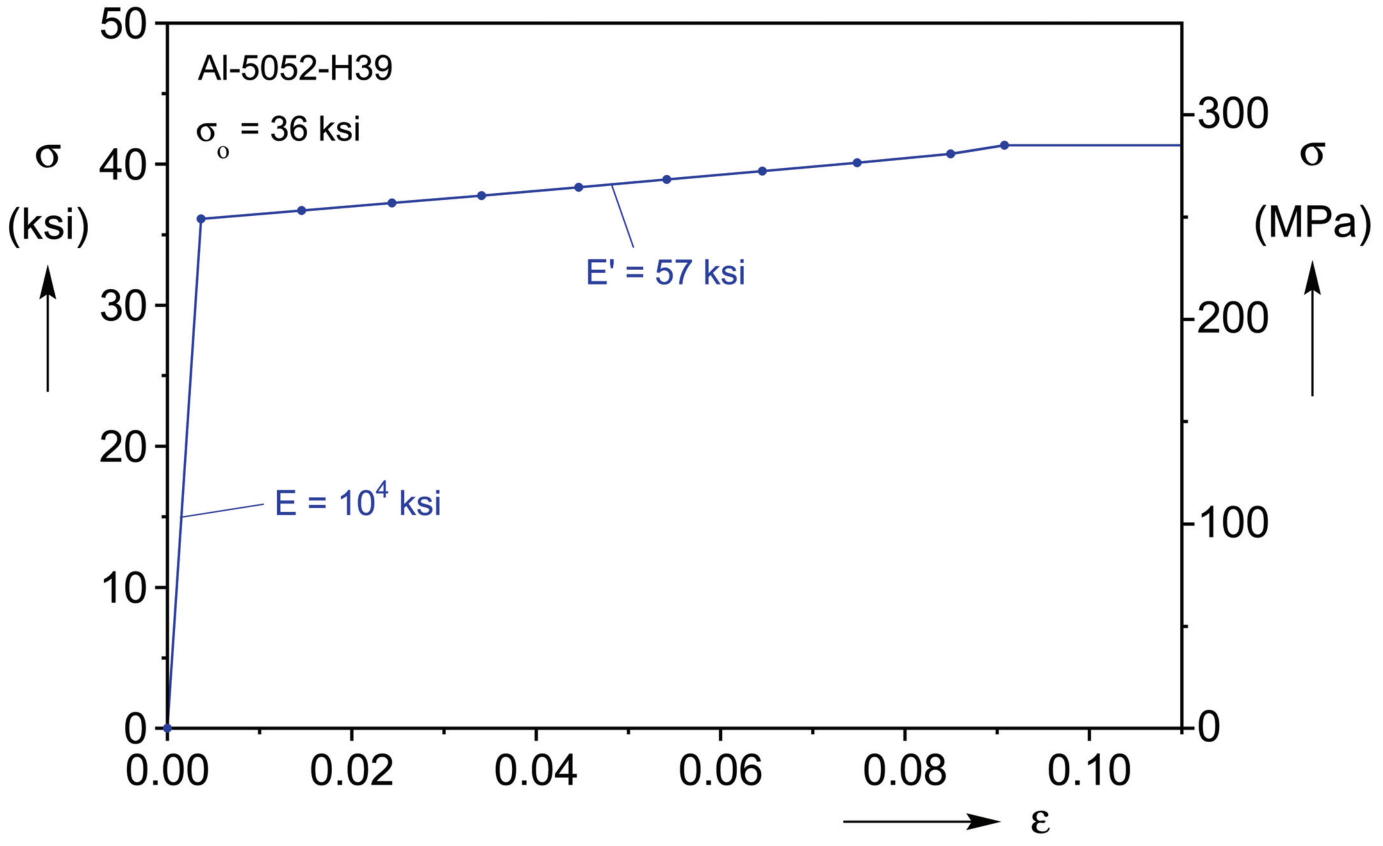

Figure 3.3: Trilinear stress-strain response of the honeycomb Al alloy used in the calculations.

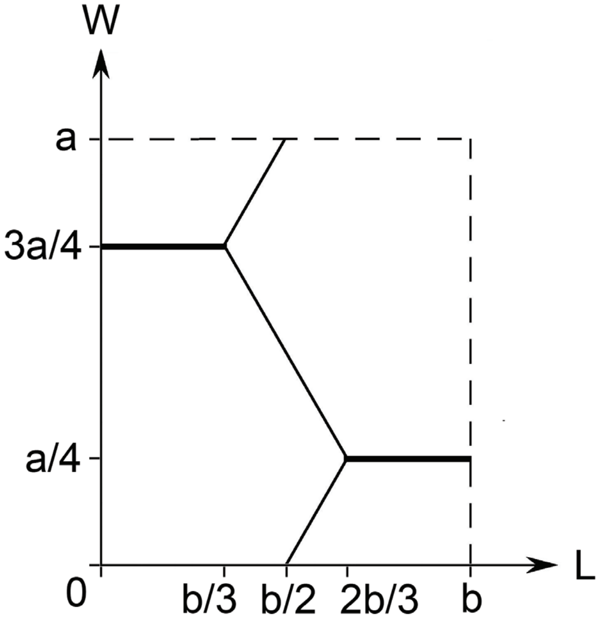

Figure 3.4: Plan view of the unit cell with parameters used in the Matlab code to generate the FE geometry and mesh.

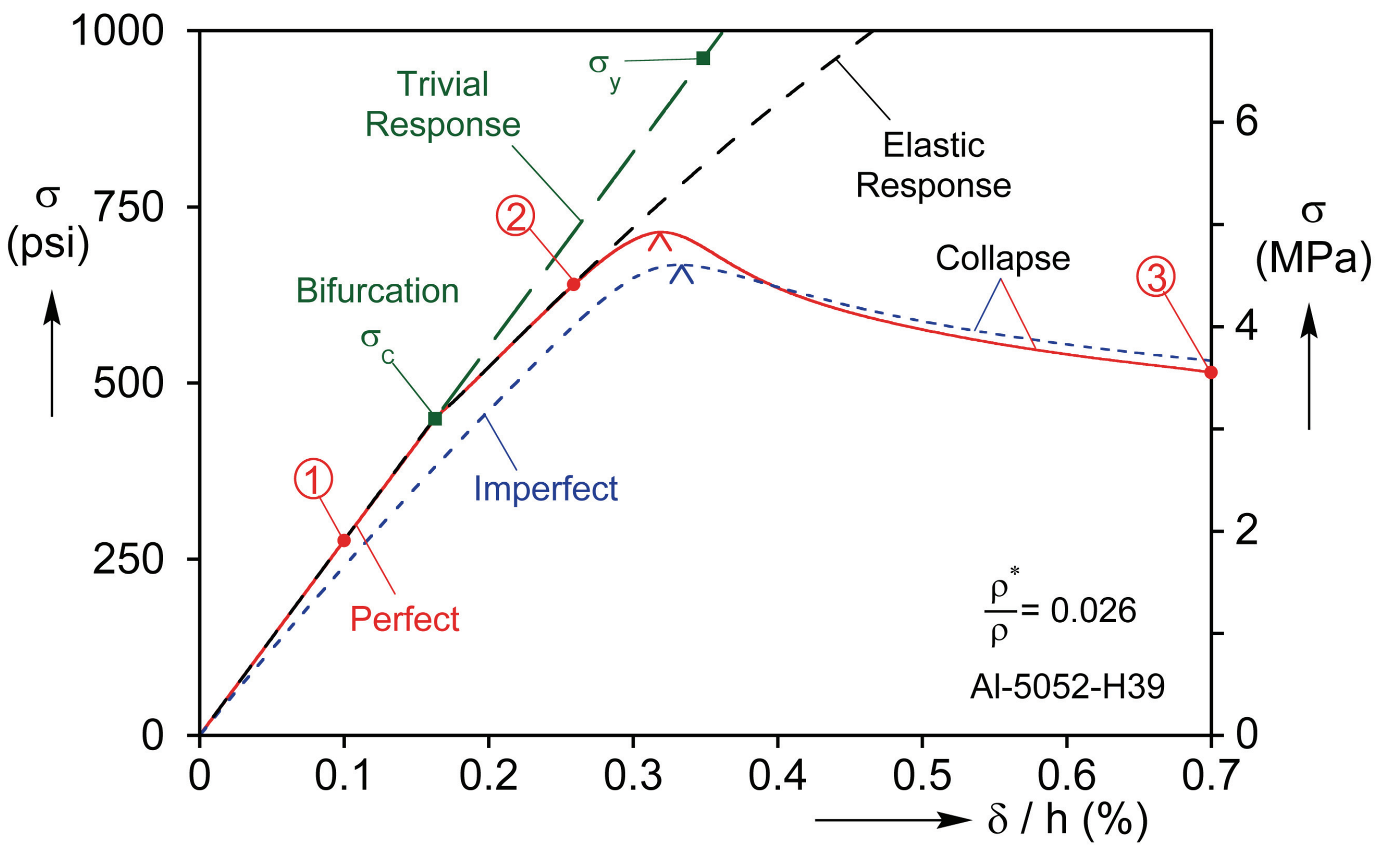

Figure 3.5: Initial stress-shortening responses for perfect and imperfect unit cells.

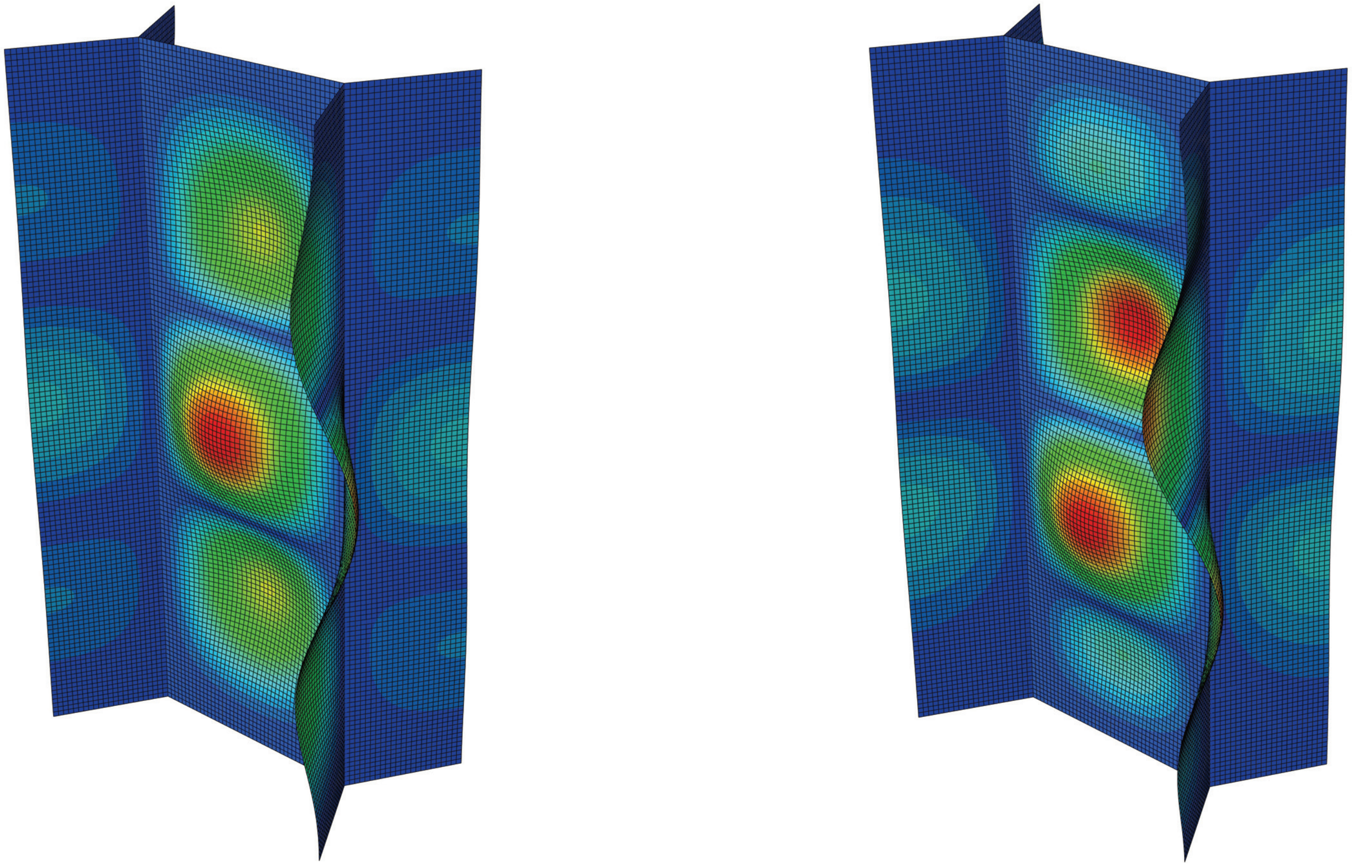

(a) (b)

Figure 3.6: (a) First buckling mode and (b) second buckling mode of unit cell.

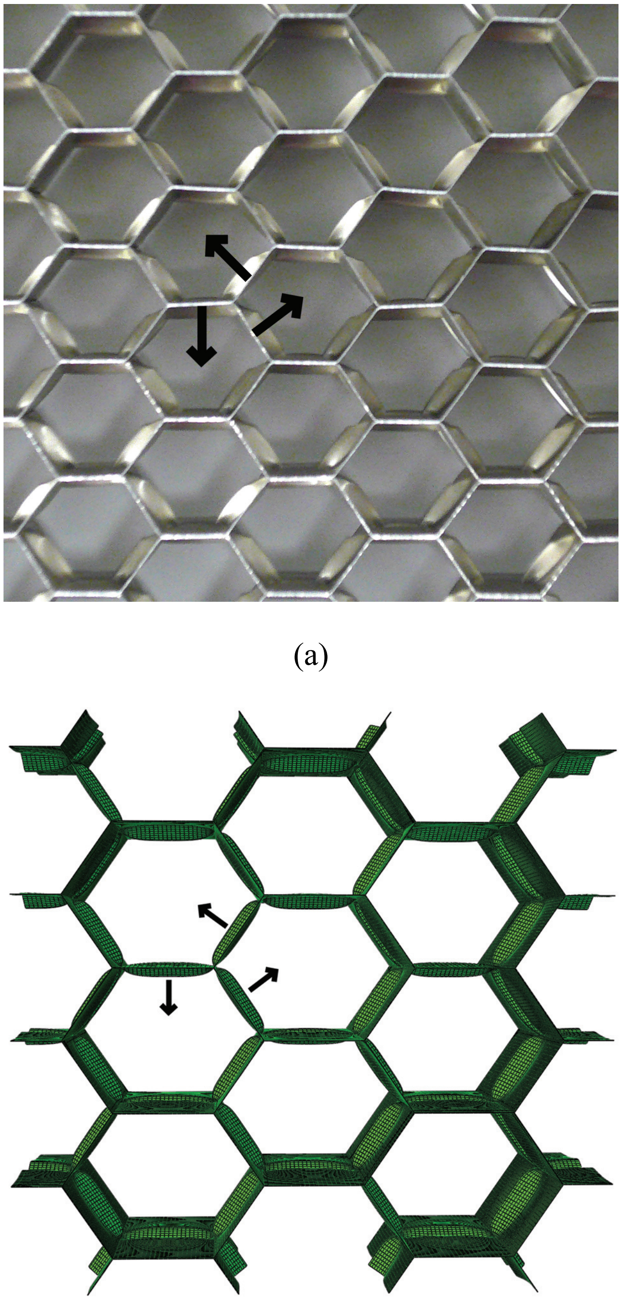

(a)

(b)

Figure 3.7: Images that illustrate the compatibility of the buckling mode between neighboring cells: (a) experiment and (b) calculations.

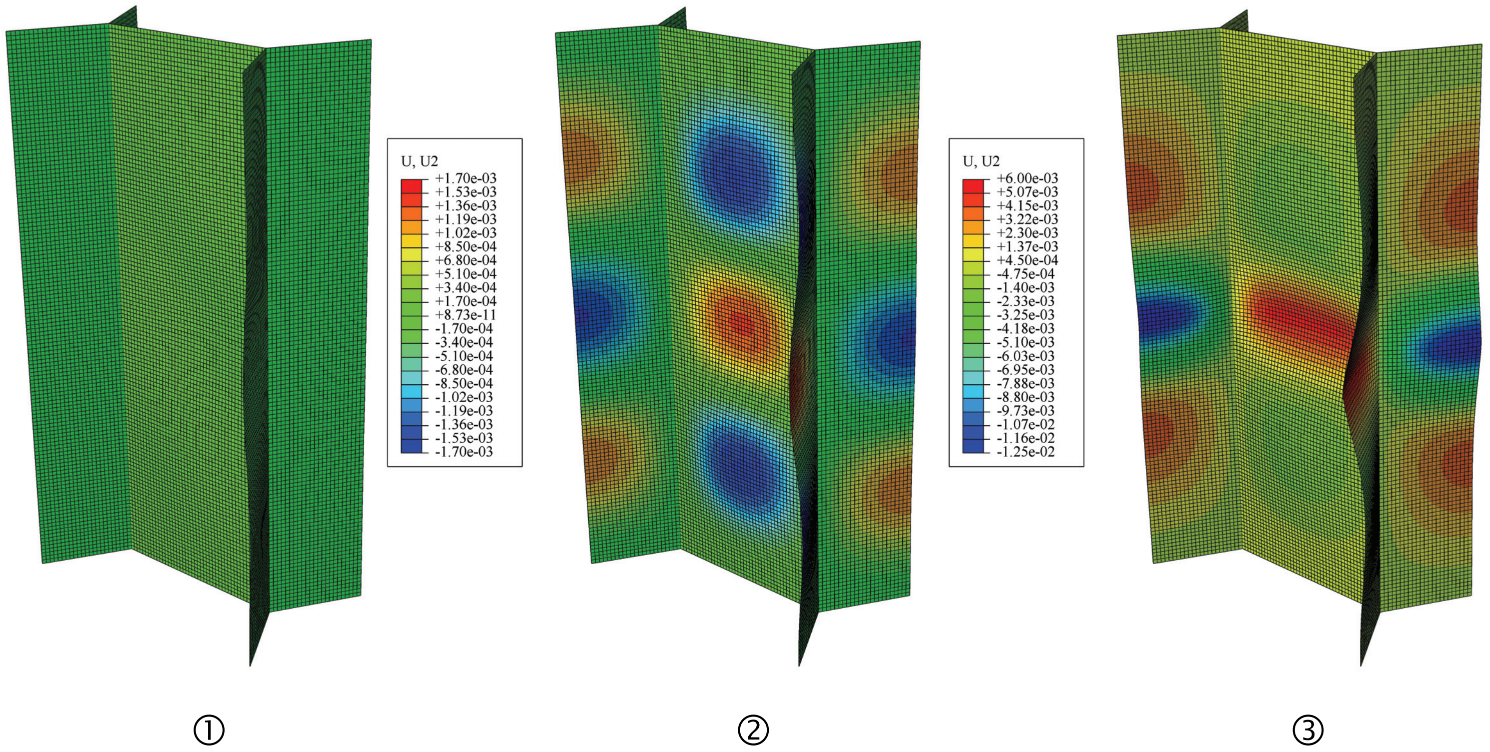

Figure 3.8: Deformed configurations corresponding to numbered points on the response in Fig. 3.5.

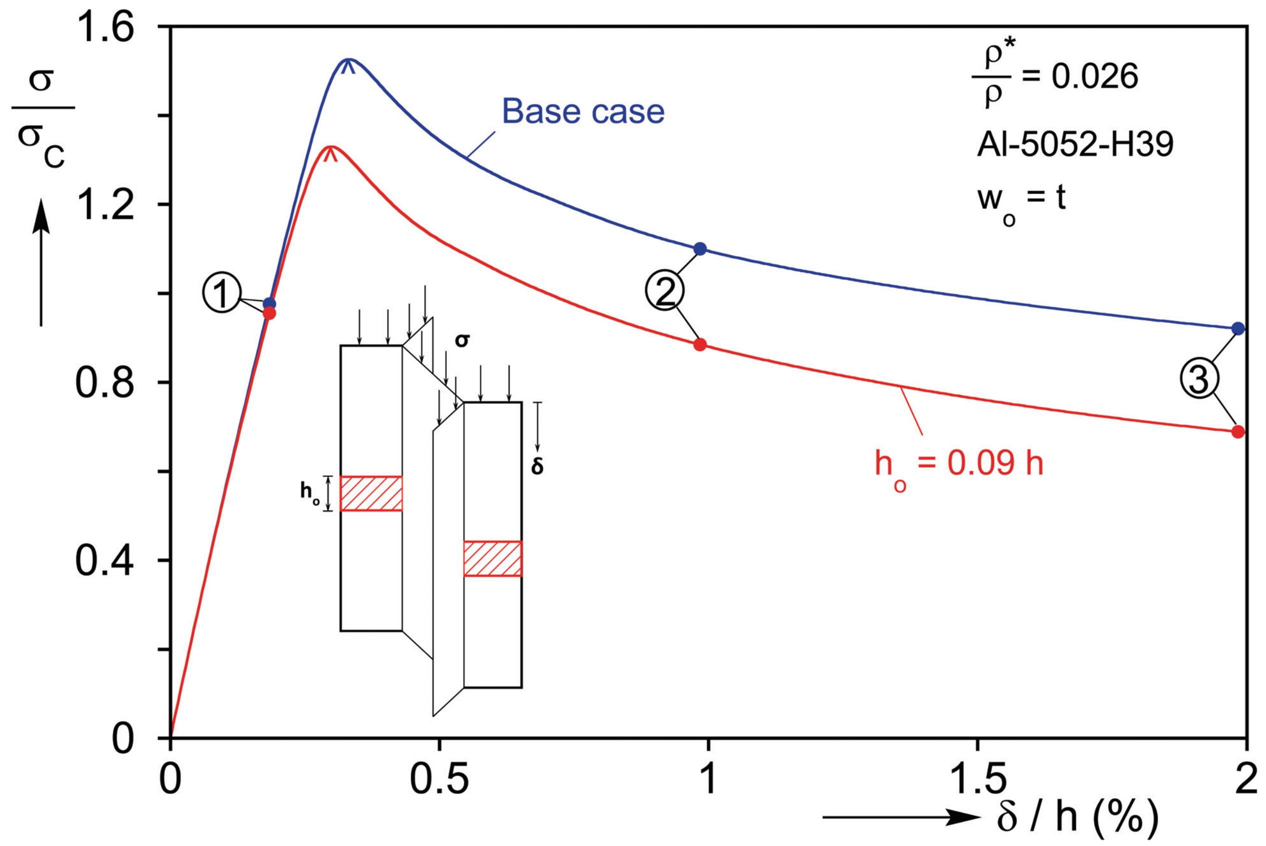

Figure 3.9a: Comparison of stress-shortening responses of the unit cell with and without an initial debond of height h_0.

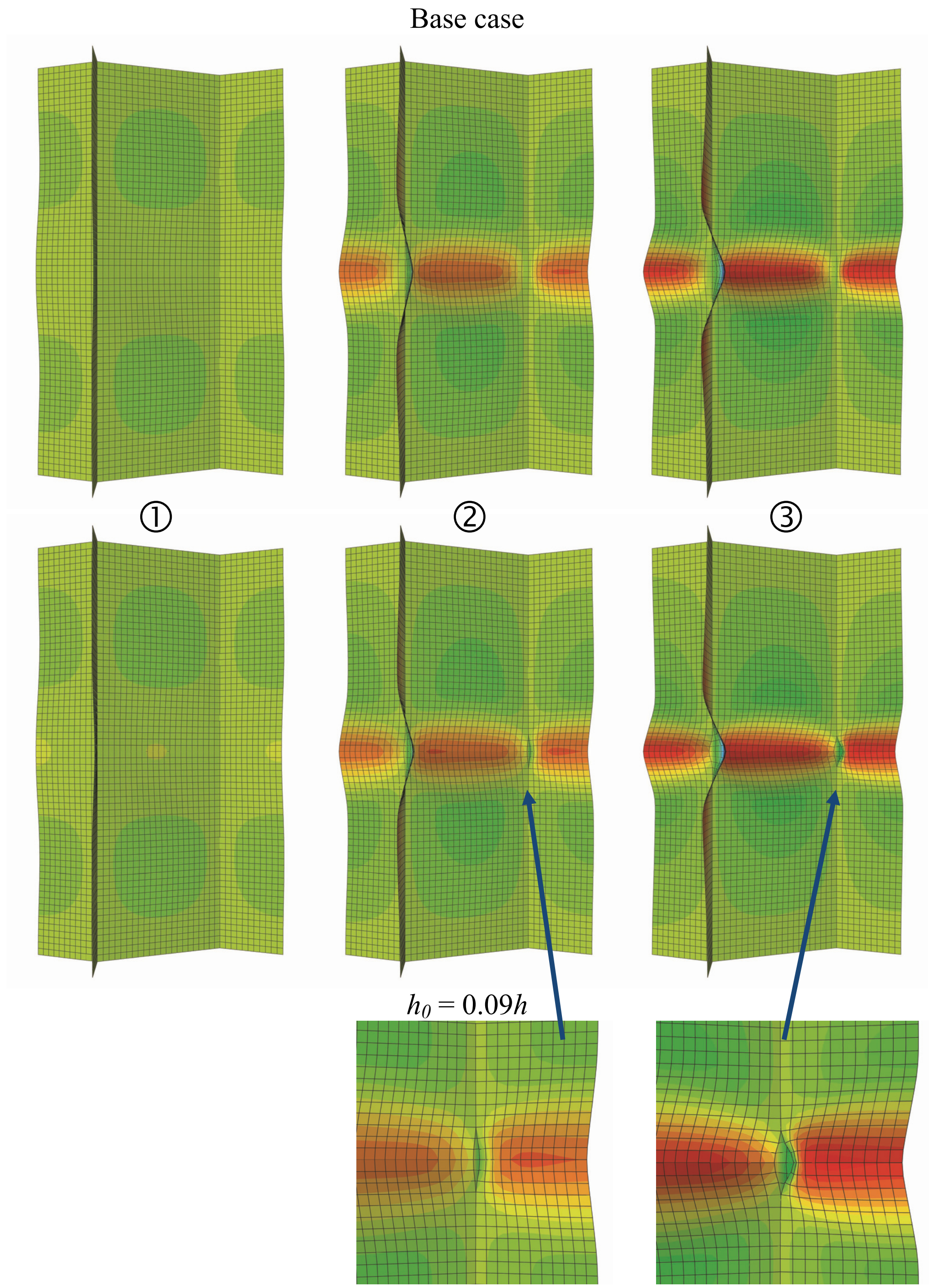
Base case

Figure 3.9b: Deformed configurations corresponding to numbered points on the responses in Fig. 3.9a.

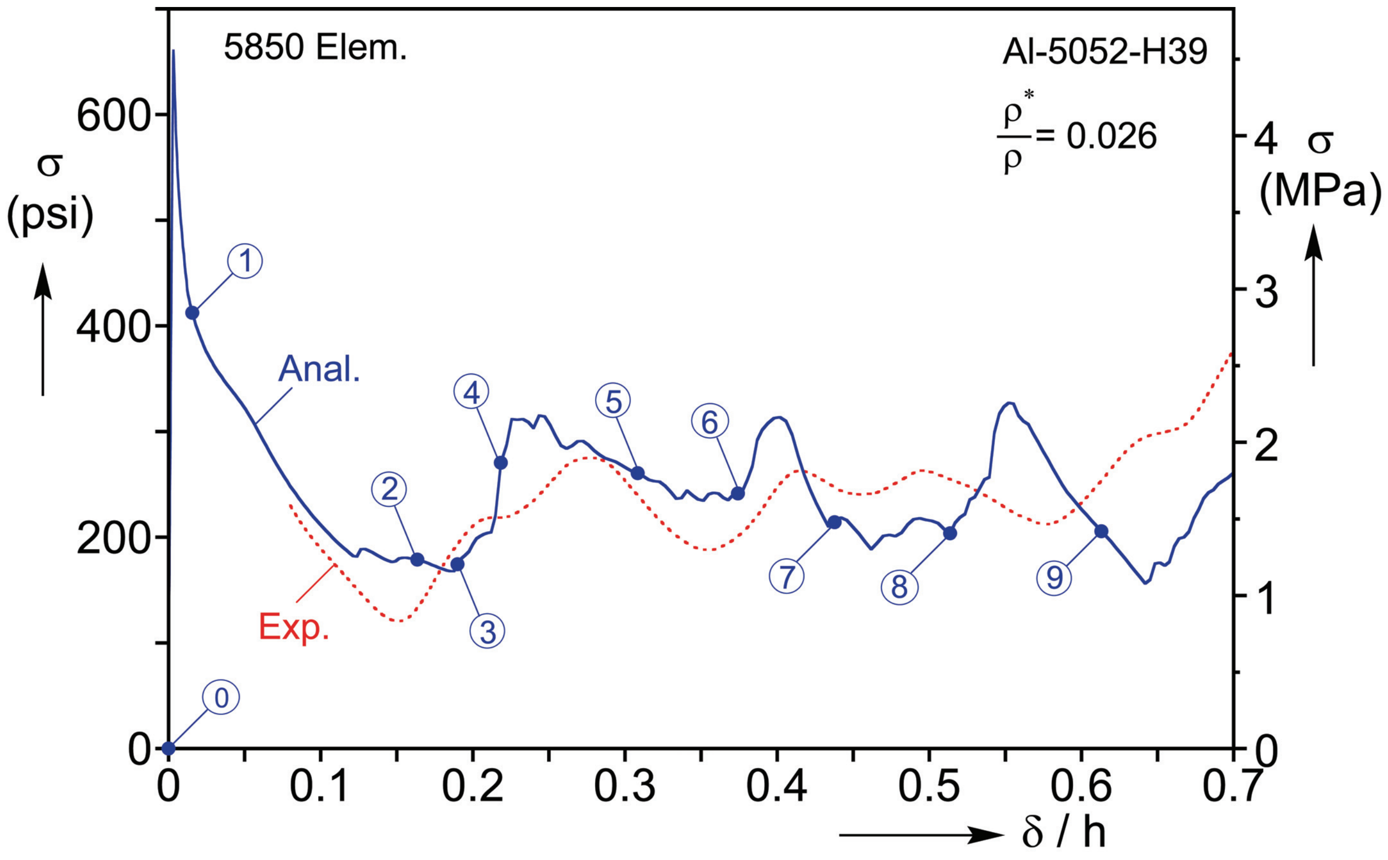

Figure 3.10: Comparison of calculated and measured crushing responses (unit cell with 5850 elements).

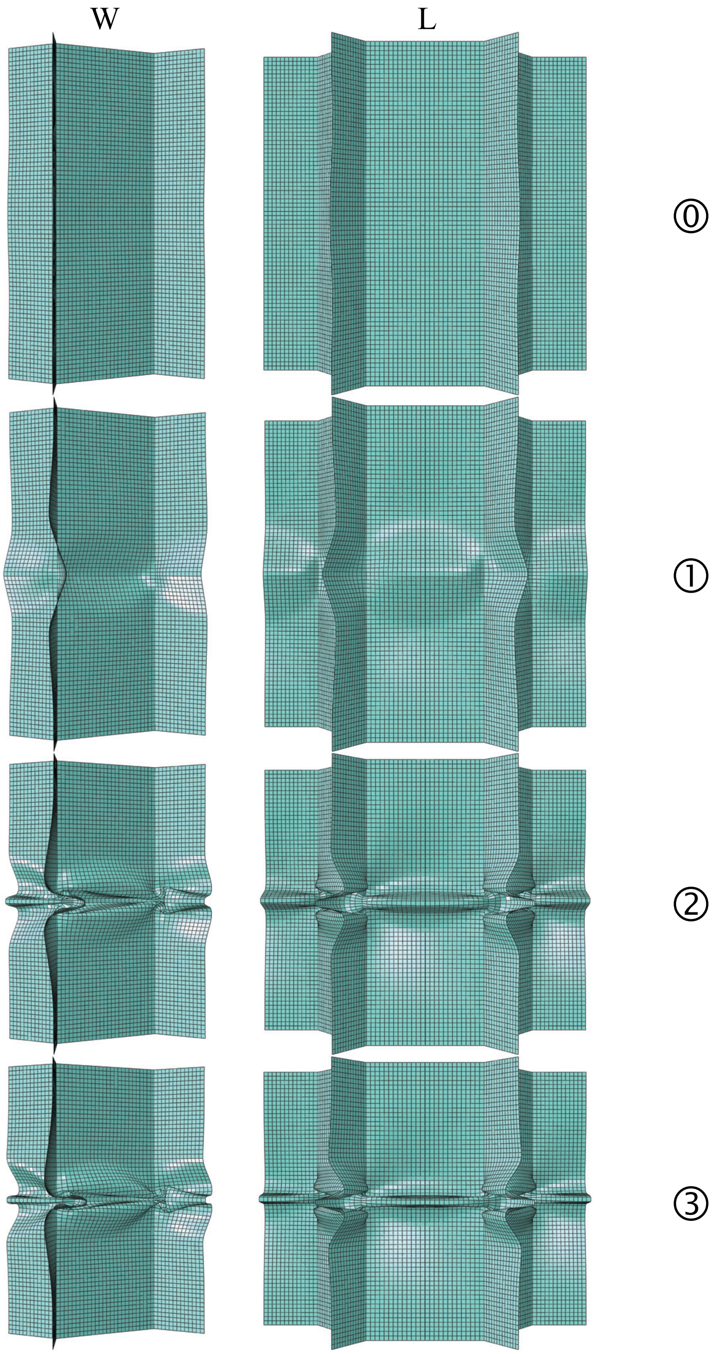

Figure 3.11a: Deformed configurations of the unit cell at different stages of crushing corresponding to numbered bullets on the calculated response in Fig. 3.10 (views of W and L planes: L views have been doubled for better visualization).

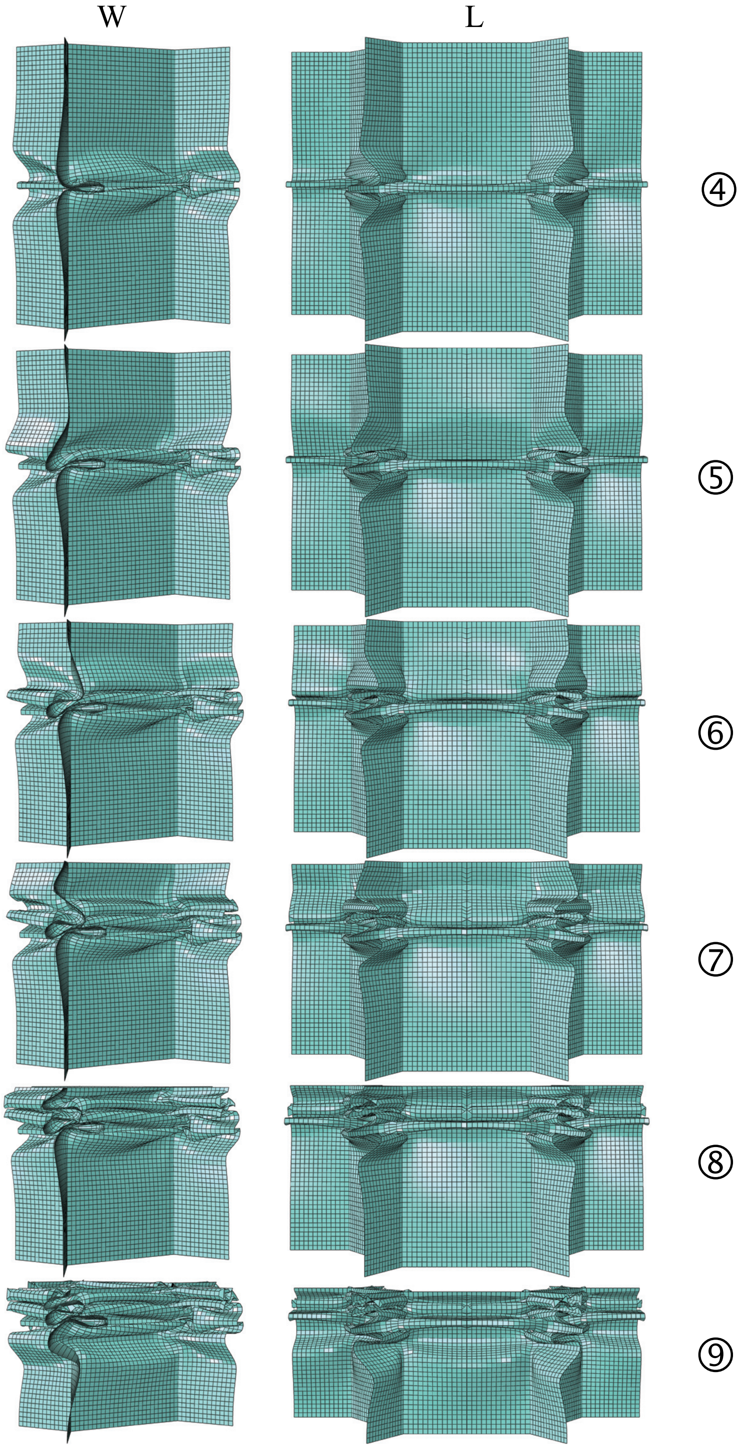

Figure 3.11b: cont.

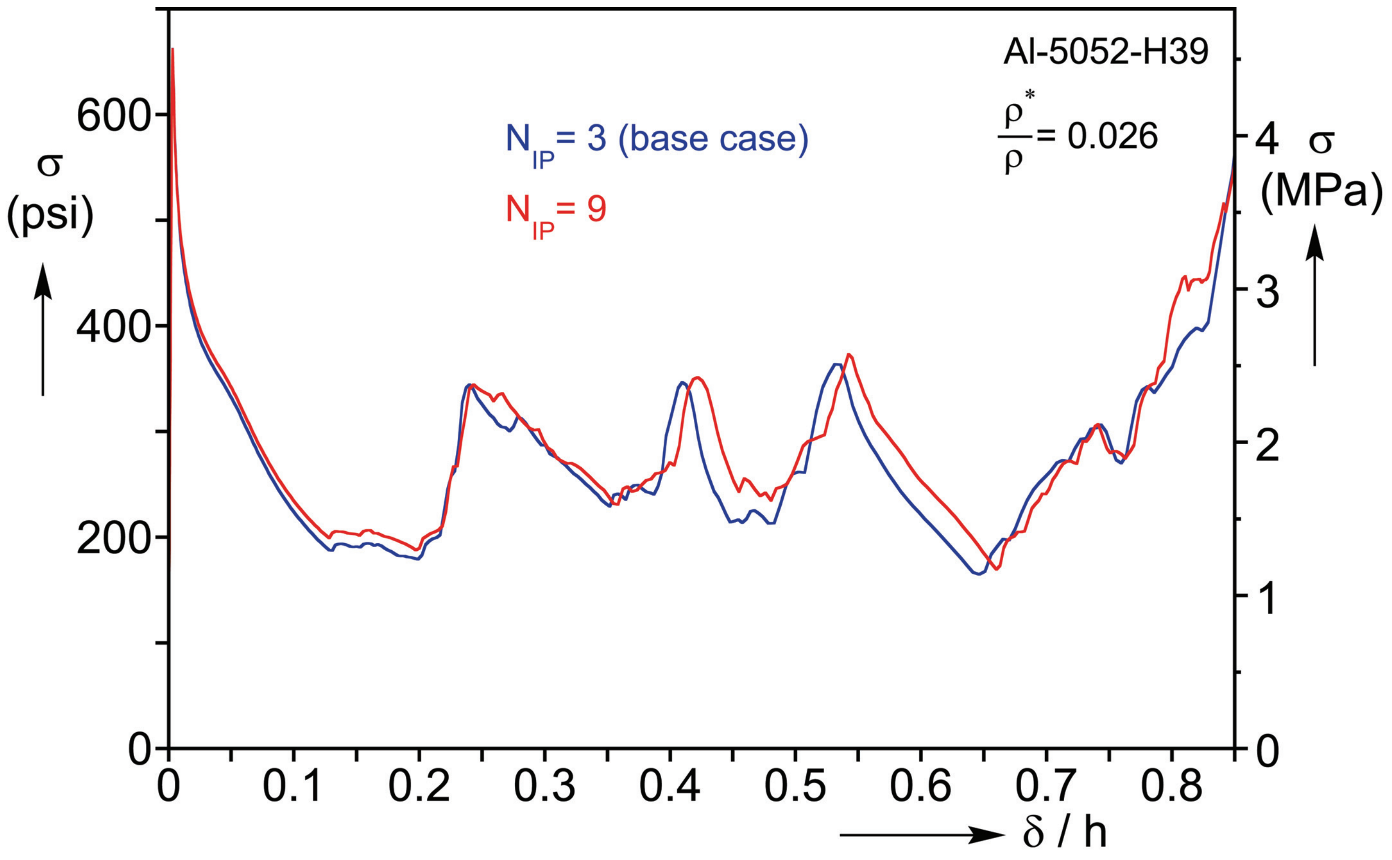

Figure 4.1: Calculated crushing responses vs. number of through thickness Gaussian integration points.

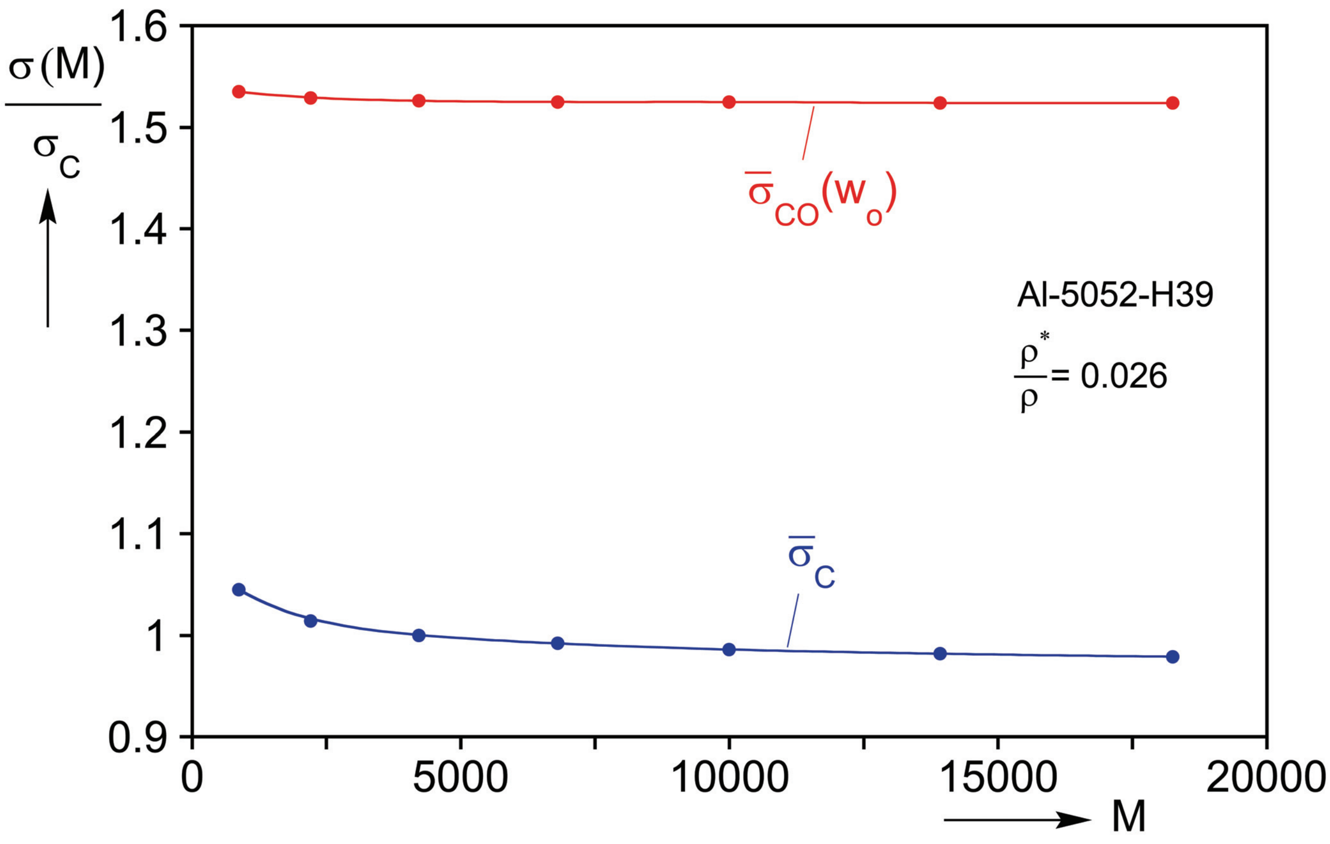

Figure 4.2: Calculated buckling and collapse stresses vs. number of elements used in the unit cell.

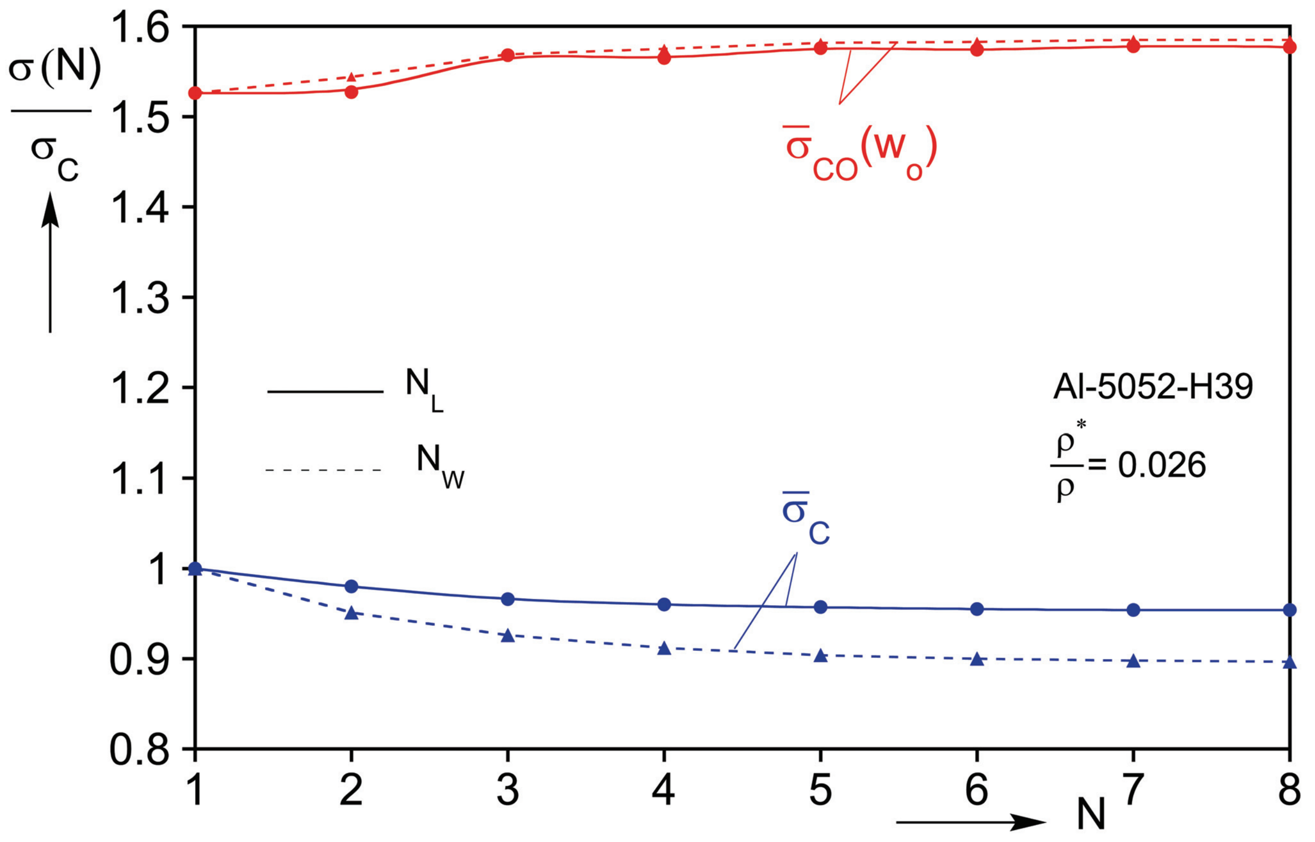

Figure 4.3: Calculated buckling and collapse stresses vs. number of cells in periodic rows along L and W directions.

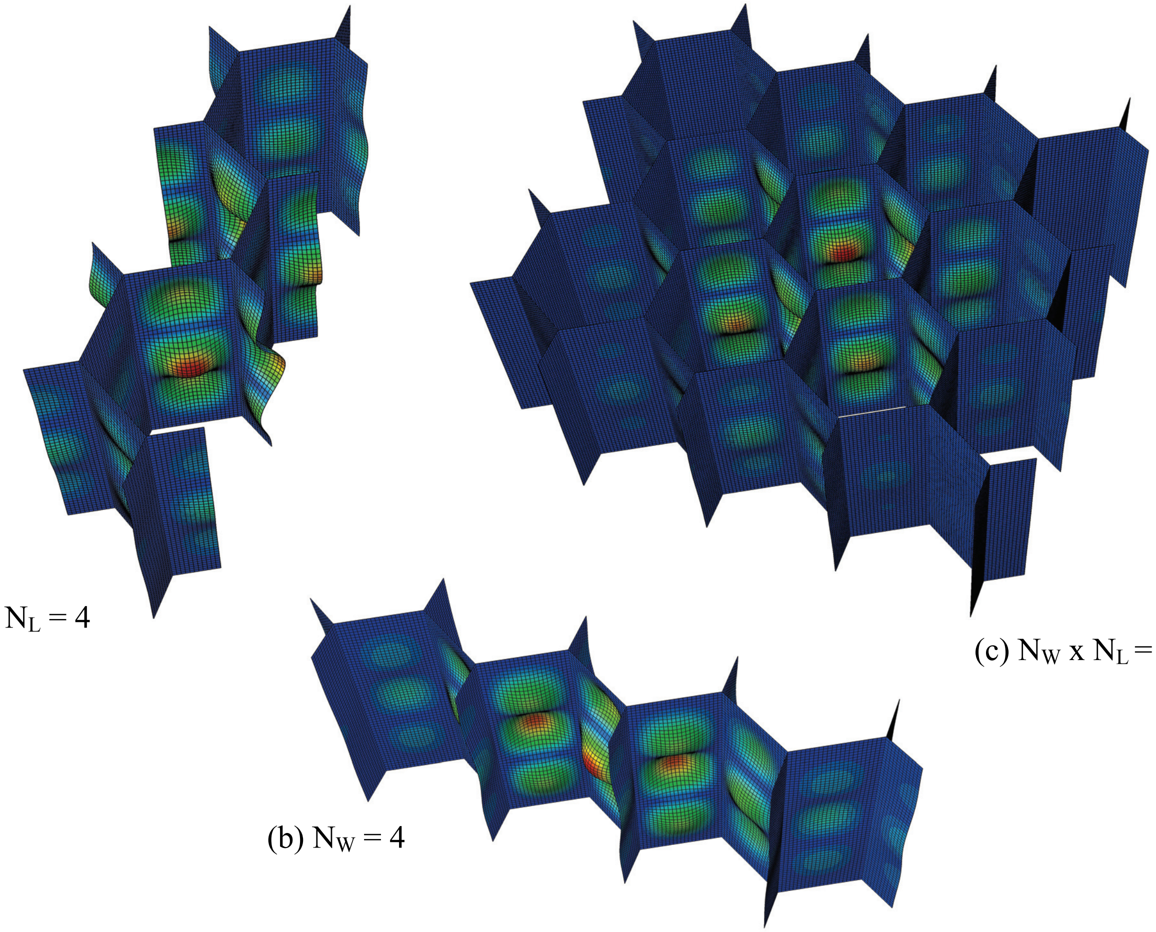

(a) $N_L = 4$

(b) $N_W = 4$

(c) $N_W \times N_L = 16$

Figure 4.4: First buckling modes for domains with (a) 4 cells along L, (b) 4 cells along W, and (c) 4×4 cells.

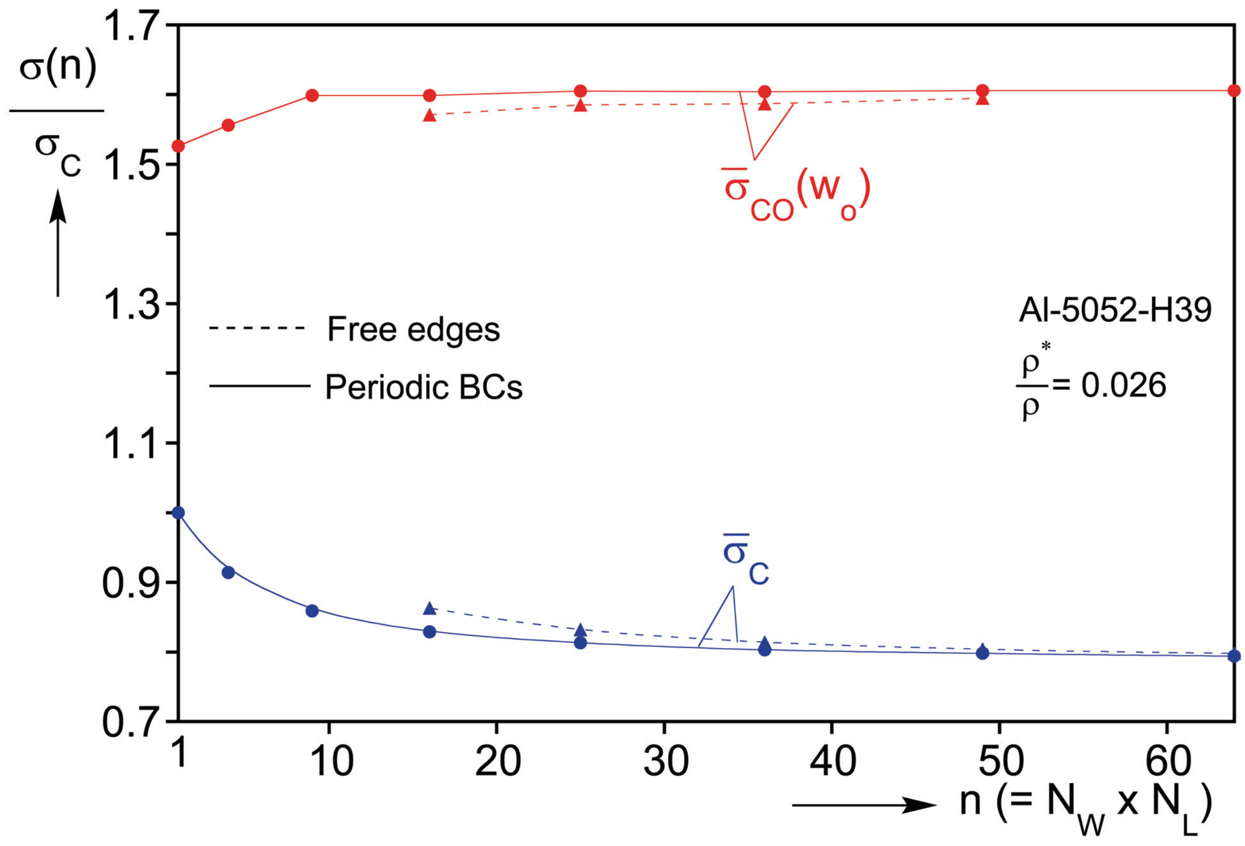

Figure 4.5: Calculated buckling and collapse stresses vs. size of square domains with and without periodicity conditions.

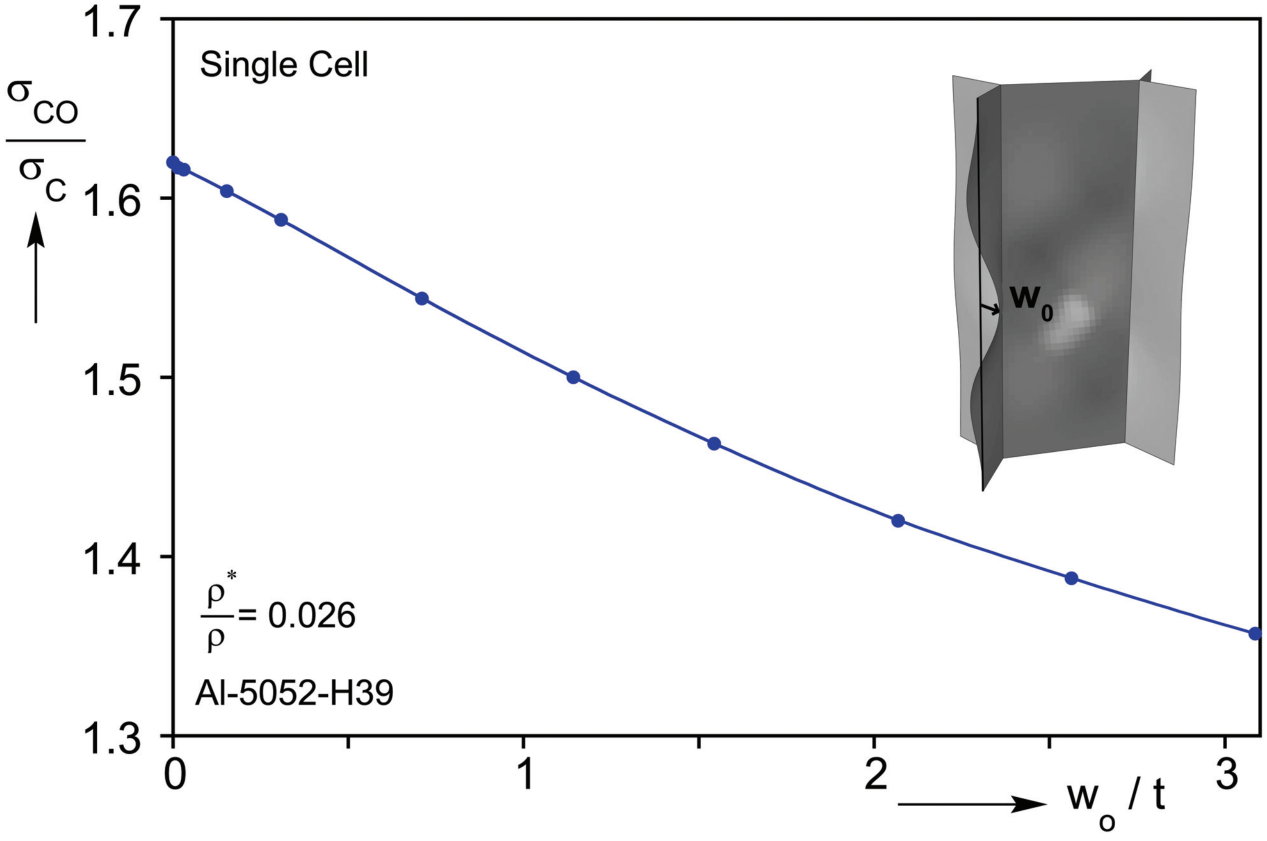

Figure 4.6: Calculated collapse stress vs. amplitude of initial imperfection corresponding to the critical buckling mode.

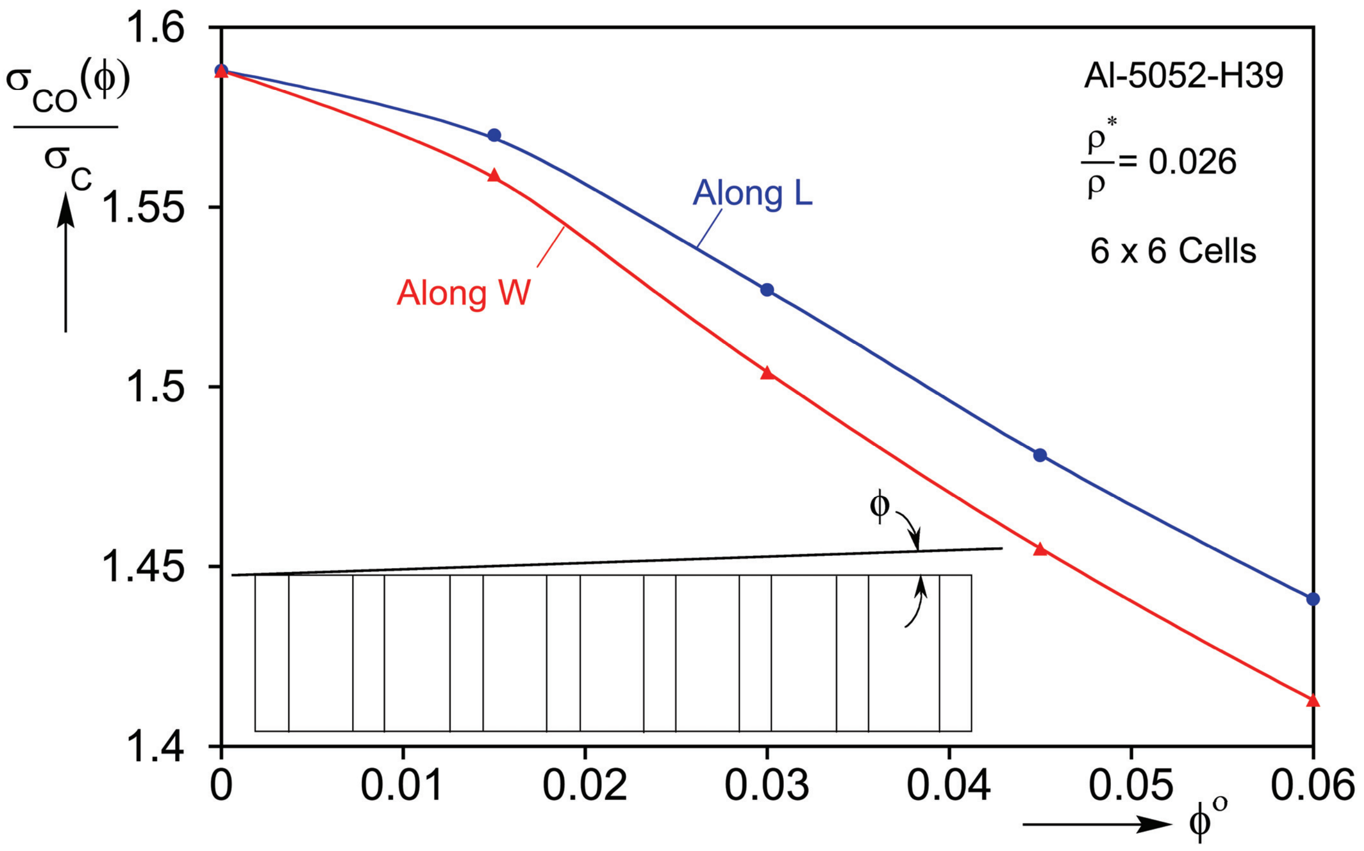

Figure 4.7: Calculated collapse stress vs. platen misalignment angle along L and W directions (6×6 cells domain).

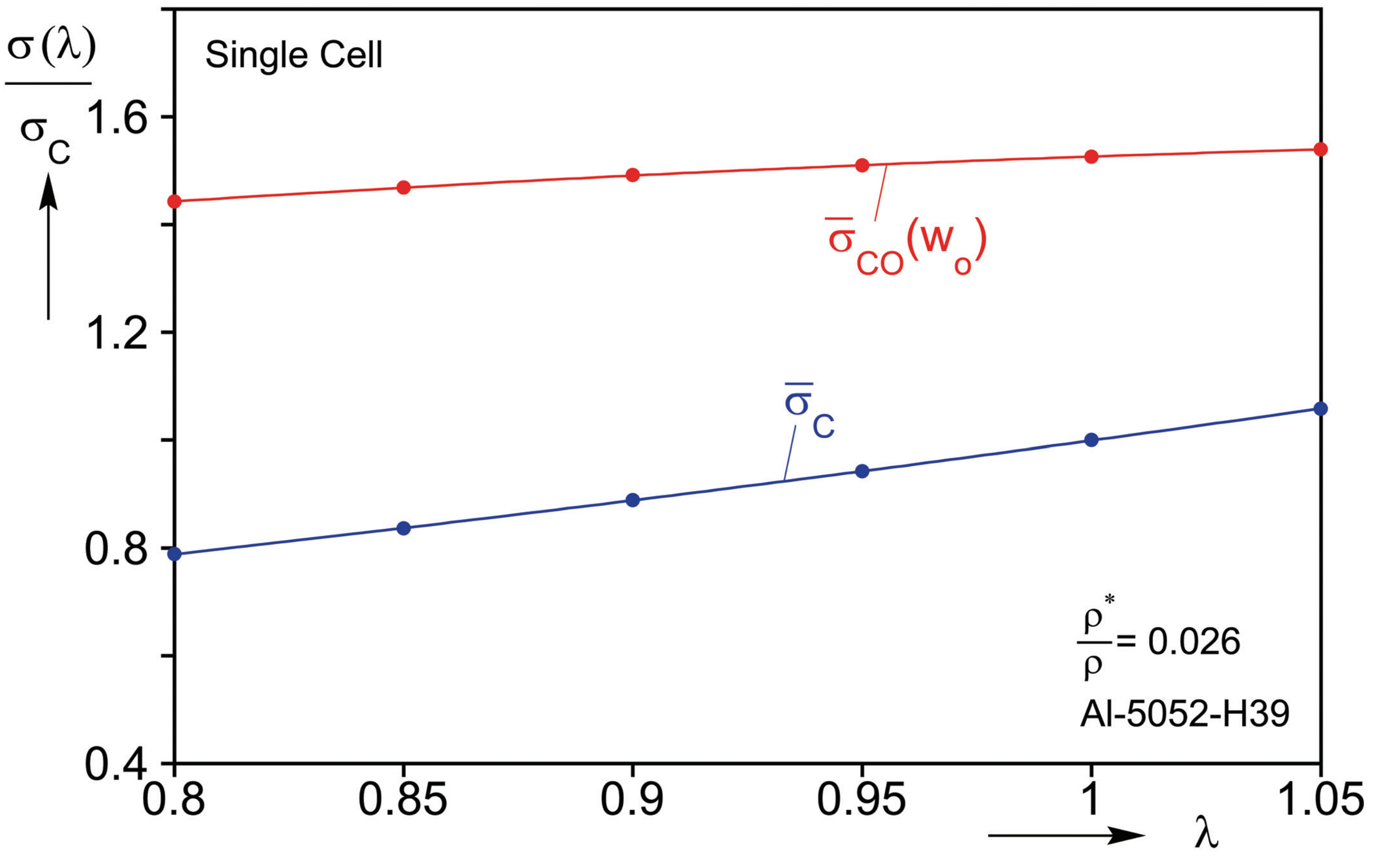

Figure 4.8: Calculated buckling and collapse stresses vs. bond length imperfection parameter λ.

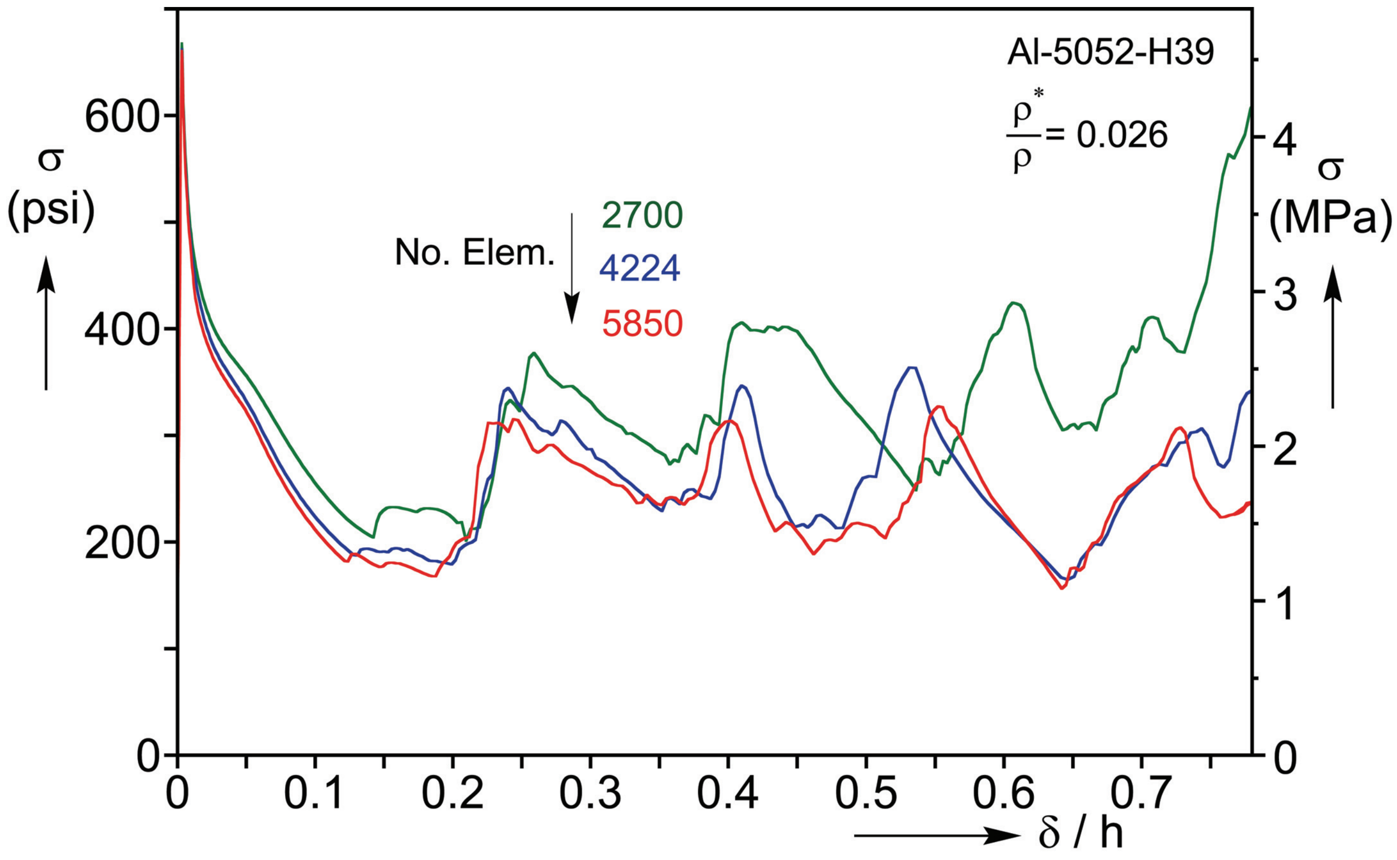

Figure 4.9: Calculated axial stress-shortening responses from unit cells with various meshes.

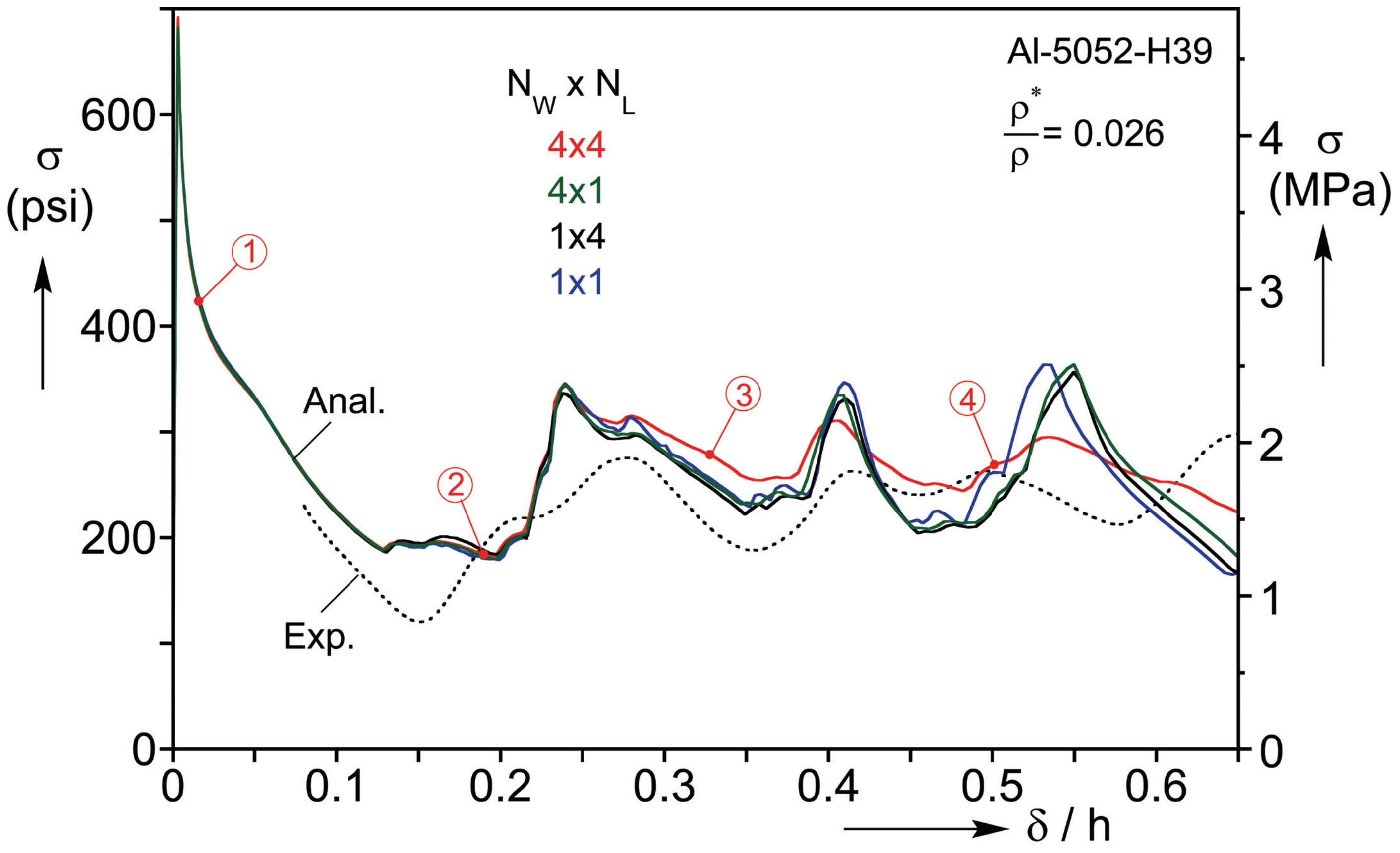

Figure 4.10: Calculated axial stress-shortening responses for various domain sizes along with an experimental one.

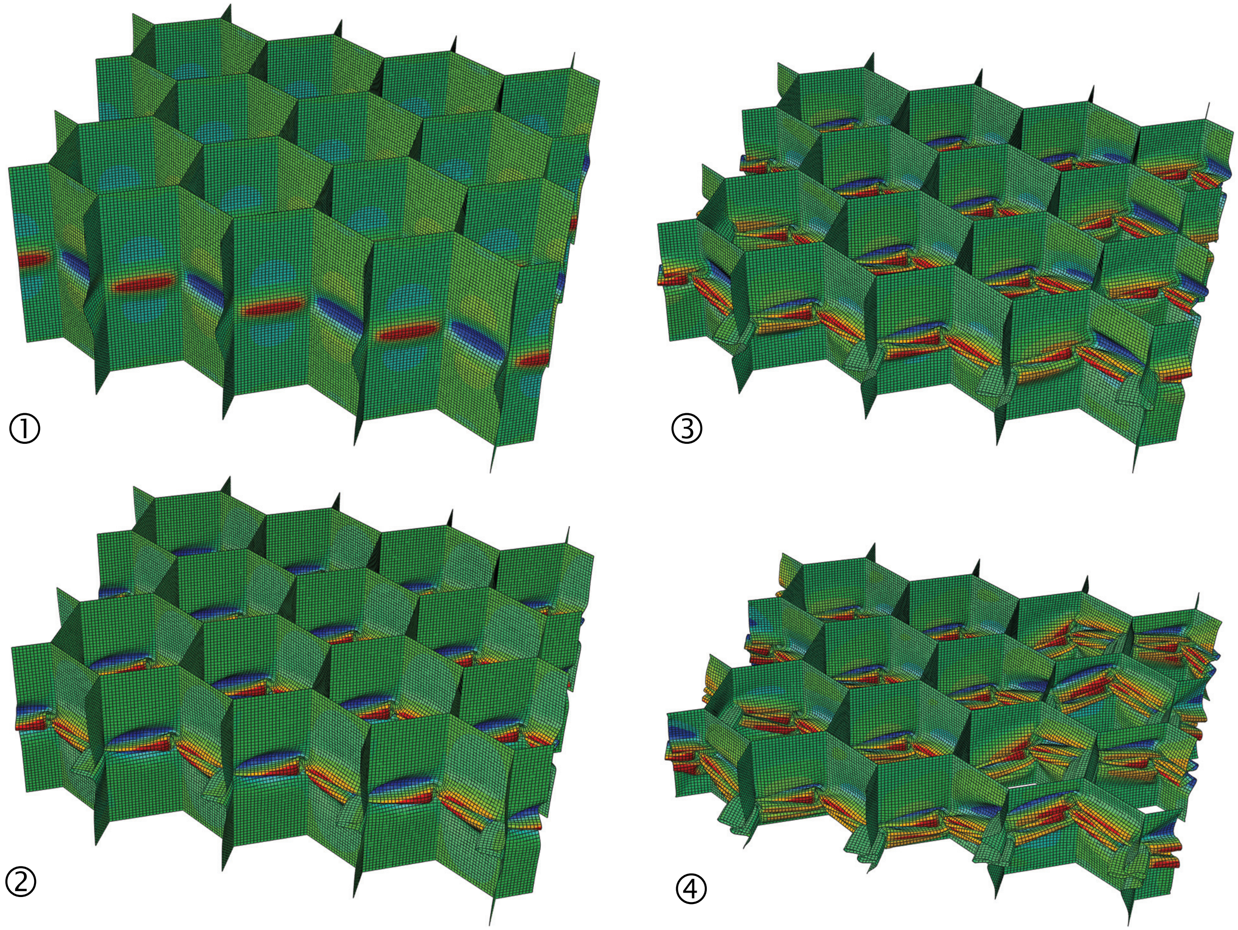

Figure 4.11: Deformed configurations corresponding to numbered bullets on the response of 4×4 cells domain in Fig. 4.10.

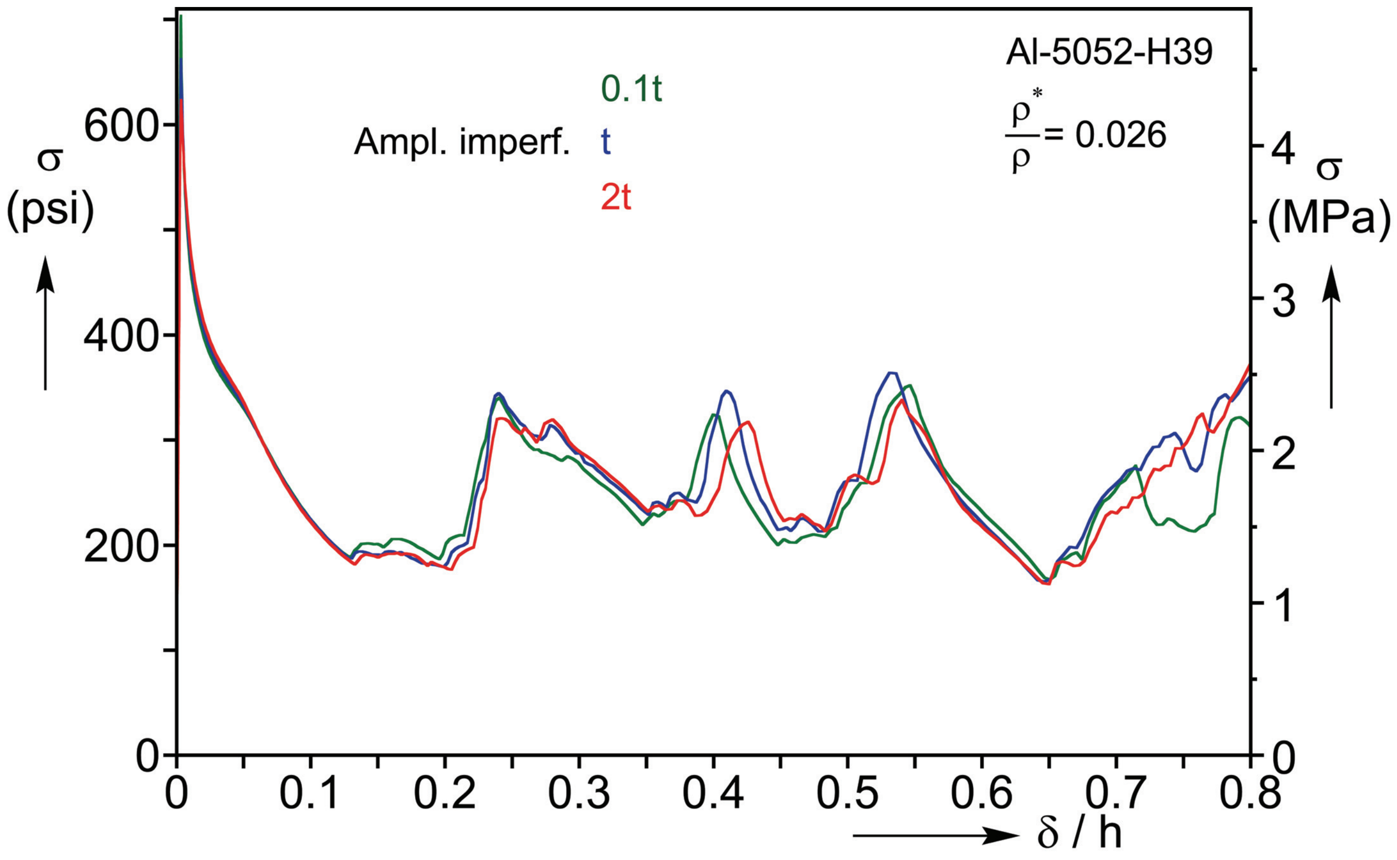

Figure 4.12: Calculated axial stress-shortening responses for various amplitudes of modal imperfection.

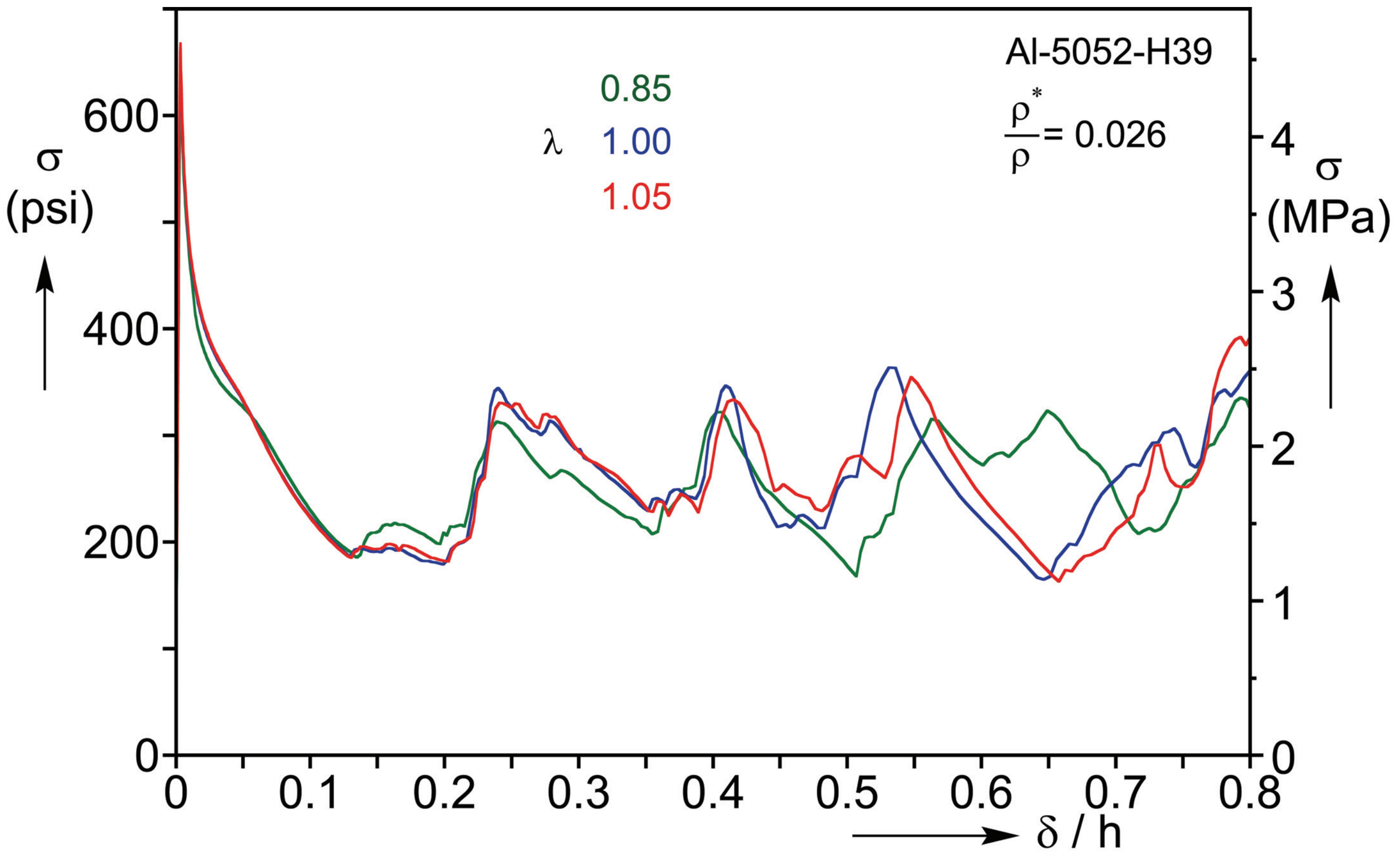

Figure 4.13: Calculated axial stress-shortening responses for various bond length imperfections.

Appendix A

Experimental Measurements of Honeycomb Material Properties

Uniaxial tension tests of both honeycomb aluminum foil and epoxy specimen were performed in order to obtain their main elastic-plastic properties.

A.1 ALUMINUM ALLOY

The aluminum samples were extracted from single thickness walls of the honeycomb used in the crushing experiments. The specimens which had a thickness $t = 0.00374$ in (95 μm) where machined to the dog-bone geometry depicted in Fig. A.1. These were tested in tension in a standard testing machine equipped with a low capacity load cell using custom grips. Figure A.2 shows the measured stress-strain response from such an experiment. Following an initial linear elastic response with modulus of elasticity $E \approx 10^4$ ksi (69 GPa), the material yielded at a level of stress of about 36 ksi (248 MPa), and the stress then slightly increased up to a strain of 5% where failure occurred. The series of tests performed by Floccari [2008] showed repeatability. Thus the measured values reported above are the ones used in the analyses reported in Chapters 3 and 4.

A.2 EPOXY RESIN

A sample of Hysol EA9696 resin was prepared by bonding together several layers of epoxy extracted from bulk 0.060 psf (0.293 kg/m^2) sheets. The layers were cured at 250°F (121°C) for 90 minutes in a Teflon mold applying small pressure. After curing and once the temperature dropped to room temperature, the specimen was removed from the mold and measured. The geometry of the specimen is reported in Fig. A.3. The sample of epoxy was tested in uniaxial tension in a screw-type testing machine. Figure A.4 shows the measured stress-strain response obtained from this specimen. The response is characterized by a modulus of elasticity $E = 211\text{ksi}$ (1.45 GPa) and a yield stress of 3.78 ksi (26.1 MPa). Failure of the specimen occurred at a strain of 7%.

Appendix B

Meshing of the Unit Cell with Matlab Code

The meshing of the geometry of the unit cell is realized by using a Matlab code. The code was developed in order to automatically generate the node positions, their numbering and the element connectivity. Different parameters can be adjusted in the code as described in Section 3.4.5.

The meshing was done by consecutively considering the five walls of the unit cell denoted by the numbered bullets in Fig. B.1. The double thickness walls (① and ②) are meshed first, while single thickness wall (③, ④ and ⑤) are meshed afterwards for the reasons described below.

B.1 NODE NUMBERING

As explained above, the numbering of the nodes is realized wall by wall in the order of the numbered bullets in Fig. B.1. The nodes are numbered first from top to bottom, and then from left to right (with respect to L-direction). Figure B.2a shows the node numbering for the first wall considered (①). Nodes of subsequent walls are numbered in a similar fashion with continuously increasing numbers.

It is important to note that the nodes lying on the edges where different walls are connected are numbered only once. As an example, the nodes marked in red color in Figs. B.1 and B.2a are numbered only when considering wall ①; the nodes marked in green in Fig. B.1 are numbered only when considering wall ②.

Below is an example of the ABAQUS data lines characterizing the three first node positions when $c = 0.375$ in, $h = 0.625$ in, and $N_h = 64$.

```
1, 0.00000, 0.28125, 0.62500
2, 0.00000, 0.28125, 0.61523
3, 0.00000, 0.28125, 0.60547
```

The first number of each line corresponds to the node reference number while the three following are the coordinates in the (x_1, x_2, x_3) coordinate system.

B.2 ELEMENT NUMBERING AND CONNECTIVITY

Similarly, the elements are numbered in the order of the walls, from top to bottom, and left to right. The element numbering of the first wall is shown in Fig. B.2b. Again, the elements numbering is continuous from the first to the last wall.

The total number of elements, *M*, of the unit cell can be calculated from the ratio c/h and the number of elements along the height N_h as follows:

$$M = 6N_h \times round(\frac{c}{h} \cdot \frac{N_h}{2\sqrt{3}}), \tag{B.1}$$

where *round* represents the nearest integer function.

The connectivity of S4 shell elements to their four attached nodes is realized by the code. The ordering of the nodes attached to each element was coded such that the element normal vectors always point in the negative W-direction (right-hand rule). Nodes lying on the edges of the cell's corners are connected to the corresponding elements of the three adjacent walls.

Below is an example of the ABAQUS data lines characterizing the three first element connectivity when $c = 0.375$ in, $h = 0.625$ in, and $N_h = 64$.

1, 1, 2, 67, 66

2, 2, 3, 68, 67

3, 3, 4, 69, 68

The first number of each line corresponds to the element reference number while the four following corresponds to the nodes attached to it.

B.3 NODE AND ELEMENT SETS

The element sets are easily created by including all the elements of walls ① and ② for the double thickness shells set and all the elements of walls ③, ④ and ⑤ for the single thickness shells set.

The nodes sets used in the boundary conditions consist of the top and bottom edges. The nodes lying on the top edges, i.e. with x_3 position of 0.625 in, are included in the top set while the one with x_3 position of 0 in are included in the bottom set.

In order to apply the periodicity conditions as explained in Section 3.4.3, the nodes of the side edges must be listed in the same order for the four different sets (corresponding to the edges denoted as A1, A2, B1 and B2 in Fig. 3.2). ABAQUS also limits nodes to be applied only one boundary or periodicity condition at a time. Therefore, these edge sets include nodes starting from the second one at the top to the second last one at the bottom.

As an example, in the case of $c = 0.375$ in, $h = 0.625$ in, and $N_h = 64$, the edge A1 include the nodes from reference number 2 up to 64.

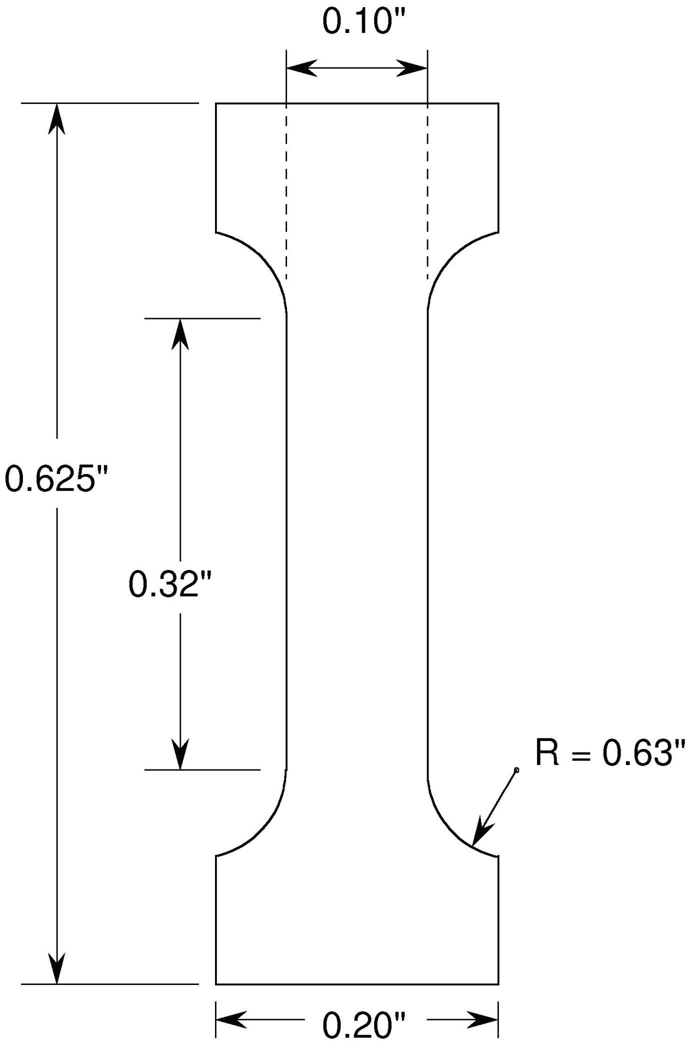

Figure A.1: Geometry of uniaxial tensile test specimens extracted from aluminum honeycomb walls.

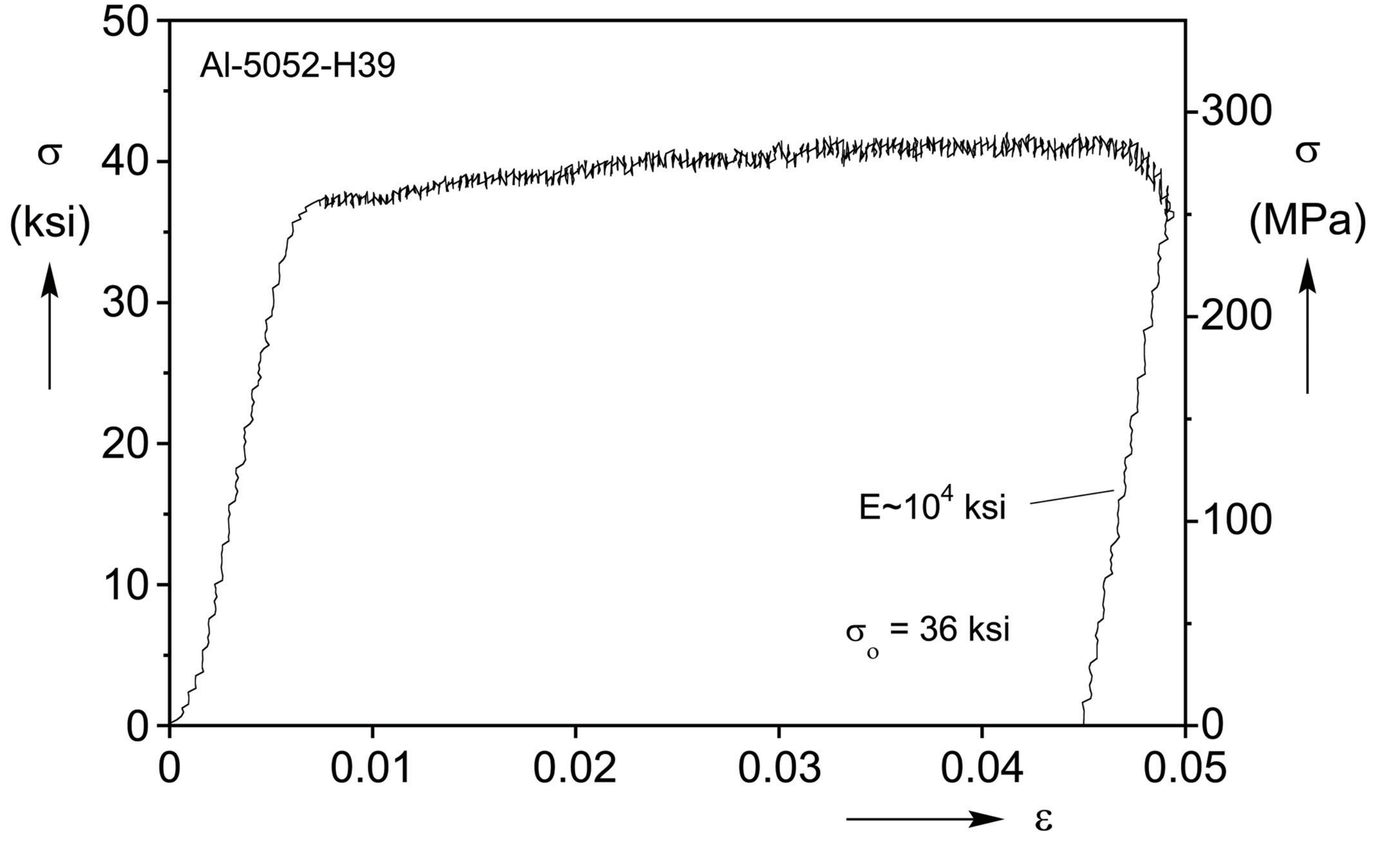

Figure A.2: Measured stress-strain response from aluminum honeycomb specimen.

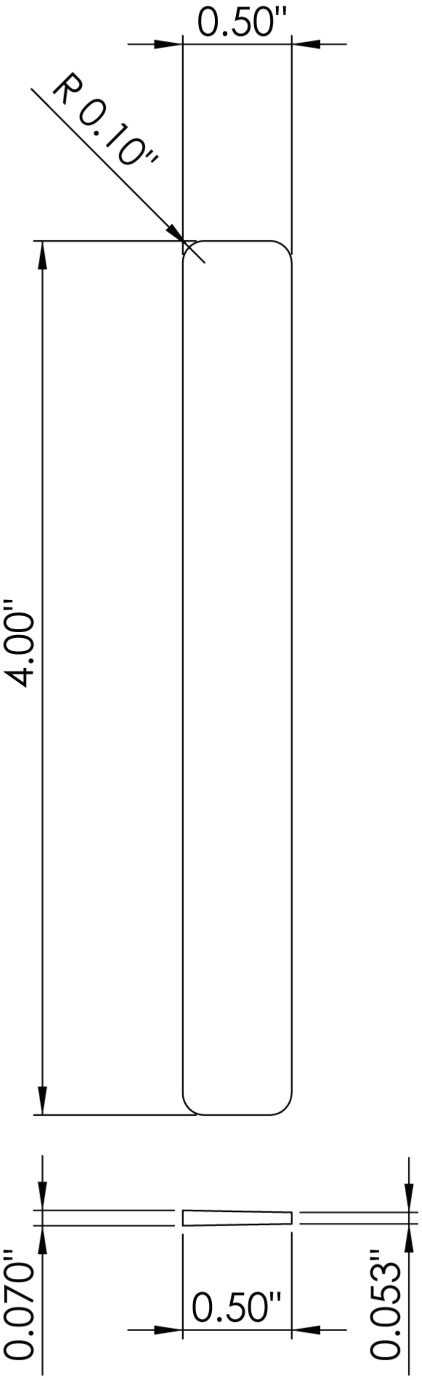

Figure A.3: Geometry of uniaxial tensile test specimen made of Hysol epoxy.

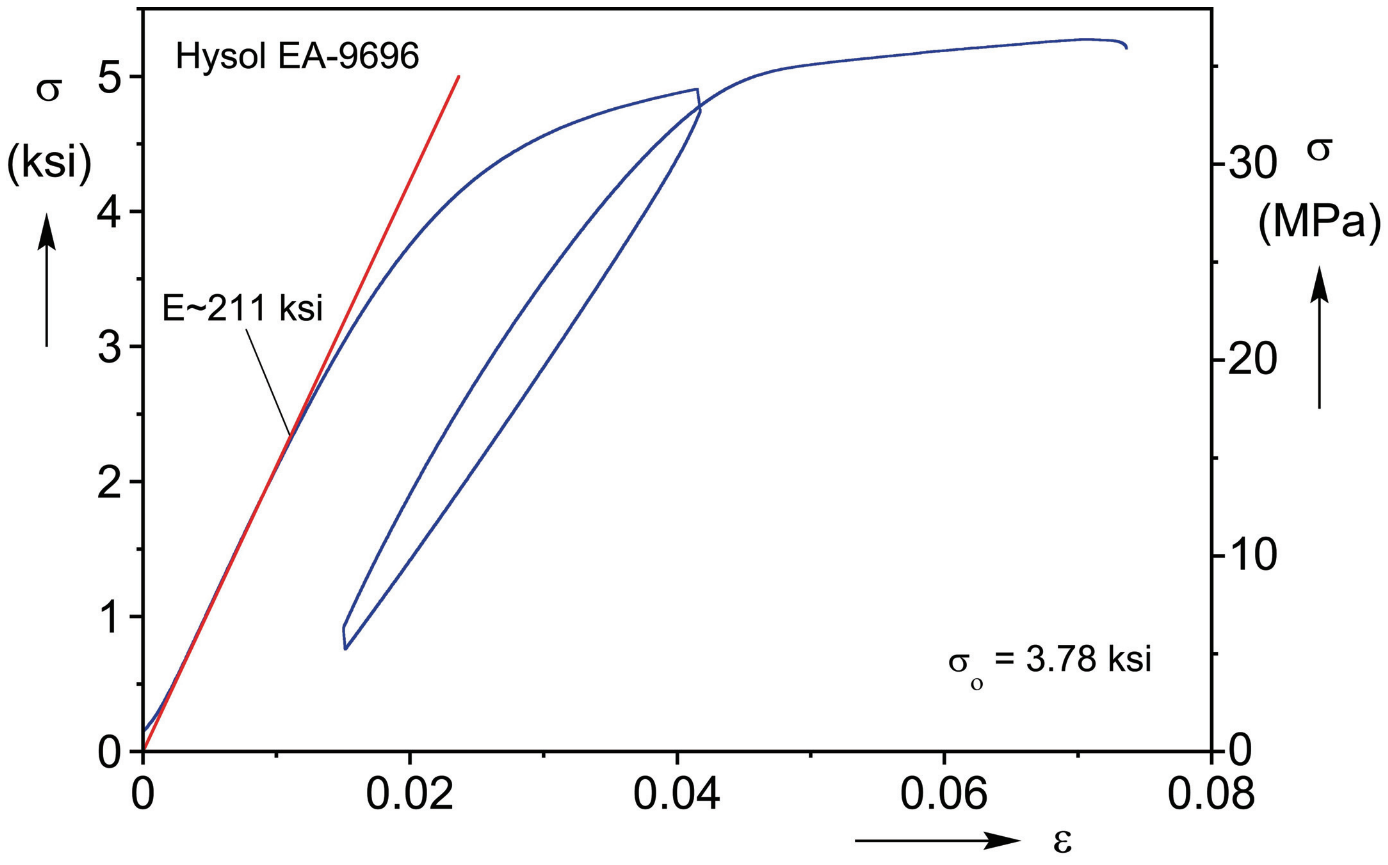

Figure A.4: Measured stress-strain response of Hysol epoxy specimen.

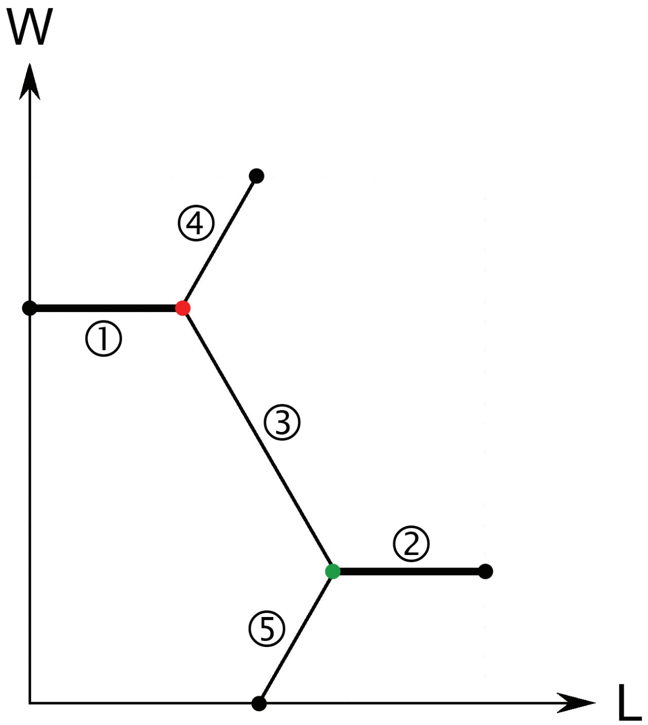

Figure B.1: Plan view of the unit cell with ordering of walls considered for the meshing.

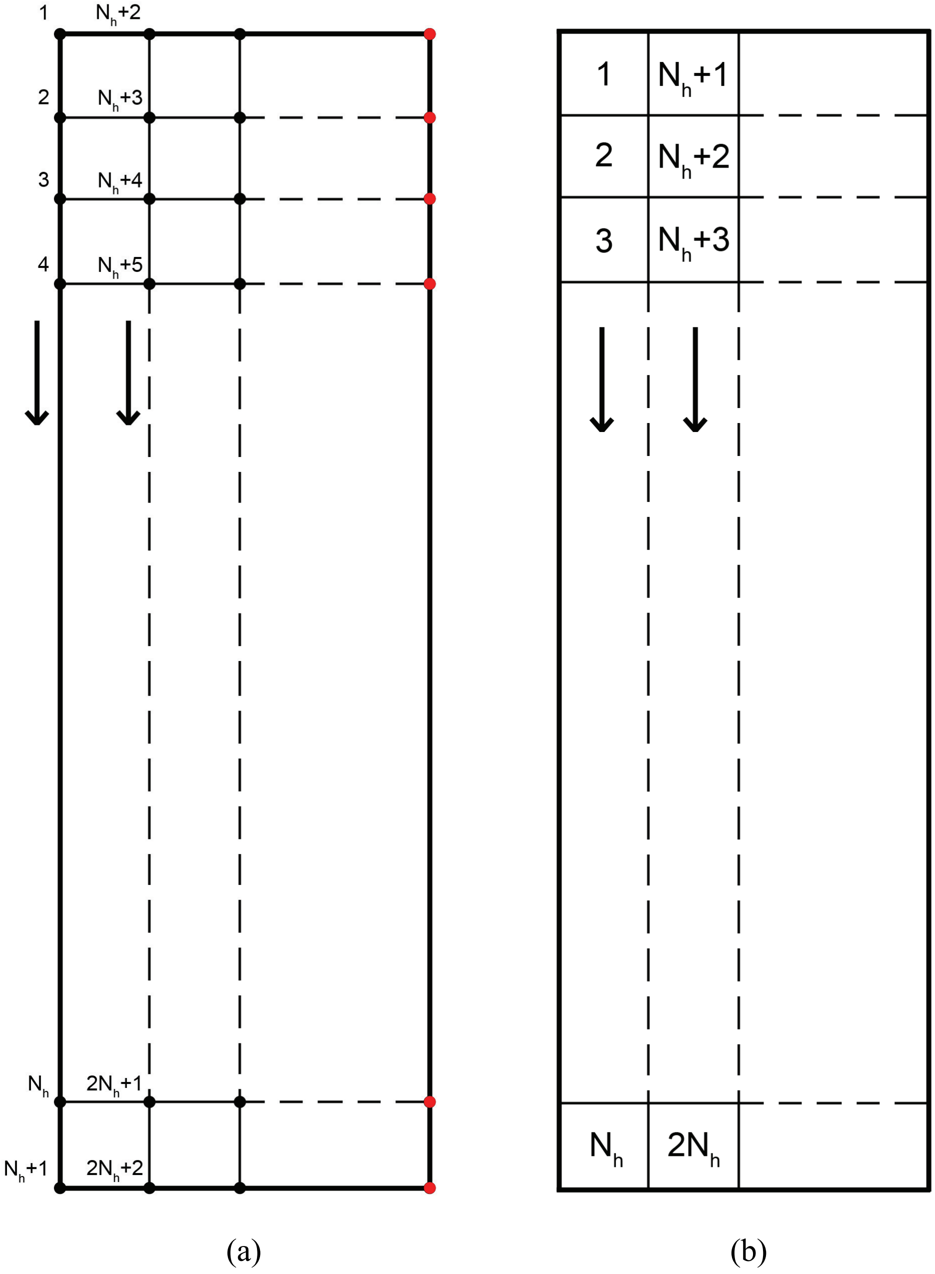

Figure B.2: Numbering of (a) nodes and (b) elements for wall denoted as ① in Fig. B.1.

References

5M (2010). http://www.5m.cz/en/sandwich-panels/

Allen, H.G. (1969). *Analysis and design of structural sandwich panels*. Pergamon Press.

Aktay, L., Johnson, A.F., Kröplin, B.-H. (2008). Numerical modeling of honeycomb core crush behavior. *Eng. Fracture Mech.* **75**, 2616-2630.

Bardi, F.C., Yun, H.D. and Kyriakides, S. (2003). On the axisymmetric progressive crushing of circular tubes under axial compression. *Int'l J. Solids & Structures* **40**, 3137-3155.

Car Body Design (2008). http://www.carbodydesign.com/archive/2008/01/30-pininfarina-nido-concept/

Chen, Y., Zhang, Z.-Y., Wang, Y., Hua H. (2009). Crush dynamics of square honeycomb thin rubber wall. *Thin-Walled Structures* **47**, 1447-1456.

Defense Industry Daily (2008). http://www.defenseindustrydaily.com/246M-to-Advance-Naval-Radar-Absorption-Materials-04923/

Flight International (2005). http://www.flightglobal.com/articles/2005/06/14/199071/creating-a-titan.html

Floccari, J.F. (2008). On the crushing of honeycomb under combined compression and shear. M.S. Thesis, Engineering Mechanics, The University of Texas at Austin.

Geymonat, G., Müller, S. and Triantafyllidis, N. (1993). Homogenization of nonlinearly elastic materials, microscopic bifurcation and macroscopic loss of rank-one convexity. *Archive Rational Mech. Analysis* **122**, 231-290.

Gibson, LJ., Ashby, M.F., Schajer, G.S., Robertson, C.I. (1982). The mechanics of two-dimensional cellular materials. *Proc. Royal Society London* **A 382**, 43-59.

Gibson, L.J. and Ashby, M.F. (1997). *Cellular Solids: Structure and Properties, 2nd Ed*. Cambridge University Press.

Gong, L., Kyriakides, S. and Triantafyllidis, N. (2005). On the stability of Kelvin cell foams under compressive loads. *J. Mechanics and Physics of Solids* **53**, 771-794.

Grediac, M. (1993). A finite element study of the transverse shear in honeycomb. *Int'l J. Solids & Structures* **30**, 1777-1788.

Goldsmith, W. and Sackman, J.L. (1992). An experimental study of energy absorption in impact of sandwich plates. *Int'l J. Impact Eng.* **12**, 241-262.

Hexcel (2010). Honeycomb attributes and properties. http://www.hexcel.com/

Jang, W.-Y. and Kyriakides, S. (2010). On the buckling and crushing of expanded honeycomb. In preparation.

Kelsey, S., Gellanty, R.A., Clark, B.W. (1958). The shear modulus of foil honeycomb core. *Aircraft Eng.* **30**, 294-302.

Klintworth, J.W. and Stronge, W.J. (1988). Elasto-plastic yield limits and deformation laws for transversely crushed honeycombs. *Int'l J. Mech. Sci.* **30**, 273-292.

Marshall, A. (1982). Sandwich Construction. In, *Handbook of Composites*, Ed. G. Lubin, Van Nostrand Reinhold Comp.

McFarland Jr., R.K. (1963). Hexagonal cell structures under post-buckling axial load. *AIAA Journal* **1**, 1380-1385.

McFarland Jr., R.K. (1964). The development of metal honeycomb energy-absorbing elements. *Technical Report No. 32-639*. Jet Propulsion Laboratory, California Institute of Technology.

Mohr, D. and Doyoyo, M. (2003). Nucleation and propagation of plastic collapse bands in aluminum honeycomb. *J. Applied Physics* **94**, 2262-2270.

Mohr, D. and Doyoyo, M. (2004a). Deformation-induced folding systems in thin-walled monolithic hexagonal metallic honeycomb. *Int'l J. Solids & Structures* **41**, 3353-3377.

Mohr, D. and Doyoyo, M. (2004b). Experimental investigation on the plasticity of hexagonal aluminum honeycomb under multiaxial loading. *J. Appl. Mech.* **71**, 375-385.

Papka, S.D. and Kyriakides, S. (1994). In-plane compressive response and crushing of honeycombs. *J. Mech. Phys. Solids* **42**, 1499-1532.

Papka, S.D. and Kyriakides, S. (1998). Experiments and full-scale numerical simulations of in-plane crushing of a honeycomb. *Acta Materialia* **46**, 2765-2776.

Penzien, J. and Didriksson, T. (1964). Effective shear modulus of honeycomb cellular structure. *AIAA Journal* **2**, 531-535.

Triantafyllidis, N. and Schraad, M. (1998). Onset of failure in aluminum honeycombs under general in-plane loading. *J. Mechanics & Physics of Solids* **46**, 1089-1124.

UK Center for Materials Education (2010). http://www.whystudymaterials.ac.uk/images/heli-fig3.jpg

Wierzbicki, T. and Abramowicz, W. (1983). On the crushing mechanics of thin-walled structures. *J. Appl. Mech.* **50**, 727-732.

Wierzbicki, T. (1983). Crushing analysis of metal honeycomb. *Int'l J. Impact Eng.* **1**, 157-174.

Wierzbicki, T., Bhat, S.U., Abramovicz, W., Brodkin, D. (1992). Alexander revisited- A two folding elements model of progressive crushing of tubes. *Int'l J. Solids & Structures* **29**, 3269-3288.

Yamashita, M., Gotoh, M. (2005). Impact behavior of honeycomb structures with various cell specifications-numerical simulation and experiment. *Int'l J. Impact Eng.* **32**, 618-630.

Zhang, J. and Ashby, M.F. (1992). The out-of-plane properties of honeycombs. *Int'l J. Mech. Sci.* **34**, 475-489.

Zhao, H and Gary, G. (1998). Crushing behaviour of aluminium honeycombs under impact loading. *Int'l J. Impact Eng.* **21**, 827-836.

Vita

Adrien Wilbert was born in Paris, France, on April 27, 1987, the son of Sylvain and Isabelle Wilbert. After graduating from Le Bon Sauveur High School in Chatou, France, he entered Lycée Pasteur scientific preparatory classes in Neuilly-sur-Seine. After passing the national entrance examination, he entered Ecole Centrale de Lille in order to obtain his Diplôme d'Ingénieur. In August 2008, he entered the University of Texas at Austin to pursue the degree of Master of Science in Engineering Mechanics as a double-degree program with Ecole Centrale de Lille.

Publications

Wilbert, A., Jang, W.-Y., Kyriakides, S., Floccari, J.F., "Buckling and Progressive Crushing of Laterally Loaded Honeycomb." *Int'l J. Solids & Structures* (submitted) 2010.

Wilbert, A., Jand, W.-Y., Kyriakides, S., "Buckling and Progressive Crushing of Laterally Loaded Honeycomb Panels." *Proceedings of the 16th US National Congress of Theoretical and Applied Mechanics* 2010. UNSCTAM2010-469.

Permanent address : 2 Avenue du Château de Bertin
78400, Chatou, France

The thesis was typed by the author.